Effects of Stress and Fluid Inclusions

on Wave Propagation in Rock

by

AMOS MICHAEL NUR

B.Sc., The Hebrew University, Jerusalem, Israel

(1962)

SUBMITTED IN PARTIAL FULFILLMENT
OF THE REQUIREMENTS FOR THE
DEGREE OF DOCTOR OF
PHILOSOPHY

at the

MASSACHUSETTS INSTITUTE OF TECHNOLOGY

June, 1969

Signature of Author ....
    Department of Earth and Planetary Sciences, June   , 1969

Certified by ....
                                     Thesis Supervisor

Accepted by ....
      Chairman, Departmental Committee on Graduate Students

Abstract

Effects of stress and fluid inclusions
on wave propagation in rock.

by

Amos Michael Nur

Submitted to the Department of Earth and Planetary Sciences
in partial fulfillment of the requirement for the
degree of Doctor of Philosophy.

Experimental results indicate that the response of
rock with fluid inclusions (air, water and glycerol at
various temperatures) to low amplitude stress waves can be
described by the bulk and shear moduli K_0 and μ_0 and
density of the solid without inclusions, the bulk modulus,
density, and viscosity of the fluid and the volume of the
inclusions, and their aspect ratios α .

The effective bulk modulus and specific attenuation in
pure dilatation are largely dependent on the bulk modulus of
the fluid inclusion and are almost independent of the fluid
viscosity.   The effective shear modulus and specific attenua-
tion in pure shear on the other hand are strongly influenced
by the viscosity of the fluid and are almost unaffected
by its compressibility. Replacement of air by water in the
microcracks of granites causes the velocity of compressional
waves, V_p, to increase by as much as 40% while the velocity
of shear waves, V_s, remains almost unchanged. An increase
of the viscosity η of the fluid phase from 10^{-1} to 10^9 poise
causes V_s to increase by 25% and V_p by only 6%. A pro-
nounced damping peak for pure shear occurs at frequency
ω_0 , when $\omega_0 \eta / \alpha \mu_0 \approx 1$.

Velocities of elastic waves and internal friction in
solid with viscous fluid inclusions are therefore frequency
dependent. Low velocity zones and strong shear anisotropy
in the earth can be explained by the presence of a viscous
fluid phase. The change of shear velocity from that of the
solid is greater than the change of V_p. The depth to the
bottom of the LVZ is frequency dependent. The viscosity of
fluid inclusions decreases with depth in the upper mantle--
10^{16} poise at 25 km, 10^{13} at 60 km and $10^7 - 10^{13}$ at 80 km.

Measurement of velocities in the laboratory on many
rocks that exhibit a large dependence of elastic wave veloci-
ties on hydrostatic pressure demonstrates that they become
elastically anisotropic under conditions of non-hydrostatic
stress. When uniaxial stress is applied the increase of

velocity is largest in the direction of the applied stress and smallest in a direction perpendicular to it. Two shear waves which are polarized in planes parallel and perpendicular to the applied stress show a velocity difference that increases with increasing stress level. The general anisotropy, of orthorhombic symmetry, is related to the influence of cracks on the effective elastic properties of rocks and can be obtained from a small number of measurable crack parameters. A theoretical study indicates that the induced velocity anisotropy can be obtained from velocity measurements under hydrostatic pressure. Cracks most likely exist in situ due to differences in the thermal expansivity and compressibility between various mineral phases. Therefore, the laboratory results can be extended to the earth and changes in the local state of stress in the earth can be determined from several repeated, precise measurements in situ of seismic travel times if sufficient information about the properties of the local rock is known. In a crustal region of increasing shear stress, as well as in the region around a fault on which sudden stress relief occurs, velocities of elastic waves increase in some directions and decrease in others. Measurement of body and interface wave velocities in existing boreholes can also be used to obtain information about stress in situ.

Thesis Supervisor: Gene Simmons
Title: Professor of Geophysics.

Acknowledgements:

I am indebted to Prof. Gene Simmons, my thesis advisor, for his counsel and assistance prior to and throughout this investigation. I would also like to extend my gratitude to Prof. W.F. Brace for extensive use of his laboratory and for his thoughtful advice; to J.B. Walsh for significant help, given always with good humor, in many theoretical aspects of this work; and to Prof. Keiiti Aki, whose encouragement and perception provided a sense of perspective. My thanks are due to D. Riach whose technical skill was invaluable, to N. Brenner who helped in some of the computational problems, to S. Solomon, W.R. Wawersik and D.H. Chung for numerous discussions and suggestions, and to Roberta Smith, Rosalyn Unger and Ann Kasameyer who patiently typed and retyped the manuscript.

The love, support and encouragement of my wife Mary enabled me to carry on during difficult periods. Her presence made graduate school tolerable.

TABLE OF CONTENTS

Chapter 7. In situ stress determinations from velocity measurements.

Appendix A: Experimental set-up for travel time measurements.

List of common symbols used throughout the manuscript:

Ap, As	Amplitudes of compressional and shear waves
a	crack width
α	crack aspect ratio; thermal expansivity
$A(\alpha)$	density distribution function of the aspect ratio α .
β	largest crack aspect ratio,
C	porosity. Concentration of inclusion in host material.
C_{ijkl}	stiffness tensor
ϵ_{ij}	strain tensor
E_{ij}, E_o, E_1, E_{11}	Young's modulus
η	viscosity
g	gravitational acceleration
i,j,k,l	indices of Cartesian coordinates
$I_{ij}, I_o, I_{(o)}$	integrals over spatial crack distribution
K, K_1	bulk modulus
l, n	direction cosines
m	a constant
$\mu_{ij}, \mu_o, \mu_{11}, \mu_\perp$	shear modulus
N_{ij}, N	distribution function of cracks with aspect ratio α .
ν_{ij}, ν_o, ν	Poisson's ratio

P — hydrostatic stress, pressure

ϕ — internal friction

$\theta, \varphi, \varphi_o$ — angular distance

Q — elastic quality factor

ρ — density

S_{ijkl} — compliance tensor

S, SH, SV — shear velocity modes

T — temperature

$\mathcal{T}$ — shear stress

σ_{ij} — stress tensor

$V_p, V_s, V_l, V_{ll}, V_{ij}, V$ — wave velocities (compressional, shear)

U_i — elastic displacement vector

ω — frequency

Z — depth

Chapter 1

Introduction

The state of stress in the earth is essentially unknown except for rough estimates of average pressure at depth and a small number of local stress values. Almost everything we do know about stresses in the earth (with the exception of direct local strain measurements in a number of mines and quarries) has been obtained from indirect measurements and theoretical models. Early estimates of pressures in the earth's interior, such as by Laplace (Bullen, 1963), were based on theoretical density distributions which agreed with the mean density and the moment of inertia of the earth. Adams and Williamson (1923a) later noticed that seismic velocities can be used to obtain radial changes in density in the earth's interior which in turn improve the estimate of the pressure. Thus, basically, the pressure distribution inside the earth is estimated from seismic wave velocities and from the mean density and moment of inertia of the earth.

But even this estimate is rather crude. The earth is believed to be in a state of hydrostatic stress--an assumption which is not critical at great depth but has great influence on the estimated near surface (crust and upper mantle) stress distribution. Birch (1964) has pointed out that shear stresses in the crust will not exceed the shear strength of crustal rock and that normal stresses will not

be tensile. Thus, shear stress can range over almost two thousand bars. Indeed the stress data available from direct measurements at or near the earth's surface indicate a rather complicated stress pattern. Hast (1958) found that horizontal stresses exceed vertical stresses in Scandinavia, Leeman (1964) reports that measured vertical stresses far exceed the horizontal ones in many mines in South Africa. However, such measurements are very sensitive to such local factors as mechanical inhomogeneities and while they are most valuable for mining and tunnelling problems, they provide little information on the regional stress field.

Indirect measurements are less localized. Here rock properties which are stress dependent are measured over a large area and the stress field or some of its elements can be evaluated. What are these rock properties? By far the most sensitive is electrical resistivity, especially at low stress levels. Brace et al. (1965) found an order of magnitude change in resistivity over a range 0-1 kb hydro-static stress which suggests that resistivity measurements can be used for stress detection. Much less sensitive to stress is the magnetic bulk susceptibility of rocks which changes by a few percent per kilobar (Kapitsa, 1955). Neither of these methods distinguish between stress and temperature effects. An increase of temperature will cause a decrease in resistivity and a decrease in apparent magnetic susceptibility similar to the effects of stress

reduction. Another important stress dependent property
are the elastic wave velocities. Predicted by Adams and
Williamson (1923b) and later verified by Zisman (1933),
elastic wave velocities in some porous rocks depend
significantly on the magnitude of the applied pressure.
The change of velocity with pressure is much smaller than
that of resistivity, but has the advantage of being associated
with waves rather than with static induced or spontaneous
fields.

.With waves we have an enormous flexibility in modes
of generation, modes of propagation, polarization and
path--each of which can be used to extract more information.
Static fields on the other hand are limited by their in-
herent non-uniqueness--additional measurements often do not
provide additional information although they may improve
estimates of measured quantities.

In this thesis we attempt to answer the following
questions: How does stress influence the various wave
velocities in rocks? What is the cause of this influence?
What else influences the velocities? How can velocities
be used to study stress in situ?

The types of rocks which we investigated were limited
because of the great variability--chemical, mineralogical,
and mechanical--of rocks in general. Soft sedimentary
rocks respond to stress in a completely different manner
from brittle rocks. Most importantly, brittle rocks are

commonly elastic and return to their initial state upon removal of stress. Their mechanical history need not be known in order to predict their response to stress. This is true for a limited range of nonhydrostatic stress. With brittle rocks, however, if the shear stress exceeds the in situ strength they break and cease to be reversible under stress. Some breaking in the form of microfracture occurs before the bulk shear strength is exceeded and thus, the range of stress over which brittle rocks are reversible is further reduced. This investigation is confined to a small number of brittle rocks, mostly granites, at low stress levels.

In chapter 2 some of the effects of fluid filled pores on seismic velocities in rocks are investigated. Commonly, compressional and shear wave velocities are significantly lower near atmospheric pressure than at pressure of a few kilobars, but when such rocks are saturated with water the compressional velocity at low pressures greatly increases. By contrast, the shear velocity is almost unaffected by the presence of fluid. A change in the degree of saturation of a porous rock produces an effect similar to that of a stress change--but only in compressional wave velocities. The various effective elastic constants which are utilized to describe the elastic response of the rock show variable degrees of dependence on saturation. The bulk modulus is most sensitive, the shear modulus least sensitive. The

applications and implications of the study of saturation go beyond the questions of rock properties at or near the earth's surface. For example, because of the law of effective stress the presence of fluid inclusions with pore pressure extends the range of application of low stress results to regions of high pressure. Some of the results obtained in chapter 2 may be applicable to the upper mantle with partial melt. Furthermore, the complexity of even a two phase system is so much greater than that of a single phase system that the concept of a geophysical equation of state in an upper mantle with melt is, perhaps, too simple.

The influence of the viscosity of a fluid phase in a solid aggregate is examined in chapter 3. Both compressional and shear wave velocities increase significantly with increasing viscosity. The internal friction in shear exhibits a peak at a particular combination of frequency, fluid viscosity and shape of the fluid inclusion. Consequently the elastic wave velocities and internal friction are also dependent on frequency. In particular, the effective shear modulus in a solid with viscous inclusions varies greatly with viscosity or frequency.

In the fourth and fifth chapters we investigated in some detail, the stress induced anisotropy in a granite. Tocher (1957) found that compressional wave velocity in the direction of an applied uniaxial stress is higher than the velocity normal to the stress. We extend his observation to determine the change of velocity with direction relative

to the direction of stress and the dependence of this change on the magnitude of the stress. We also investigate the behavior of shear waves and their dependence on stress. The velocities of both compressional and shear waves are largest in the direction of the applied stress and smallest perpendicular to it. The compressional and one shear velocity vary with direction while the other shear velocity is almost independent of direction of propagation. An analysis of the observed velocities yields the effective elastic constants of the solid which depend on stress.

The basic theory relating various stress conditions to the form of the induced elastic wave velocity anisotropy is considered in chapter 5. Although the algebra is heavy the problem is simple conceptually: cracks close at a particular magnitude of applied stress which is related to their shape and orientation. Some cracks are so oriented as to close first when uniaxial stress is being applied while others remain open. Consequently, the effective elastic properties and therefore wave propagation depend on the direction and magnitude of the applied stresses and the initial distribution of cracks in the rock.

The presence of cracks in unstressed rock samples brings us back to earth. Do these cracks exist in situ or are they introduced into the sample upon removal from the earth? In chapter 6 some relevant data is combined with a simple experiment. The changes in velocity with pressure in many igneous rocks are indicative of their

crack porosity--rocks which contain quartz show much higher porosities than rocks without quartz. A simple analysis indicates that the values of thermal expansibity and compressibility of quartz, which are much larger than the values of other common rock-forming minerals, require the presence of cracks in granites. Velocity measurements on cores, drilled from stressed samples, indicate that only a small number of cracks are introduced into the cores. Thus cracks are probably also present in situ and the theory of chapter 5 and the experimental results of chapter 4 can be applied to rocks in the real earth.

Relative and absolute stress determination can be made from velocity measurements in situ. Velocities can be measured either along profiles or in boreholes. The stress-velocity relations at a given site can be determined from samples in the Laboratory.

References:

Adams, L.H., and E.D. Williamson, Density distribution in the
        Earth, J. Wash. Acad. Sci., 13, 413, 1923.

Adams, L.H., and E.D. Williamson, The compressibility of
        minerals and rocks at high pressures, J. Franklin
        Inst., 195, 475, 1923.

Birch, F., Megageological considerations in rock mechanics
        in state of stress in the earth's crust, W.R. Judd
        ed., Elsvier Publ. Co., p. 55, 1964.

Brace, W.F., A.S. Orange, T.R. Madden, The effect of pressure
        on the electrical resistivity of water saturated
        crystalline rocks, J. Geophy. Res., 70, 5669, 1965.

Bullen, K.E., An introduction to the theory of seismology,
        Cambridge U. Press, p. 226, 1963.

Hast, Niels, The measurement of rock pressure in mines,
        Sveriges Geologiska Undersöking, Stockholm, 1958.

Kapitsa, S.P., Magnetic properties of eruptive rocks
        exposed to mechanical stresses, Akad. Nauk. U.S.S.R.,
        Ser. Geofiz. 6, 489, 1955.

Leeman, E.R., The measurement of stress in rock III,
        J. South Afr. Inst. Min. Metall., 254, 1964.

Tocher, D., Anisotropy in rocks under simple compressions,
        Trans. Am. Geophy. Union, 31(1), 89, 1957.

Zisman, W.A., Comparison of the statically and seismologically
        determined elastic constants of rocks, Proc. Nat. Acad.
        Science, 19(7), 653, 1933.

Chapter 2

The effect of Saturation on

Velocity in Low porosity rocks

1. Introduction

A very simple experiment at room pressure and temperature shows clearly the effects of moisture on the velocity of elastic waves in some rocks. In fig. 2.2 the compressional wave velocity in a sample of Chelmsford granite, initially saturated with water but allowed to dry in the atmosphere over a period of four days is plotted as a function of time. Note the rather rapid change of velocity that occurs in the first few hours even though the porosity of the sample is only about 1%. In this paper, we examine systematically the effects of saturation on the elastic properties of low porosity rocks.

The presence of a fluid phase in porous rocks is common in the earth. It constitutes one of the environmental factors that must be considered when in situ seismic velocities are to be investigated. Among these factors pressure, temperature and composition are known to influence greatly both shear and compressional wave velocities (1,2), even in rocks with such low porosity as compact granites. Because of their low porosity, generally less than 1%, the velocities in granites were not expected to be influenced by saturation with water. Simmons and Nur (3) found, however, that the velocities of compressional waves measured in place in two

three-km deep boreholes, both drilled in granites, varied
less from top to bottom than expected from laboratory measure-
ments. They suggested two possible explanations. Either
rock in situ does not contain cracks, which are responsible
for the increase in velocity in dry rock under low pressure
(4), or these cracks may have been filled with water in
situ, somehow greatly affecting the seismic velocity. Such
saturation effects have been reported by a number of investi-
gators Hughes and Jones (5), King (6), and Dortman and Magid
(7) in various rocks.

For the measurement of velocities in saturated
specimens under applied pressure it is important to consider
the effect of pore pressure. When the pore pressure equals
the external pressure, the configuration of pores and cracks
remains unchanged from the initial, unstressed configuration.
An increase of external pressure, accompanied with an equal
increase of pore pressure, affects only slightly the velocity
in the sample. Adams and Williamson (8) first noticed this
effect in their measurements of compressibility in jacketed
and unjacketed samples. If the fluid in the pores is
pressure free, cracks close under external stress and the
velocity increases with stress. Thus, in experiments in-
volving both pressure and pore fluid the pore fluid
pressure must be specified in order to obtain the effective
pressure which is merely the difference between the external
and pore pressures.

2. Experimental procedure

Both shear and compressional wave velocities were
measured on cores one inch in diameter and 2 to 3 inches
long. We used the technique described by Birch (1) with
minor, but important, variations. The flat end faces of the
samples were fine ground and parallel to within .001 inch.
The transducer assembly was attached at each end of the
sample and held in place by a rubber jacket enclosing sample
and transducers. The transducer was assembled, as shown in
fig. 2.1, inside a cylindrical brass holder with a .010
inch copper foil closing the end. A ceramic transducer
(PZT) was cemented to the foil. A small brass plug attached
to the upper surface of the transducer served as an electrode.
The copper foil served both as the second electrode and
as an impermeable barrier between the water which saturated
the sample and the pressure medium (petroleum ether). This
fluid was free to penetrate the assembly in order to avoid
non-hydrostatic stresses in the assembly. Travel times
were measured with a variable mercury delay line.*

In order to completely saturate the specimens, we
used a combination of vacuum to remove air and pressure to
force water into the pores. Brace et al. (9) described
the technique.

---

* For detail see Appendix A.

The sample is suspended over a container of water inside a vacuum chamber. After the pressure in the chamber is sufficiently low for the water to boil, the sample is then dropped into the water. The sample remains in the water container which is then placed in a gas pressure vessel and held overnight at 10 bars.

All measurements on water saturated samples were made at zero pore pressure. In order to keep the pore pressure at zero, while the confining pressure was increased, a piano wire was wrapped around the specimen before the rubber jacket was slipped over it. The configuration is shown in figure 2.1. The fluid expelled from the pores as they close is allowed to flow into the free volume between the coils of the piano wire spring and the specimen. The confining pressure was raised in small steps with long pauses between increments to allow for the reduction of transient pore pressures by the flow of water out of the specimens. The steel spring causes local stress concentrations in the sample. We used a wire with diameter about 1/10 of the diameter of the sample so that the region of stress concentration was small, confined to the outer 10% of the sample. Because a wire of sufficient diameter must be used to provide enough space for the expelled water, this method may not be suitable for use with high porosity rocks. The "dry" samples were held in a vacuum of 25 inches Hg and temperature of 50°C for 24 hours; they were then quickly

enclosed with the transducers in a rubber jacket to avoid absorption of water from the air.

Total and crack porosities (Table 2.1) as well as densities were determined by Brace (10).

3. Samples

A suite of six samples was selected for a set of measurements designed to examine the effects of saturation and external hydrostatic pressure on both shear and compressional wave velocities of low porosity rocks. The samples, with the exception of Troy granite, were the same ones used by Brace (9). Some of their physical properties are reproduced in Table 2.1. The properties of the Troy granite sample were determined with the method described by Brace (10).

4. Data

New data on the velocity of elastic waves in dry and completely saturated rocks are given in Tables 2.2 to 2.3. The compressional and shear wave velocities in dry and saturated conditions, shown in fig. 2.3, depend very differently on the degree of saturation of samples, at various pressures. The effect of hydrostatic pressure and that of fluid saturation on compressional wave velocity are similar. High velocity can be obtained either by the application of high confining pressure or by completely saturating the rock. The effect of pore pressure of V_p,

however, is small. Once the sample is completely saturated,
the effective pressure has a relatively small influence on
compressional velocity because V_p at zero effective pressure
is almost as high as the velocity of the sample would be
without any cracks. The influence of pore pressure on
shear velocity though is very significant. If pore pressure,
for example, equals the external pressure the observed
shear velocity will be approximately the same as the velocity
in the unstressed sample which is also equal to the velocity
in the dry sample. The strong dependence of velocity on
pressure and saturation is confined to low effective pressures.
At pressures above 1 or 2 kb and without pore pressure all
velocities show only a small increase with increasing stress.

The velocities of the saturated Casco granite sample
were measured also as a function of pressure without the
steel spring arrangement, thus forcing the water in the
cracks to remain there. The fluid in the pores was there-
fore confined, subject to a pressure nearly equal to the
external pressure. The velocities change but little with
external pressure (fig. 2.3a) and the constant value dv/dp
is the same as for the (1) saturated, and unconfined
specimen and (2) dry rocks at high pressure. Although V_p
of the confined sample is lower by 10%, and V_s by 35%,
from the corresponding unconfined velocities, the slopes
dv/dp are practically the same.

From the measured velocities we can obtain values of

the effective elastic constants of the dry as well as the
saturated samples. We assume that the effective elastic
constants are related to the velocities in the same way
that these quantities are related in a linear elastic
material. Thus the effective dynamic bulk modulus K is

$$K = \rho \left[V_P^2 - \frac{4}{3} V_S^2 \right]$$

and the effective shear modulus

$$M = \rho V_S^2$$

where ρ is the density of the sample. We also obtained
effective Young's modulus E and Poisson's ratio ν, for
both dry and saturated cases. The resulting values (Table 2.3,
fig. 2.4) emphasize the observation that fluid saturation
greatly influences the effective bulk modulus of a rock while
the shear modulus is almost independent of fluid inclusions.
The Poisson's ratios obtained at various pressures are of
some interest. Dry rocks exhibit very small, even negative
Poisson's ratio values while saturated rocks exhibit
abnormally high values. From the expression for Poisson's
ratio

$$\nu = \left(3K - 2M \right) \Big/ \left(6K + 2M \right)$$

it is apparent that a negative Poisson value indicates
that $K < \frac{2}{3} \mu$. Such low Poisson values in dry rocks are
observed at very low pressures only. The effective value

at higher pressures is near the intrinsic value. The effective Young's modulus is not as strongly dependent on saturation as the bulk modulus, shown clearly in fig. 2.4.

Interesting results were obtained from the first pressure run of the Bedford limestone sample, as shown in fig. 2.5. Like all other samples the compressional velocity in the dry sample increased greatly with pressure at low pressure, then became more constant. At a pressure of about 2 kilobars, however, the velocity increased again with pressure. Upon reduction of pressure the velocity remained significantly higher than in the initial part of the cycle, except at low stress when the decrease of V_p with decreasing pressure became so large that the final velocity was well below the initial velocity. Similar behavior under pressure was observed by Brace (11), also at about 2 kilobars for electrical resistivity. Since the strength of the Bedford limestone is rather low and initial pore porosity high, it is likely that pores begin to collapse at an external hydrostatic stress of 2 kilobars or more. A collapsed pore may in later cycles behave like a crack, which in turn will increase the dependence of velocity on stress at low stress levels.

5. Discussion of results

The simplest theory of wave velocities in two-phase systems is the so-called "Time average" (12, 13) which is summarized by the relation

$$\frac{1}{\overline{V}} = \frac{a}{V_1} + \frac{1-a}{V_2}$$

where $\overline{V}$, V_1, and V_2 are wave velocities of the composite and
of the phases 1 and 2, respectively, and a is the concentra-
tion of phase 1, and (1-a) is that of phase 2. Equation (1)
can be interpreted physically as expressing the velocity
of waves which are short compared to the size of the in-
homogeneity, assumed here as layered, in the composite. It
is clear, however, that the wave lengths, even in the mega-
cycle range, are not generally smaller than the size of the
inhomogeneity in the sample. Furthermore, the time average
method fails when one of the phases is air in the case of
compressional and shear waves or a liquid in the case of
shear waves.

A more fundamental approach is based on the concept of
effective elastic constants which can be used to yield the
various wave velocities. The first attempts to obtain
effective elastic constants from the properties of the com-
ponents required only the specification of the relative
concentrations. The Voigt-Reuss estimates provide lower
and upper bounds for the effective elasticity of a composite,
but these bounds are too far apart for a composite with
holes, or liquid inclusions for shear modulus. Hashin and
Shtrikman (14) using a variational energy method derived
narrower bounds and proved that they are indeed the narrowest
ones for a composite with specified concentration alone.

Even their bounds are widely separated for a medium with holes. Mackenzie (15) derived expressions for both bulk and shear moduli assuming that all porosity is in the form of round pores. Satô (16, 17) extended those results to spherical holes with liquid and solid inclusions and computed the velocities of seismic waves. When the pores contain water Satô's results indicate that both compressional and shear velocities should differ by less than 1% from the intrinsic velocities if the porosity is 1%. Compressibility measurements of sintered porous silicates by Walsh et al. (18) indicate that Mackenzie's and Satô's expressions are quite satisfactory if the porosity is in the form of round holes.

Our results, however, are at variance with the pore model. Saturating the granite samples, which have porosities less than .01, caused V_p to increase by as much as 40%. It is necessary then to take into account the fact that porosity C is not in the form of round holes. Wu (19) derived expressions for effective elastic constants for two phase composites with ellipsoidal inclusions. Walsh (20) generalized Wu's expressions for two phase systems, in which the inclusion is empty or contains a fluid. The shape of the inclusion or crack, assumed to be penny-like, is specified through a single parameter--the aspect ratio $\alpha = a/d$ where a is the width and d is the diameter of the crack.

Walsh's expressions for bulk and shear moduli when the inclusion fluid is air, (whose viscosity is vanishingly

small and compressibility almost infinite) are:

$$\frac{1}{\bar{K}_{air}} = \frac{1}{K_o}\left[1 + m \cdot \frac{c}{\alpha}\right]$$

$$\frac{1}{\bar{\mu}_{air}} = \frac{1}{\mu_o}\left[1 + n \cdot \frac{c}{\alpha}\right]$$

where

$$m = K_o(3K_o + 4\mu_o)\Big/\pi\mu_o(3K_o + \mu_o)$$

$$n = \frac{1}{15\pi}\left[\frac{8(3K_o + 4\mu_o)}{(3K_o + 2\mu_o)} + \frac{4(3K_o + 4\mu_o)}{(3K_o + \mu_o)}\right]$$

The corresponding expressions for the same material
saturated with water (viscosity low but compressibility
finite) are:

$$\frac{1}{\bar{K}_{water}} \approx \frac{1}{K_o}\left[1 + c\left(\frac{K_o}{K_{H_2O}} - 1\right)\right]$$

and

$$\frac{1}{\bar{\mu}_{water}} \approx \frac{1}{\mu_o}\left[1 + n \cdot \frac{c}{\alpha}\right]$$

for signal frequencies around 5 MH. Unlike the bulk
modulus, the shear modulus is unaffected by saturation.
The effective bulk modulus of saturated rock $\bar{K}_{water}$,
is almost independent of α despite the importance of α
in the dry case.

For rocks, K_o/K_{H_2O} and C = .005 which yields
$\bar{K}_{water} \approx .96 K_o$. The difference between the bulk modulus of the
saturated composite and the intrinsic modulus of the solid
is only a few percent. If the composite contains air this

difference will depend on the aspect ratios α. The range
of these α values can be estimated from the change, with
pressure, of the elastic properties of a composite. Walsh
(21) showed that the pressure P, required to close a crack
is related to its shape by $P \approx E_0 \alpha$ where E_0 is Young's
modulus of the solid. Because elastic properties become
almost completely independent of pressure at 1 kb we find,
for $E = 10^6$ that $\alpha \le 10^{-3}$.

The crack model leads to the prediction that the
difference between the "dry" and "saturated" bulk modulus
or compressional wave velocities should increase with
increasing crack porosity. Such an increase is clearly shown
in fig. 2.6, while no correlation with volume porosity is
noticeable (Table 2.1). From Walsh's expressions we notice
also that for composites with high porosity the effect of
volume porosity on the elastic properties can be quite
significant. However, the effect of pressure on these
same properties is largely due to cracks and cannot be
attributed to porosity of round holes.

The change of volume of holes with external pressure
is rather small. The displacement of the cavity's wall
U under pressure P is

$$U \approx \frac{a \cdot P}{E_0}$$

where a is the radius of the cavity and E_0 is Young's
modulus of the solid. To close the cavity the displacement

must be of the order of radius a or $P \approx E$. For most rocks such pressure is far beyond their shear strength. Cavities will, therefore, collapse before they close elastically.

Our results are consistent with a model of rock with small penny shaped micro cracks. Their closure is very sensitive to pressure, unlike round pores, and when filled with water they greatly influence the effective compressibility of the rock.

6. Some applications to the earth

The available field data on velocities in the shallow crust is not complete because of the difficulty in measuring shear wave velocities. Nevertheless, we can test our laboratory results against a number of field observations. Dobrin et al. (22) found that V_p increased greatly when measured below the water table while V_s remained essentially unaffected.

The observation by Simmons and Nur (3) of high, almost constant, velocity from top to bottom in two boreholes 3 km deep in granites can now be explained by the presence of water in the cracks. An interesting test of the saturation mechanism in granites in situ would be the determination of shear wave velocity as a function of depth. Unlike the compressional waves, shear wave velocity is almost unchanged when the air in cracks is replaced by water. On the other hand, closure of crack by pressure does influence the shear

velocity and we would, therefore, expect a noticeable change from top to bottom.

Birch (4) and others reported a large range of initial V_p values for samples of the same rocks. These variations were attributed to inhomogeneity or anisotropy of the samples. It is quite possible, however, that much of the scatter is simply due to various degrees of saturations, depending perhaps on the humidity and temperature in the laboratory.

A discrepancy between dynamic and static elastic moduli of rocks was noticed first by Zisman (23). Commonly the static moduli at low pressures are lower (24) than the dynamic moduli. Our results combined with Walsh's theory can explain in part such a discrepancy in rocks which contain fluids like water. At short periods of loading, such as in seismic waves, the fluid has no time to flow out of the crack which increases the crack's resistance to closure and increases the effective bulk modulus of the rock. If, however, the loading period is sufficiently long to allow flow to occur (and space is available for the fluid) cracks will behave as dry, air filled cracks. The relations between period and effective elasticity must involve many other physical parameters such as permeability of the fluid in the rock, which depends on pressure and crack shape and viscosity of the fluid which depends significantly on temperature.

Our results could shed some light on the question of partial melt that possibly exists in the upper mantle. Shimozuru (25) suggested that a small amount of melt in the form of flat pockets could greatly influence the effective shear modulus of mantle material. Aki (26) showed that the presence of small melt pockets under Japan could explain the observed phase velocities of Love and Rayleigh waves. These pockets need also have a preferred orientation to cause an apparent velocity anisotropy for long waves.

The bulk modulus of a solid with fluid pockets will be almost identical with that of the solid without pockets, while the shear moduli will differ greatly. This difference will depend, most importantly, on the shape of the pockets, their orientation and the viscosity of the fluid. In Chapter 3, the effects of viscosity on shear modulus are investigated and we defer extensive discussion of the application of our laboratory results to an interpretation of the low velocity zone. Brace et al. (27) performed a series of experiments on the melting of granites. They found that melting starts at grain boundaries and that at least initially the melt is in the form of a thin film, which could perhaps be described by a small α value. Composites with small α values, such as Casco granites, need but a very small volume of melt to greatly reduce their effective shear modulus.

7. Conclusions

The inclusion of fluid in micro cracks greatly in-
creases the compressional wave velocity while shear velocity
remains unchanged. Therefore, the effective bulk modulus
of a rock is very sensitive to the degree of saturation.
Other effective elastic constants show various degrees of
dependence on saturation. The dynamic Poisson's ratio of
saturated rock with cracks is abnormally high while the
values in dry rock are very low, even negative.

The shear modulus of a rock with cracks is a better
stress indicator because it is insensitive to saturation.

References:

(1) Birch, F., The velocity of compressional waves in rocks
     to 10 kb, part 1, J. Geophy. Res., 65, 1083, 1960.

(2) Simmons, Gene, Velocity of shear waves in rocks to
     10 kb, 1. J. Geophy. Res., 69(6), 1123, 1964.

(3) Simmons, Gene and Amos Nur, Granites: relation of
     properties in situ to laboratory measurements, Science,
     162, 789, 1968.

(4) Birch, F., The velocity of compressional waves in rocks
     to 10 kb, part 2, J. Geophy. Res., 66, 2199, 1961.

(5) Hughes, D.S. and H.J. Jones, Variations of elastic
     moduli of igneous rocks with pressure and temperature,
     Bull. G.S.A., 61, 843, 1950.

(6) King, M.S., Wave velocities in rocks as a function
     of changes in overburden pressure and pore fluid
     saturants, Geophysics, 31(1), 50, 1966.

(7) Dortman, N.B., and M.Sh.Magid, Velocity of elastic
     waves in crystalline rocks and its dependence on
     moisture content, Doklad Acad. Scien. USSR, Earth
     Sci. Section, 179(1), 1, 1968.

(8) Adams, L.H., and E.D. Williamson, The compressibility
     of minerals and rocks at high pressures, J. Franklin
     Inst., 195, 475, 1923.

(9) Brace, W.F., A.S. Orange and T.R. Madden, The effect
     of pressure on the electrical resistivity of water
     saturated crystalline rocks, J. Geophy. Res., 70,
     5669, 1965.

(10) Brace, W.F., Linear compressibility of rocks, J.
     Geophy. Res., 70(2), 391, 1965.

(11) Brace, W.F., and A.S. Orange, Further studies of the
     effects of pressure on electrical resistivity of rocks,
     J. Geophy. Res., 73(16), 5407, 1968.

(12) Wyllie, M.R.J., A.R. Gregory, and L.W. Gardner, Elastic
     wave velocities in heterogeneous and porous media,
     Geophysics, 21, 41, 1956.

(13) Wyllie, M.R.J., A.R. Gregory, and G.H.F. Gardner, An
     experimental investigation of factors affecting elastic
     wave velocities in porous media, Geophysics, 23, 459,
     1958.

(14) Hashin, Z., and S. Shtrikman, A variational approach to the theory of elastic behavior of multiphase materials, J. Mech. Phy. Solids, 11, 127, 1963.

(15) Mackenzie, J.K., The elastic constants of a solid containing spherical holes, Proc. Phys. Soc., London, B63, 2, 1950.

(16) Satô, Y., Velocity of elastic waves propagated in media with small holes, Bull. Earthqu. Res. Inst., 30(3), 179, 1952.

(17) Satô, Y., Velocity of elastic waves propagated in media with small obstacles, 31(1), 1, 1953.

(18) Walsh, J.B., W.F. Brace, and A.W. England, Effect of porosity on compressibility of glass, J. Am. Ceramic Soc., 48(12), 605, 1965.

(19) Wu, T.T., The effect of inclusion shape on the elastic moduli of a two phase material, Int. J. Solids Structures, 2, 1, 1966.

(20) Walsh, J.B., A new analysis of attenuation in partially melted rocks, J. Geophy. Res., in press, 1969.

(21) Walsh, J.B., The effect of cracks on the compressibility of rocks, J. Geophy. Res., 70(2), 381, 1965.

(22) Dobrin, M.B., R.F. Simon, and P.L. Lawrence, Rayleigh waves from small explosions, Am. Geophy. Un. Trans., 32, 822, 1951.

(23) Zisman, W.A., Comparison of the statically and seismologically determined elastic constants of rocks, Proc. Nat. Acad. Sci., 19(7), 653, 1933.

(24) Simmons, Gene, and W.F. Brace, Comparison of static and dynamic measurements of compressibility of rocks, J. Geophy. Res., 70(22), , 1965.

(25) Shimozuru, D., Geophysical evidence for suggesting the existence of molten pockets in the earth's upper mantle, Bull. Volcanologique, 26, 181, 1963.

(26) Aki, Keiiti, Seismological evidence for the existence of soft thin layers in the upper mantle under Japan, J. Geophy. Res., 73(2), 585, 1968.

(27) Brace, W.F., W.C. Luth and J. Unger, Melting of granite under an effective confining pressure, abstract, presented at Annual Meeting of G.S.A., N.Y., 1966.

Table 2.1

Physical properties of rock samples.
These samples were used to determine the effects of
pressure and saturation on elastic wave velocities.

	Vp(KM/SEC)			Vs(KM/SEC)		Porosity[1]			Density[1]	Average[1] grain size
	at 1 bar		at 2Kb	at 1 bar	2Kb	crack	pore	total	gr/cm³	(mm)
	dry	sat								
Casco granite	3.22	5.50	6.54	2.40	3.73	.0045	.002	.007	2.626	5.0
Troy granite	4.50	5.90	6.60	3.10	3.65	.001	.001	.002	2.67	4.0
Westerly granite	3.80	5.48	6.10	2.90	3.46	.002	.007	.009	2.646	.75
Bedford limestone	2.70	4.60	4.90	1.55	2.64	.002	.121	.123	2.620	1.0
Solenhofen limestone	5.67	5.64	5.78			0	.047	.047	2.663	.01
Webatuck dolomite	4.96	6.43	7.03	3.480	4.20	.0022	.005	.007	2.867	.45

(1)- measured by Brace, 1965 and later. Troy granite was measured by Brace and Nur.

Table 2.2a

Elastic Wave Velocities in Casco Granite

P(BAR)	VP(DRY)	VP(SAT)	VS(DRY)	VS(SAT)
20.	3.400	5.510	2.400	2.500
25.	3.590	5.600	2.440	2.590
40.	4.100	5.780	2.530	2.640
75.	4.630	5.990	2.660	2.940
100.	5.050	6.020	2.790	3.000
150.	5.420	6.040	2.990	3.100
200.	5.630	6.140	3.120	3.160
250.	5.800	6.180	3.240	3.200
300.	5,900	6.220	3.320	3.220
350.	6.020	6.250	3.390	3.290
430.	6.110	6.280	3.460	3.340
550.	6.270	6.360	3.530	3.400
700.	6,300	6.440	3.600	3.480
1000.	6.460	6.480	3.660	3.600
1500.	6.530	6.520	3.710	3.670
2000.	6.550	6.540	3.730	3.690
2500.	6.570	6.560	3.750	3.710
3000.	6.580	6.580	3.760	3.730
3500.	6.590	6.590	3.770	3.740
4000.	6.600	6.600	3.780	3.750
4500.	6.610	6.610	3.790	3.760
5000.	6.620	6.620	3.800	3.770

Table 2.2b

Westerly granite. Elastic Wave Velocities.

P(BAR)	VP(DRY)	VP(SAT)	VS(DRY)	VS(SAT)
0.	3.800	5.480	2.800	3.000
20.	4.080	5.530	3.000	3.050
40.	4.450	5.600	3.020	3.070
100.	4.980	5.700	3.070	3.100
150.	5.190	5.740	3.120	3.130
200.	5.310	5.770	3.170	3.150
300.	5.450	5.840	3.230	3.190
400.	5.550	5.900	3.280	3.230
500.	5.610	5.940	3.300	3.260
600.	5.670	5.970	3.330	3.290
700.	5,730	6.010	3.350	3.310
800.	5.770	6.020	3.365	3.325
900.	5.810	6.040	3.380	3.340
1000.	5.850	6.060	3.395	3.350
1100.	5.890	6.070	3.410	3.360
1500.	5.970	6.100	3.450	3.410
2000.	6.060	6.130	3.480	3.440
3000.	6.130	6.170	3.520	3.470
4000.	6.180	6.220	3.530	3.490

Table 2.2c

Troy granite. Elastic Wave Velocities.

P(BAR)	VP(DRY)	VP(SAT)	VS(DRY)	VS(SAT)
20.	4.800	5.899	3.100	3.100
35.	5.183	6.033	3.185	3.185
50.	5.651	6.216	3.233	3.233
100.	5.909	6.224	3.328	3.328
150.	6.044	6.308	3.379	3.379
200.	6.169	6.336	3.424	3.424
250.	6.216	5.348	3.455	3.455
300.	6.272	6.358	3.475	3.475
400.	6.336	6.378	3.511	3.511
500.	6.365	6.398	3.524	3.524
700.	6.428	6.450	3.561	3.561
900.	6.443	6.504	3.575	3.575
1000.	6.449	6.510	3.581	3.581

Table 2.2d

Webatuck dolomite.   Elastic Wave Velocities.

P(BAR)	VP(DRY)	VP(SAT)	VS(DRY)	VS(SAT)
25.	5.145	6.434	3.550	3.409
40.	5.830	6.575	3.720	3.700
50.	5.900	6.600	3.750	3.730
75.	6.150	6.680	3.810	3.780
100.	6.400	6.730	3.840	3.830
150.	6.598	6.769	3.920	3.879
200.	6.686	6.807	3.966	3.931
250.	6.776	6.383	3.990	3.997
300.	6.819	6.856	4.024	4.037
400.	6.870	6.890	4.056	4.068
500.	6.890	6.920	4.062	4.115
600.	6.905	6.940	4.080	4.133
700.	6.919	6.958	4.095	4.153
900.	6.958	6.977	4.115	4.198
1200.	6.965	6.995	4.110	4.220
1500.	6.977	7.026	4.145	4.240
2000.	6.997	7.045	4.161	4.256
2500.	7.016	7.050	4.180	4.270
3000.	7.029	7.090	4.193	4.290

Table 2.2e

Bedford limestone. Elastic Wave Velocities.

P(BAR)	VP(DRY)	VP(SAT)	VS(DRY)	VS(SAT)
30.	2.700	4.600	1.547	1.560
50.	2.794	4.640	1.640	1.680
75.	2.929	4.660	1.690	1.720
100.	3.039	4.680	1.752	1.760
125.	3.113	4.700	1.795	1.810
150.	3.193	4.730	1.841	1.880
200.	3.351	4.760	1.917	1.940
250.	3.500	4.970	1.983	1.970
300.	3.600	4.810	2.040	2.000
400.	3.770	4.820	2.138	2.140
500.	3.912	4.840	2.223	2.230
600.	4.008	4.860	2.283	2.300
800.	4.205	4.880	2.382	2.350
1000.	4.380	4.900	2.466	2.400
1300.	4.598	4.920	2.548	2.510
1700.	4.735	4.490	2.633	2.600
2000.	4.829	4.960	2.681	2.610

Table 2.2f

Solenhofen limestone. Elastic Wave Velocities.

P(BAR)	VP(DRY)	VP(SAT)	VS(DRY)	VS(SAT)
50.	5.607	5.632	3.006	2.994
100.	5.616	5.644	3.014	3.010
200.	5.628	5.671	3.029	3.044
300.	5.637	5.685	3.043	3.050
500.	5.650	5.710	3.063	3.072
700.	5.664	5.732	3.083	3.078
1500.	5.709	5.772	3.103	3.101
2000.	5.724	5.781	3.104	3.103
2500.	5.738	5.787	3.110	3.107
3000.	5.752	5.800	3.115	3.111
3500.	5.757	5.810	3.128	3.124

Table 2.3a

Effective elastic constants of Casco Granite

P(BAR)	G(DRY)	G(SAT)	K(DRY)	K(SAT)	E(DRY)	E(SAT)	NU(DRY)	NU(SAT)
20.	16.41	15.13	10.19	57.85	30.36	44.98	0.003	0.370
25.	17.62	15.62	13.00	58.87	33.48	48.05	0.071	0.364
40.	18.30	16.81	21.74	63.34	40.10	50.07	0.193	0.368
75.	22.69	18.59	31.51	63.97	46.59	60.89	0.254	0.341
100.	23.63	20.43	39.71	63.65	52.34	63.10	0.280	0.335
150.	25.24	23.48	45.85	62.16	60.16	66.67	0.281	0.321
200.	26.23	1.92	49.16	64.05	65.36	69.22	0.278	0.320
250.	26.89	27.57	51.57	64.44	70.19	70.82	0.273	0.317
300.	27.23	28.94	52.81	65.28	73.42	71.71	0.268	0.317
350.	28.41	30.17	54.94	64.68	76.52	74.36	0.268	0.308
430.	29.31	31.43	56.12	64.49	79.46	76.33	0.264	0.303
550.	30.36	32.72	59.61	65.76	82.98	78.91	0.268	0.300
700.	31.80	34.03	58.85	66.51	85.61	82.29	0.258	0.294
1000.	34.03	35.19	62.68	64.89	88.89	86.89	0.264	0.277
1500.	35.37	36.13	63.79	64.47	91.20	89.70	0.262	0.268
2000.	35.77	36.53	63.94	64.65	92.07	90.57	0.260	0.266
2500.	36.13	36.92	64.10	64.81	92.93	91.43	0.258	0.265
3000.	36.53	37.13	64.21	64.99	93.38	92.30	0.258	0.263
3500.	36.74	37.32	64.28	65.07	93.80	92.75	0.257	0.262
4000.	36.92	37.53	64.36	65.15	94.25	93.17	0.256	0.262
4500.	37.13	37.71	64.44	65.23	94.69	93.61	0.255	0.261
5000.	37.32	37.92	64.52	65.31	95.11	94.06	0.254	0.260

Table 2.3b

Westerly granite. Effective elastic constants.

P(BAR)	G(DRY)	G(SAT)	K(DRY)	K(SAT)	E(DRY)	E(SAT)	NU(DRY)	NU(SAT)
0.	20.78	23.85	10.57	47.78	37.66	61.35	-0.094	0.286
20.	23.85	24.65	12.32	48.18	43.49	63.18	-0.089	0.281
40.	24.17	24.96	20.25	49.79	51.86	64.21	0.073	0.285
100.	24.96	25.47	32.41	52.15	59.63	65.69	0.194	0.290
150.	25.78	25.97	36.99	52.71	62.78	66.89	0.217	0.288
200.	26.63	26.29	39.22	53.16	65.14	67.71	0.223	0.288
300.	27.64	26.98	41.84	54.43	67.97	69.43	0.229	0.287
400.	28.51	27.64	43.62	55.39	70.23	71.10	0.232	0.286
500.	28.86	28.17	44.92	55.94	71.31	72.35	0.235	0.284
600.	29.39	28.67	46.00	56.21	72.69	73.54	0.237	0.282
700.	29.73	29.04	47.36	57.00	73.78	74.47	0.240	0.282
800.	30.00	29.31	48.23	56.98	74.54	75.02	0.242	0.281
900.	30.26	29.57	49.08	57.27	75.34	75.66	0.244	0.280
1000.	30.55	29.73	49.95	57.66	76.11	76.13	0.246	0.280
1100.	30.82	29.92	50.85	57.74	76.90	76.53	0.248	0.279
1500.	31.54	30.82	52.39	57.53	78.81	78.44	0.249	0.273
2000.	32.09	31.35	54.54	57.77	80.48	79.66	0.254	0.270
3000.	32.83	31.91	55.81	58.33	82.36	80.96	0.254	0.269
4000.	33.02	32.28	57.19	59.49	83.08	81.99	0.258	0.270

Table 2.3c

Troy granite. Effective elastic constants.

P(BAR)	G(DRY)	G(SAT)	K(DRY)	K(SAT)	E(DRY)	E(SAT)	NU(DRY)	NU(SAT)
20.	25.47	25.37	27.01	57.74	57.95	66.40	0.142	0.308
35.	26.77	26.77	35.22	60.38	64.10	69.99	0.197	0.307
50.	27.59	27.59	47.52	65.21	69.35	72.55	0.257	0.315
100.	29.25	29.25	53.20	63.28	74.13	76.01	0.268	0.300
150.	30.15	30.15	56.26	64.86	76.72	78.30	0.273	0.299
200.	30.94	30.94	59.19	64.71	79.07	80.10	0.277	0.294
250.	31.52	31.52	59.98	64.36	80.47	81.29	0.276	0.290
300.	31.89	31.89	61.35	64.20	81.52	82.05	0.279	0.287
400.	32.55	32.55	62.59	63.99	83.21	83.48	0.278	0.283
500.	32.79	32.79	63.25	64.36	83.87	84.08	0.279	0.282
700.	33.48	33.48	64.44	65.18	85.62	85.75	0.279	0.281
900.	33.74	33.74	64.60	66.69	86.22	86.62	0.278	0.284
1000.	33.84	33.84	64.65	66.74	86.46	86.88	0.277	0.283

Table 2.3d

Webatuck dolomite. Effective elastic constants.

P(BAR)	G(DRY)	G(SAT)	K(DRY)	K(SAT)	E(DRY)	E(SAT)	NU(DRY)	NU(SAT)
25.	33.26	33.35	27.75	74.33	87.05	75.65	0.046	0.305
40.	39.72	39.29	44.60	71.69	99.68	91.87	0.157	0.268
50.	40.35	39.92	46.09	71.78	101.05	93.73	0.161	0.265
75.	41.67	41.01	53.01	73.39	103.69	99.04	0.189	0.264
100.	42.33	42.10	61.13	73.85	106.13	103.15	0.219	0.260
150.	44.11	43.19	66.15	73.93	108.43	108.26	0.227	0.256
200.	45.15	44.34	68.11	73.85	110.87	110.93	0.229	0.250
250.	45.69	45.86	70.86	73.07	113.77	112.82	0.235	0.240
300.	46.47	46.78	71.49	72.52	115.49	114.60	0.233	0.235
400.	47.21	47.50	72.50	72.93	117.07	116.38	0.232	0.232
500.	47.36	48.59	73.10	72.64	119.22	116.84	0.234	0.226
600.	47.79	49.02	73.13	72.87	120.14	117.70	0.232	0.225
700.	48.13	49.51	73.21	72.96	121.11	118.44	0.230	0.223
900.	48.59	50.57	74.16	72.27	123.04	119.65	0.231	0.216
1200.	48.47	51.11	74.59	72.30	124.07	119.54	0.233	0.214
1500.	49.31	51.60	73.96	72.87	125.25	121.03	0.227	0.214
2000.	49.68	51.98	74.25	73.13	126.08	121.89	0.226	0.213
2500.	50.14	52.32	74.42	72.87	126.65	122.84	0.225	0.210
3000.	50.45	52.81	74.53	73.85	127.94	123.50	0.224	0.211

Table 2.3e

Bedford limestone. Effective elastic constants.

P(BAR)	G(DRY)	G(SAT)	K(DRY)	K(SAT)	E(DRY)	E(SAT)	NU(DRY)	NU(SAT)
30.	6.86	6.37	10.74	46.95	15.75	18.29	0.256	0.435
50.	7.05	7.39	11.06	46.56	17.45	21.06	0.237	0.425
75.	7.49	7.76	12.50	46.56	18.71	22.03	0.250	0.421
100.	8.04	8.12	13.47	46.56	20.12	23.00	0.251	0.418
125.	8.44	8.59	14.12	46.43	21.12	24.26	0.251	0.413
150.	8.88	9.25	14.88	46.27	22.22	26.04	0.251	0.406
200.	9.62	9.85	16.58	46.22	24.21	27.61	0.257	0.400
250.	10.30	10.17	18.37	46.56	26.04	28.43	0.264	0.398
300.	10.90	10.48	19.41	46.64	27.56	29.24	0.264	0.395
400.	11.97	12.00	21.27	44.88	30.26	33.04	0.263	0.377
500.	12.94	13.02	22.82	44.02	32.67	35.58	0.262	0.365
600.	13.65	13.86	23.87	43.41	34.40	37.57	0.260	0.356
800.	14.86	14.46	26.51	43.10	37.57	39.04	0.264	0.349
1000.	15.93	15.09	29.03	42.78	40.40	40.51	0.268	0.342
1300.	17.00	16.51	32.72	41.42	43.49	43.70	0.278	0.324
1700.	18.16	17.71	34.53	40.32	46.35	46.35	0.276	0.308
2000.	18.84	17.84	36.00	40.66	48.10	46.71	0.277	0.309

48.

Table 2.3f

Solenhofen limestone. Effective elastic constants.

P(BAR)	G(DRY)	G(SAT)	K(DRY)	K(SAT)	E(DRY)	E(SAT)	NU(DRY)	NU(SAT)
50.	24.04	23.84	51.59	52.59	62.40	62.14	0.298	0.303
100.	24.16	24.10	51.68	52.61	62.73	62.72	0.298	0.301
200.	24.40	24.65	51.72	52.69	63.26	63.96	0.296	0.298
300.	24.63	24.74	51.69	52.98	63.76	64.23	0.294	0.298
500.	24.96	25.10	51.65	53.26	64.48	65.08	0.291	0.296
700.	25.28	25.20	51.63	53.80	65.20	65.39	0.289	0.297
1500.	25.61	25.58	52.56	54.52	66.09	66.36	0.290	0.297
2000.	25.63	25.61	52.99	54.76	66.20	66.47	0.292	0.298
2500.	25.73	25.68	53.28	54.85	66.48	66.63	0.292	0.197
3000.	25.81	25.74	53.60	55.16	66.71	66.83	0.292	0.298
3500.	26.03	25.96	53.47	55.18	67.17	67.32	0.290	0.297

Figure Captions

Fig. 2.1   .Transducer assembly.   The sample is mounted
between two transducer assemblies. A piano
wire spring is wrapped around the sample to
provide space for the water which is expelled
from the saturated sample by pressure.

Fig. 2.2.   The velocity of compressional waves in Chelms-
ford granite, initially saturated with water,
as a function of time.   The sample was subject
to room temperature, pressure, and humidity.
The decrease of V_p is caused by the slow evapora-
tion of the water.

Fig. 2.3   Velocity of elastic waves in rock samples as
a function of pressure. The compressional wave
velocity depends significantly on the degree
of saturation but shear wave velocity is almost
independent of saturation.   These observations
are made for (a) Casco granite (b) Westerly
granite (c) Troy granite (d) Webatack dolomite
(e) Bedford limestone and (f) Solenhoffen
limestone.

Fig. 2.4   Elastic moduli of dry and saturated rocks.   The
bulk modulus of saturated rock samples is
almost identical to the intrinsic value of rock
without cracks.   The bulk modulus of the dry

rock increases with pressure. The shear moduli of the dry and saturated samples are almost identical. Young's modulus depends somewhat on saturation. Poisson's ratio is high in saturated rocks and very low in dry ones. Values are for (a) Casco granite (b) Westerly granite (c) Troy granite (d) Webatack dolomite (e) Bedford Limestone.

Fig. 2.5 Compressional wave velocity in a dry sample of Bedford limestone vs. hydrostatic pressure. At P = 2 kb round pores begin to collapse. They act like cracks when pressure is reduced.

Fig. 2.6 Difference between V_p in dry and saturated granites vs. crack porosity. Size of rectangles indicates experimental uncertainties.

ELECTRICAL LEADS

TRANSDUCER UNIT

TRANSDUCER

COPPER FOIL

SPRING

SAMPLE

RUBBER JACKET

RECEIVER UNIT
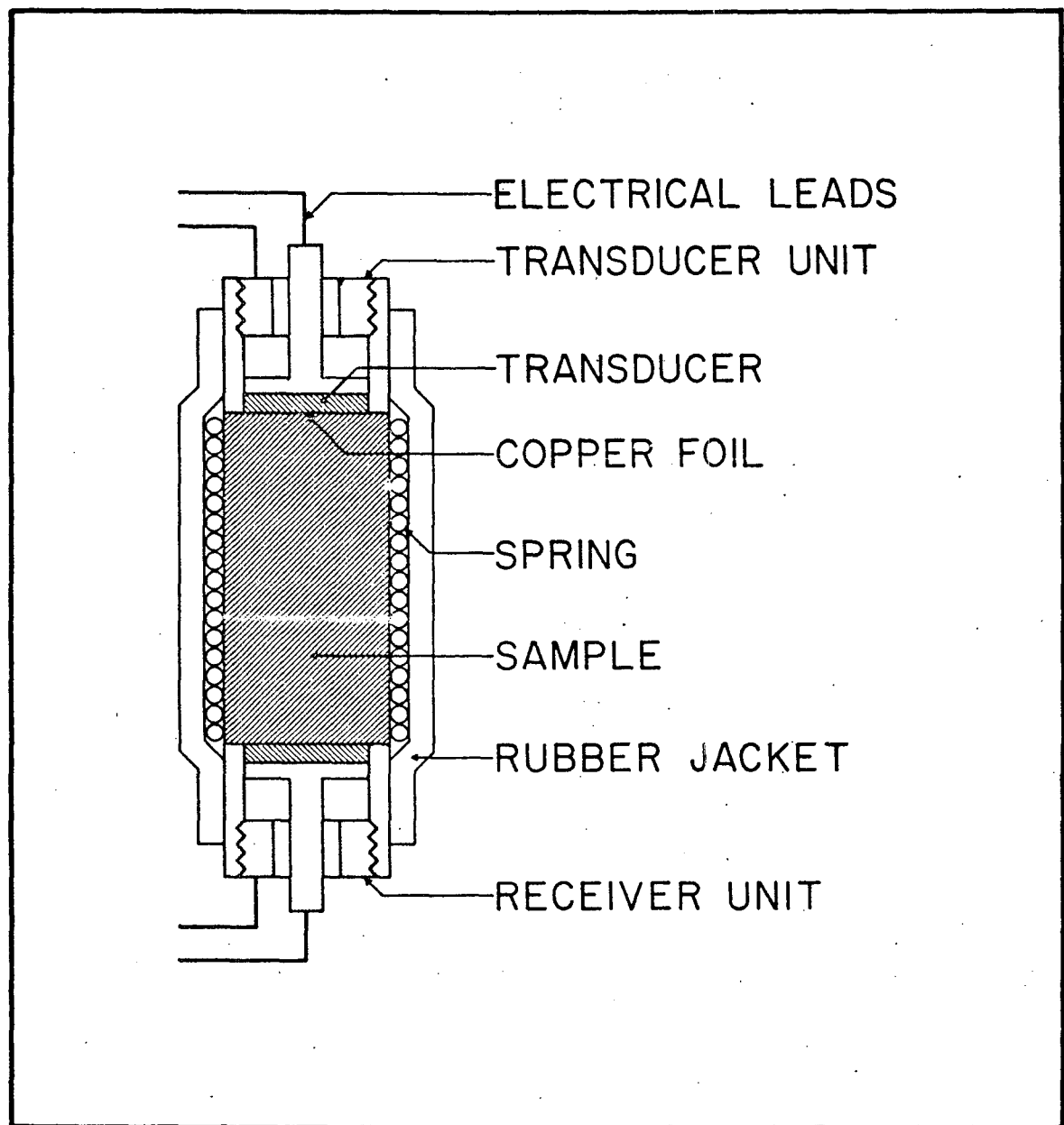
FIG 2.1
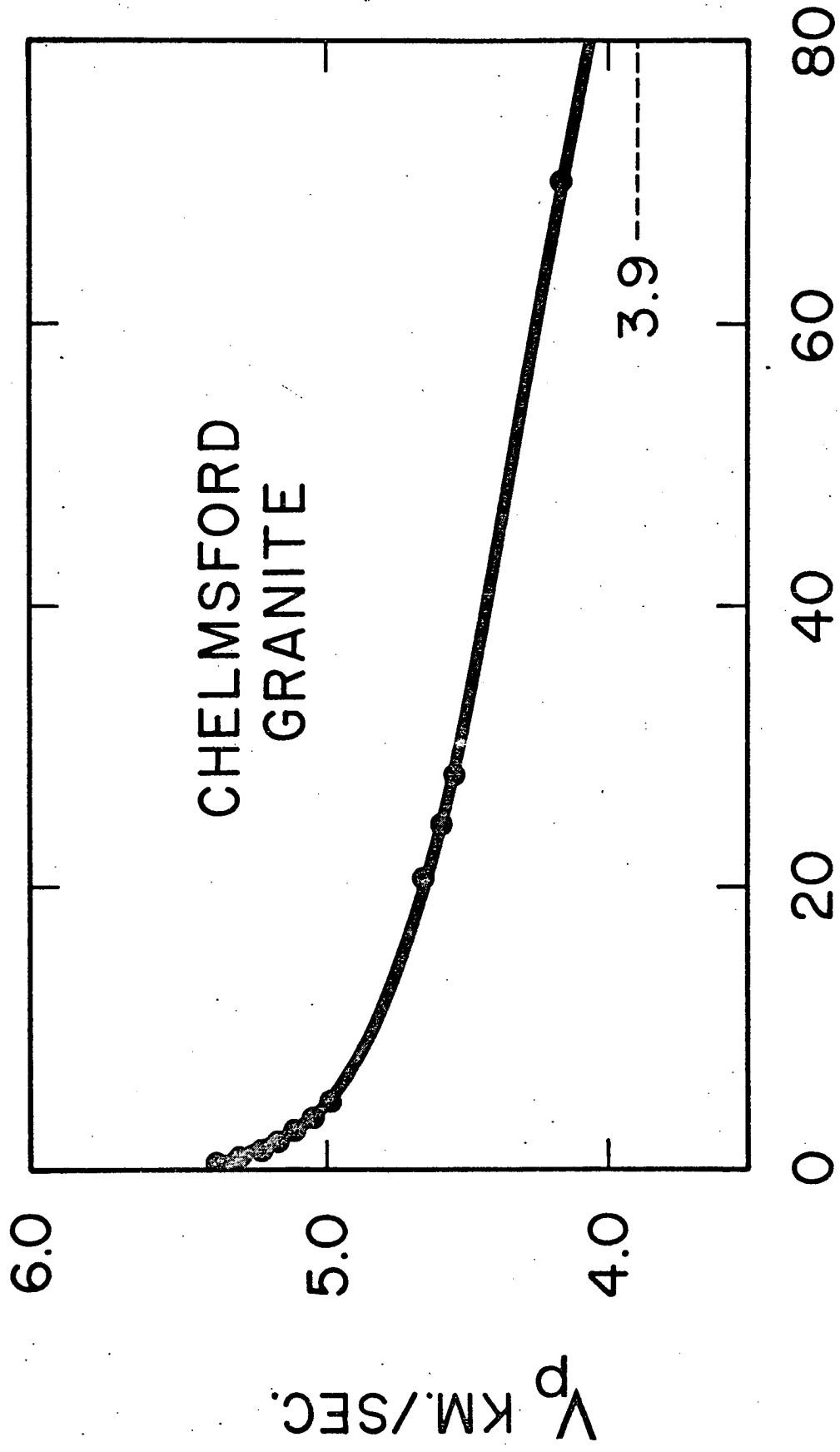
FIG 2.2 TIME (HOURS)
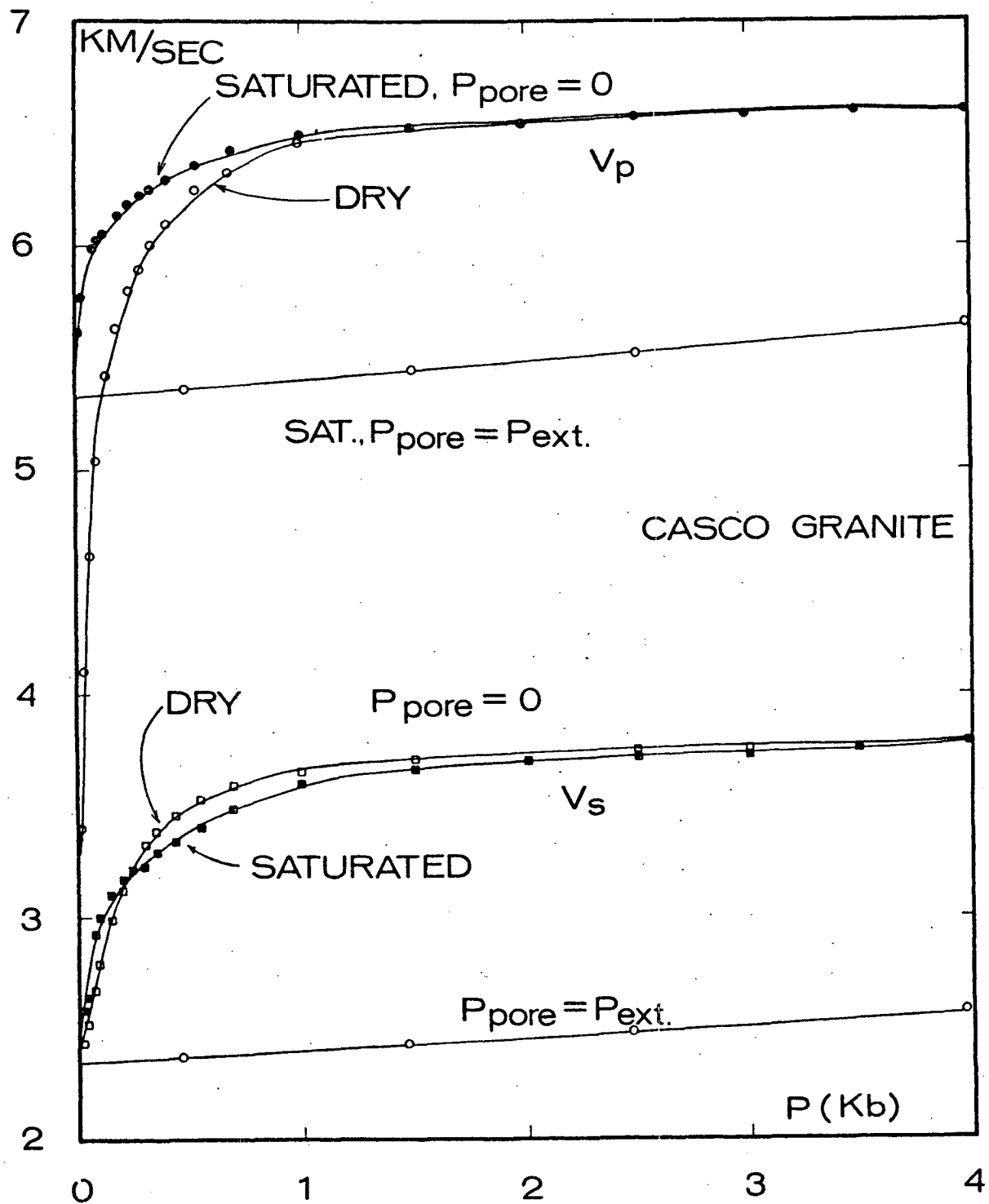
FIG 2.3a
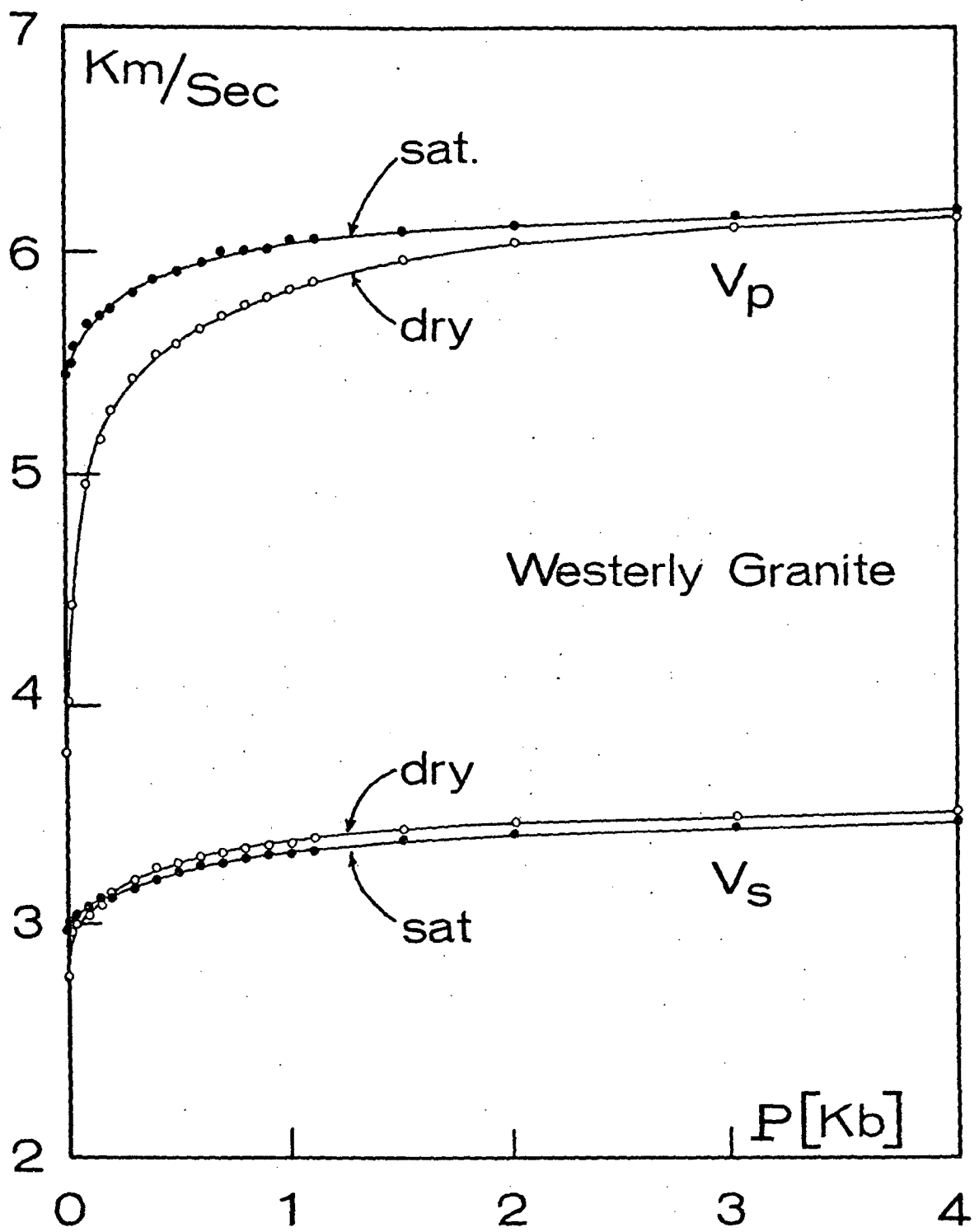
Fig 2.3 b
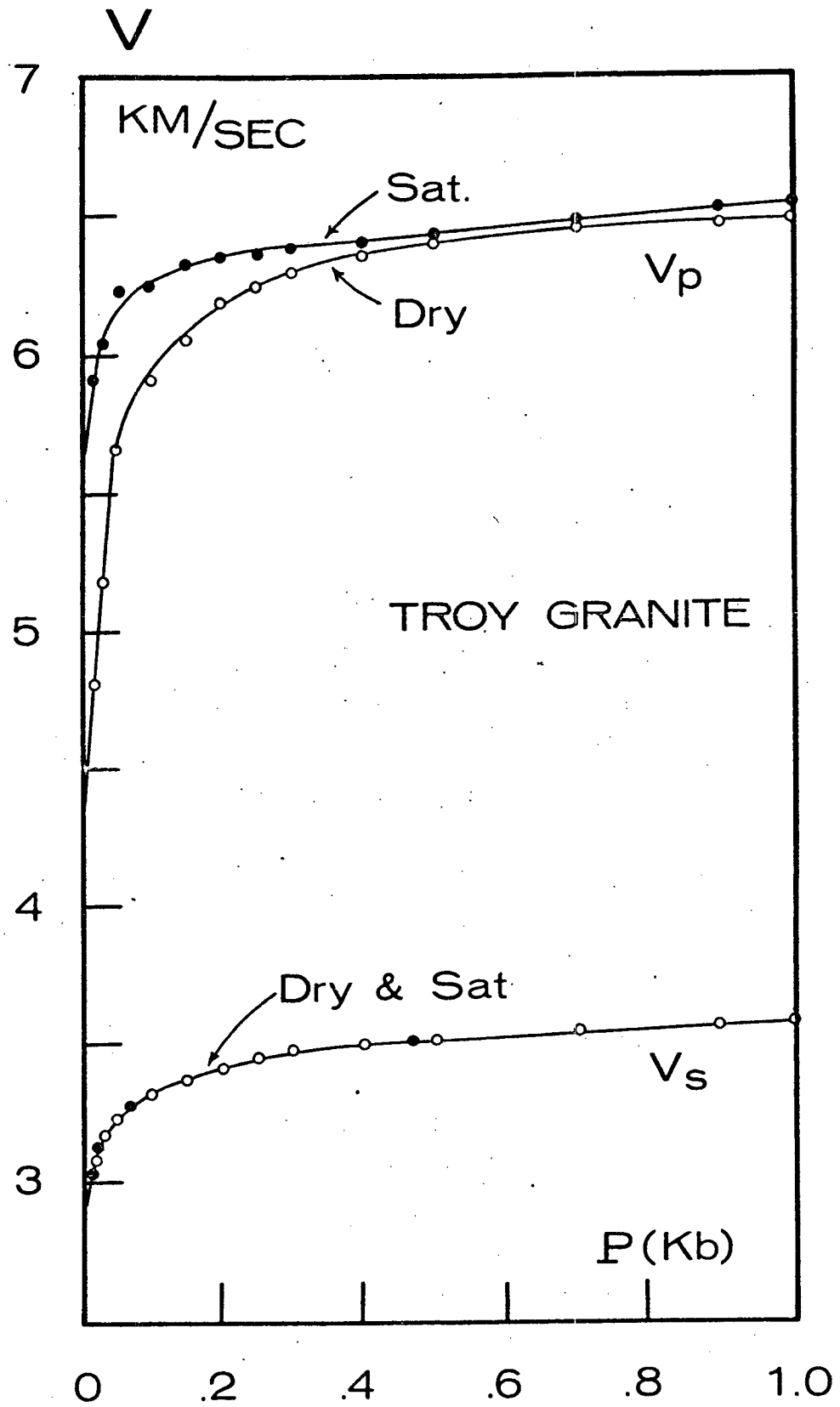
Fig 2.3 c
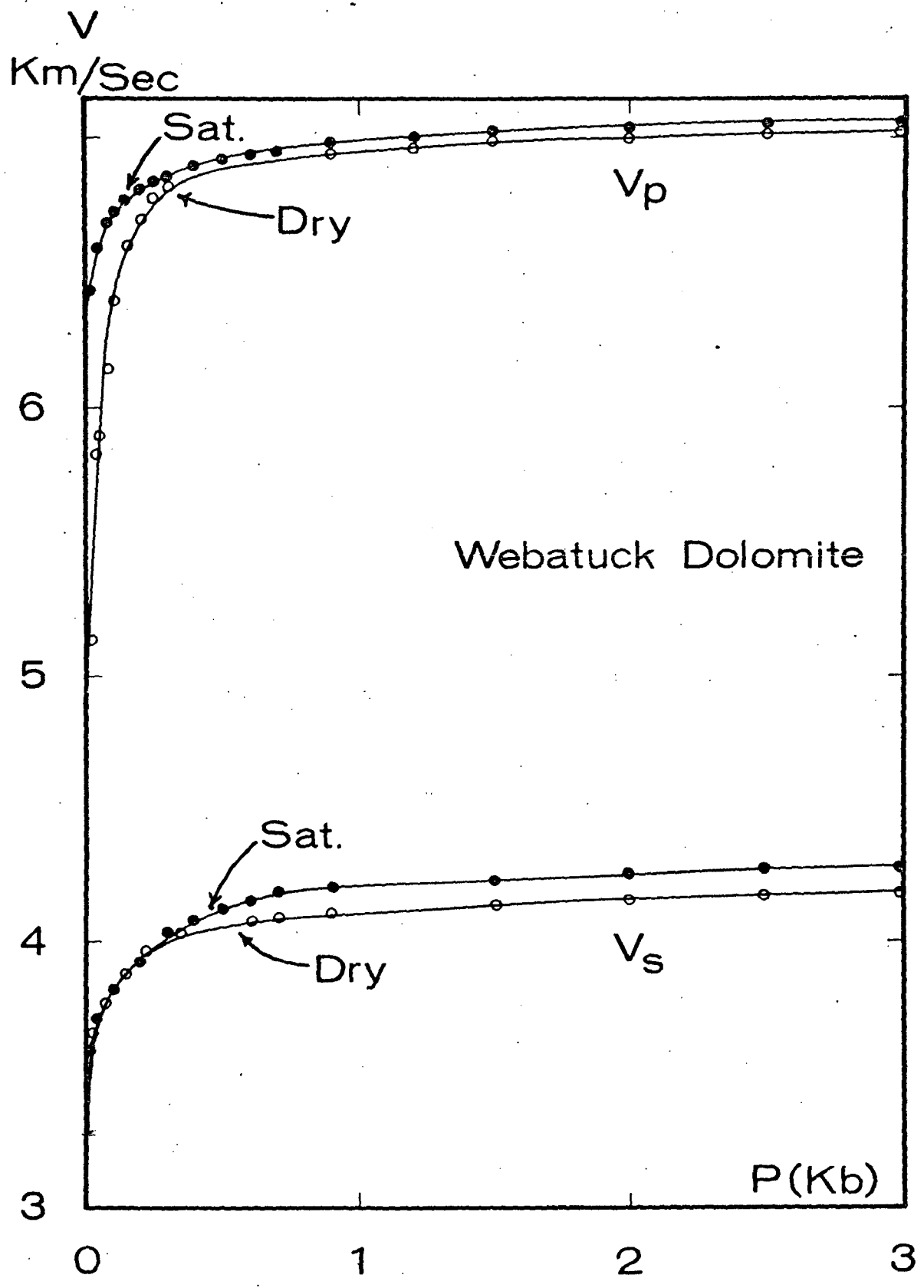
Fig 2.3 d
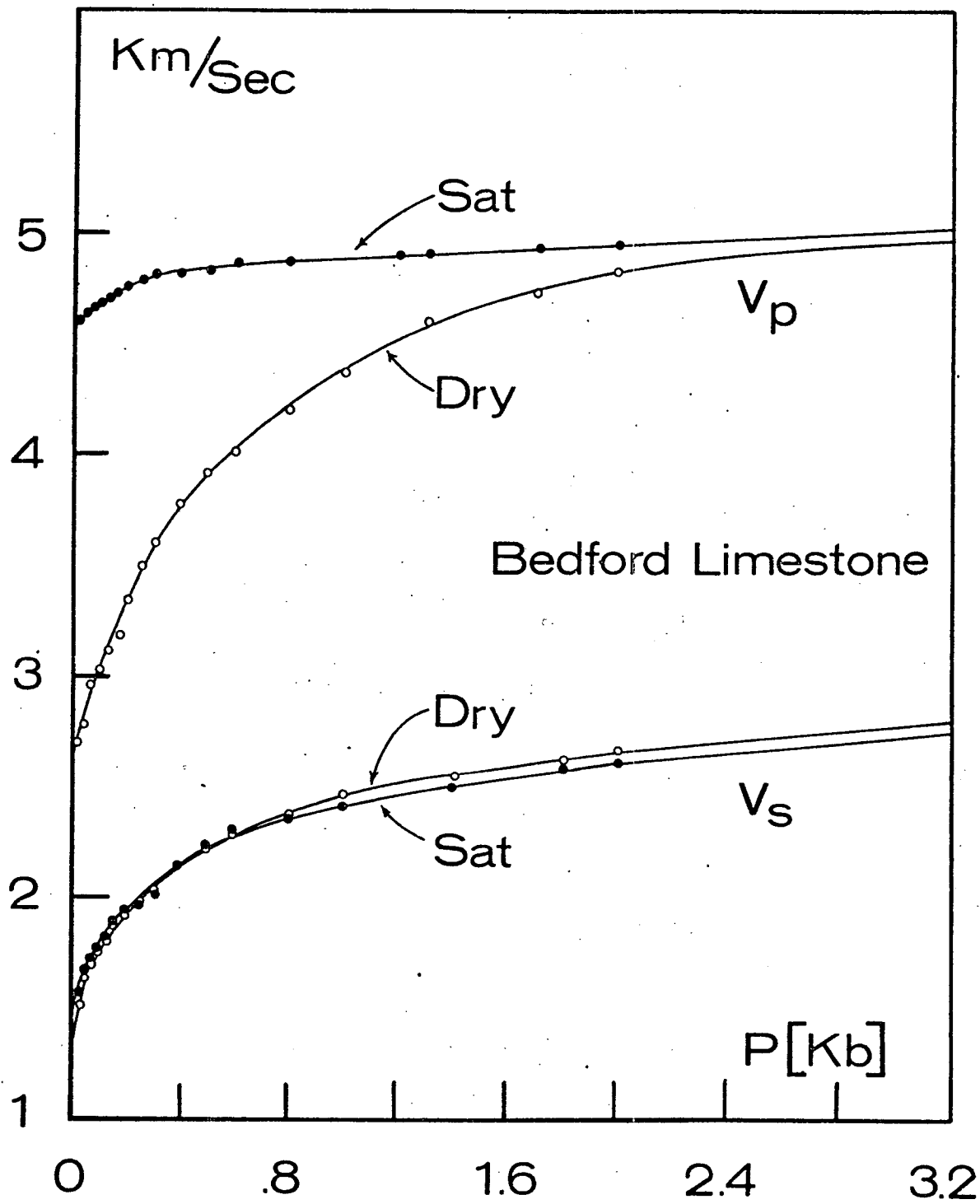
Fig 2.3e
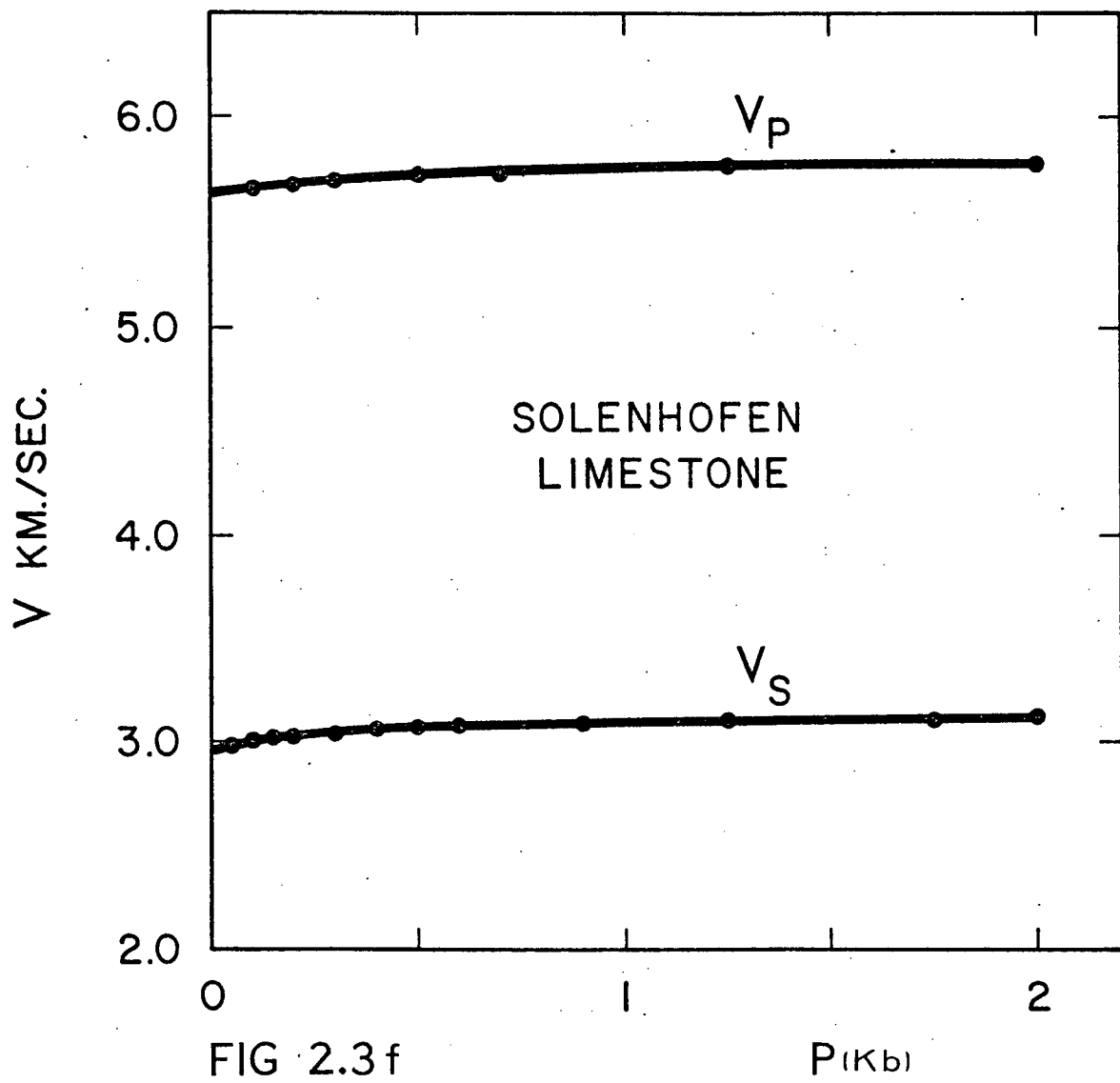
FIG 2.3 f
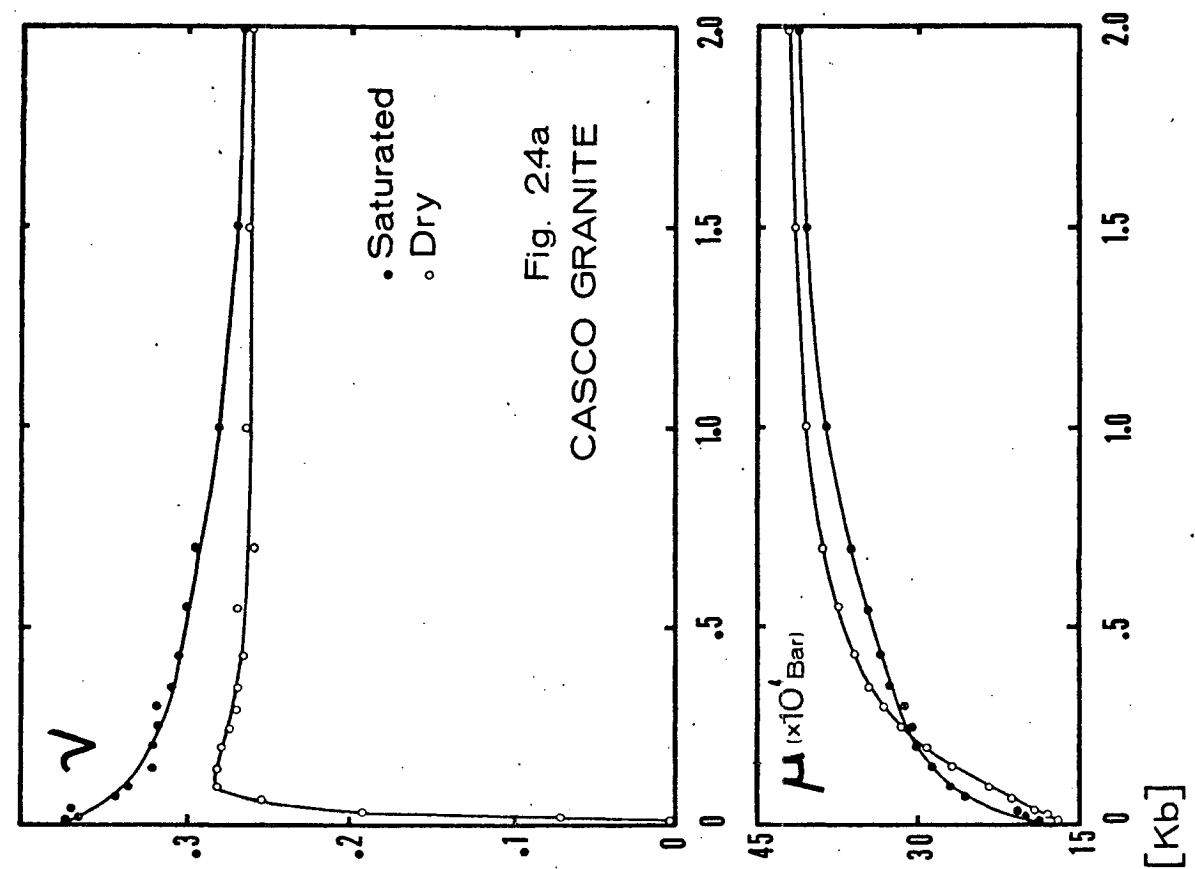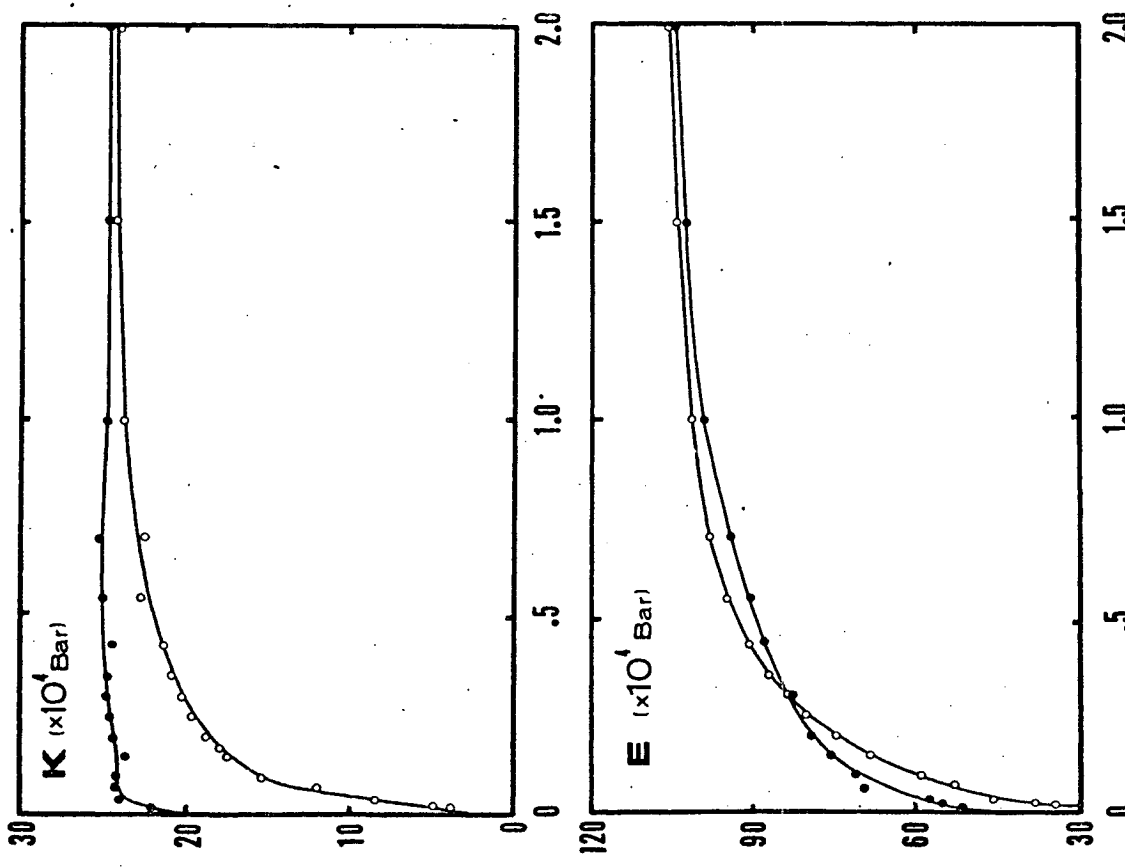
Fig. 24a
CASCO GRANITE

• Saturated
○ Dry

Fig. 24b

WESTERLY GRANITE
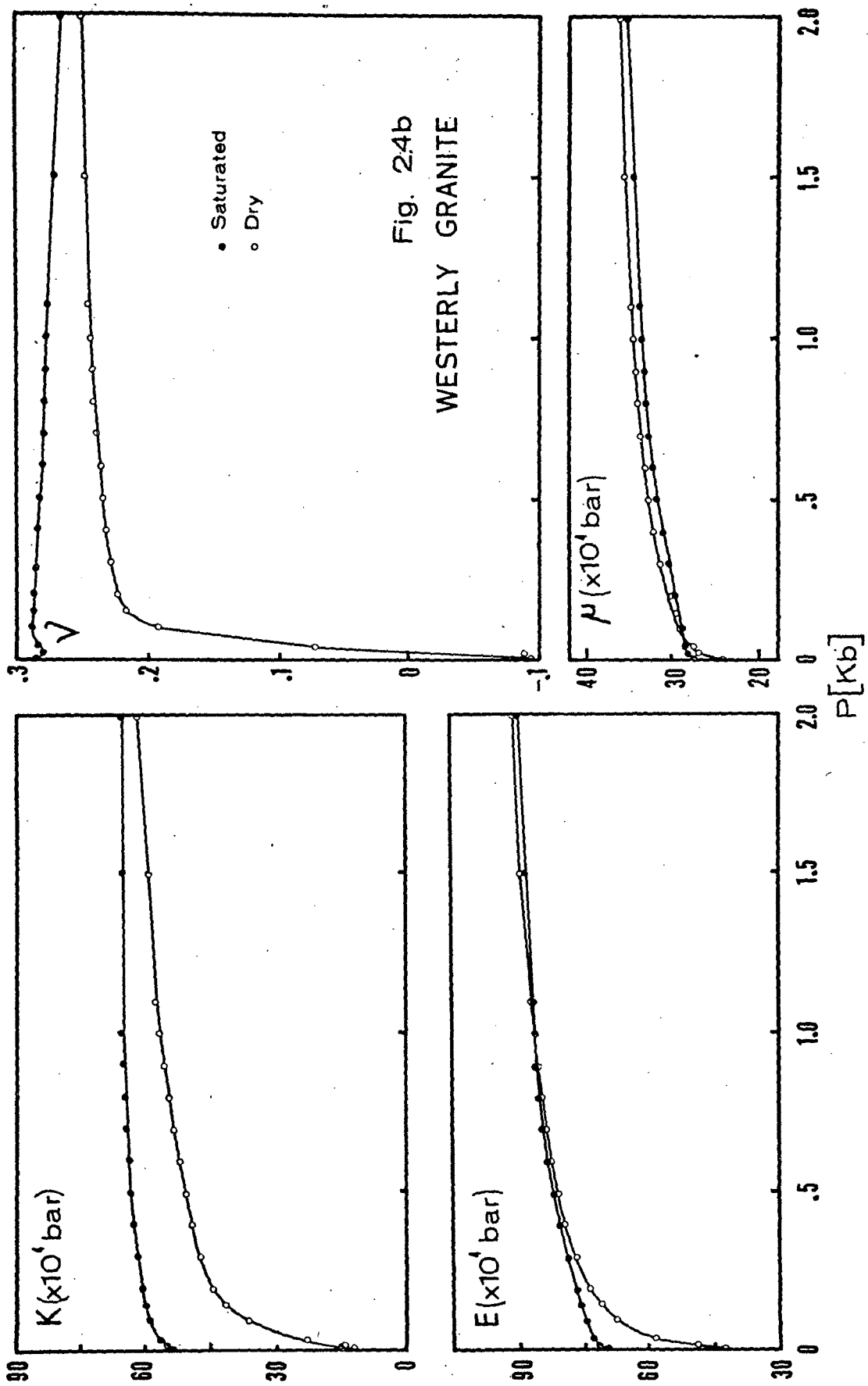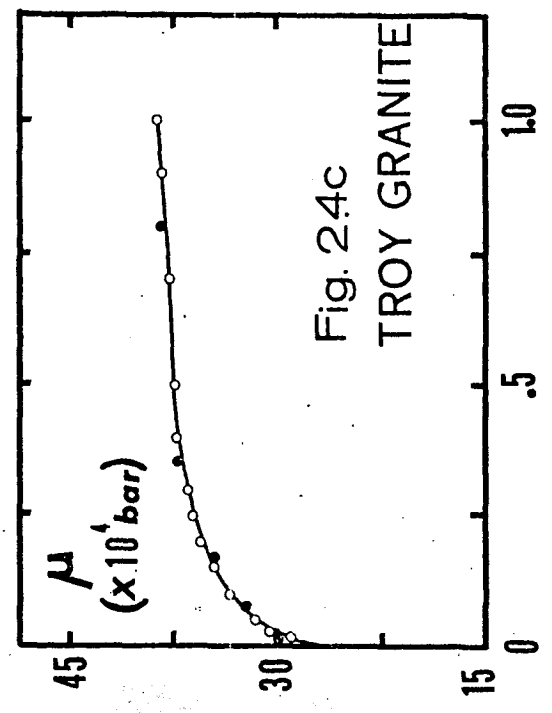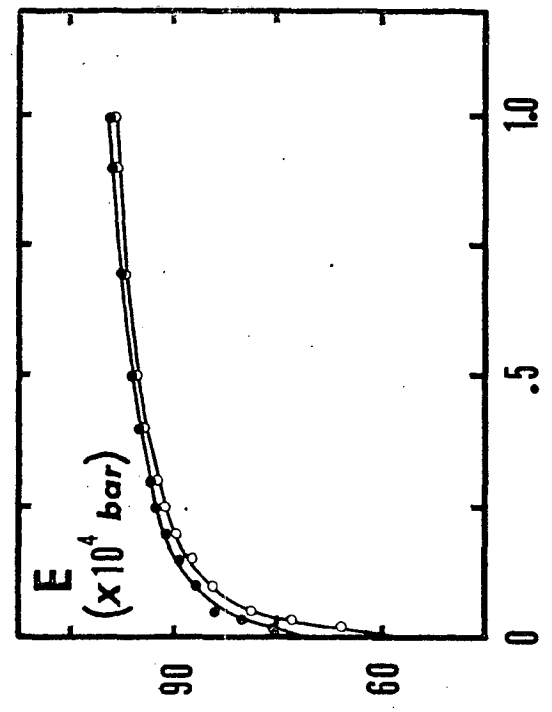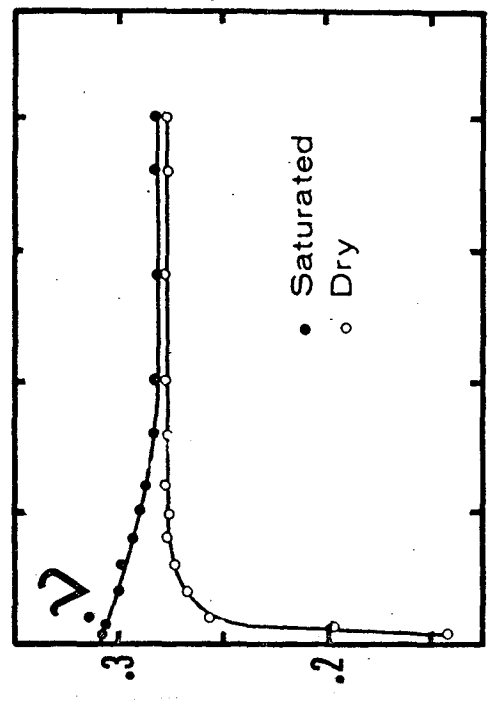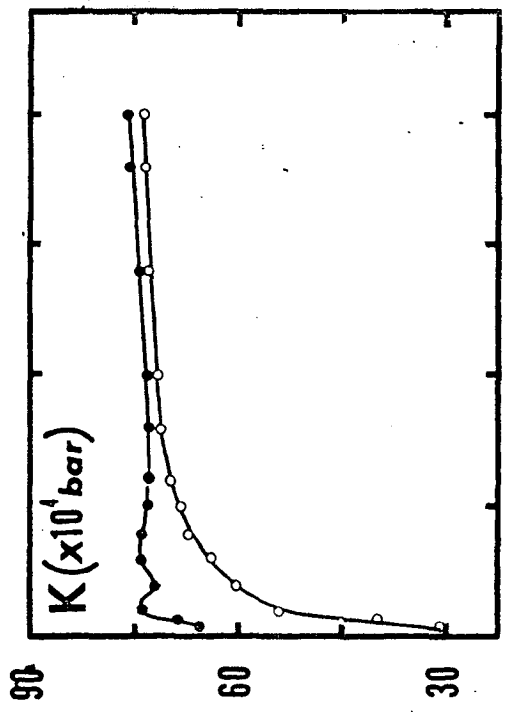
• Saturated
○ Dry

Fig. 24c
TROY GRANITE

FIG. 2.4d

WEBATUCK DOLOMITE
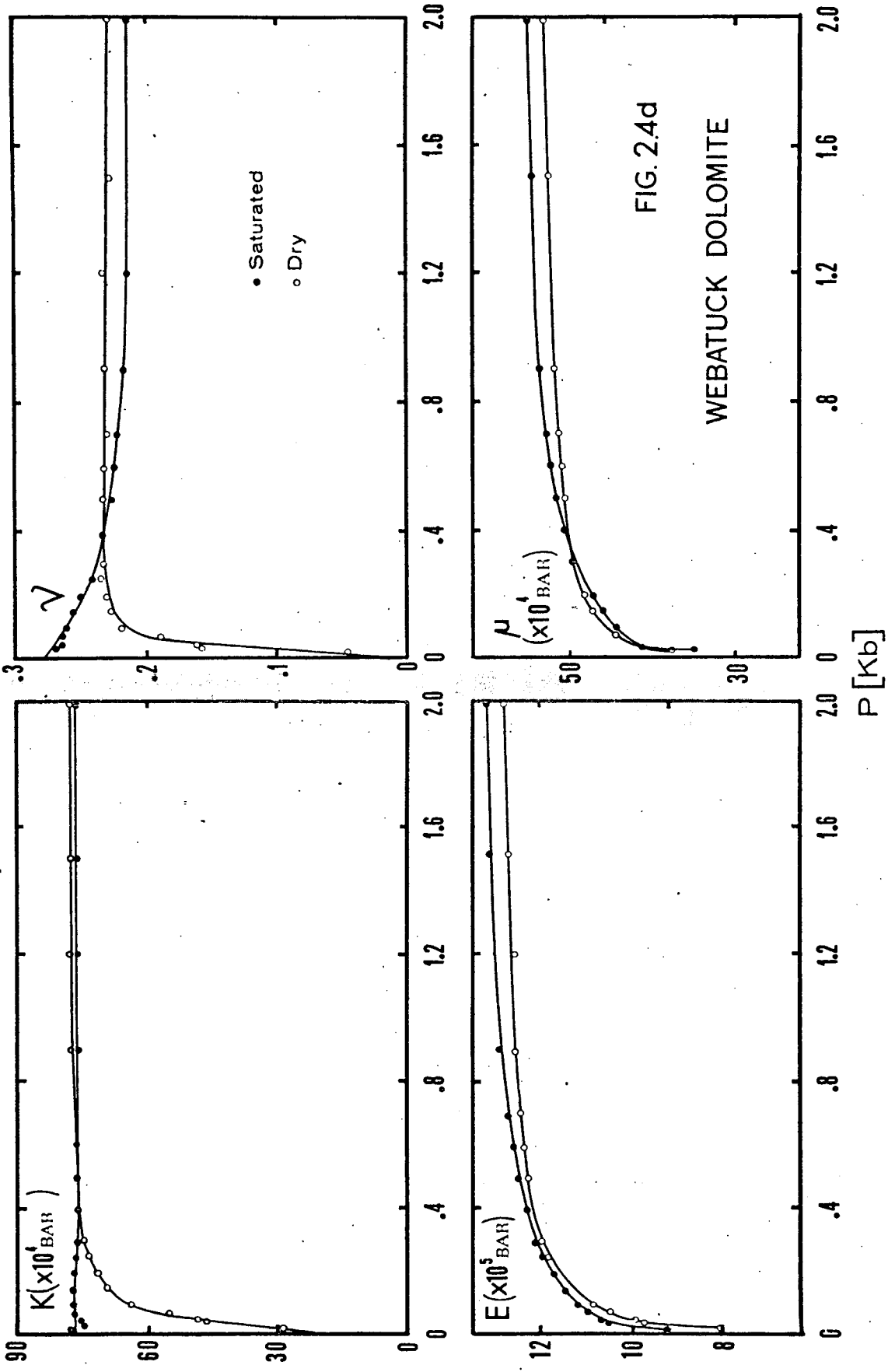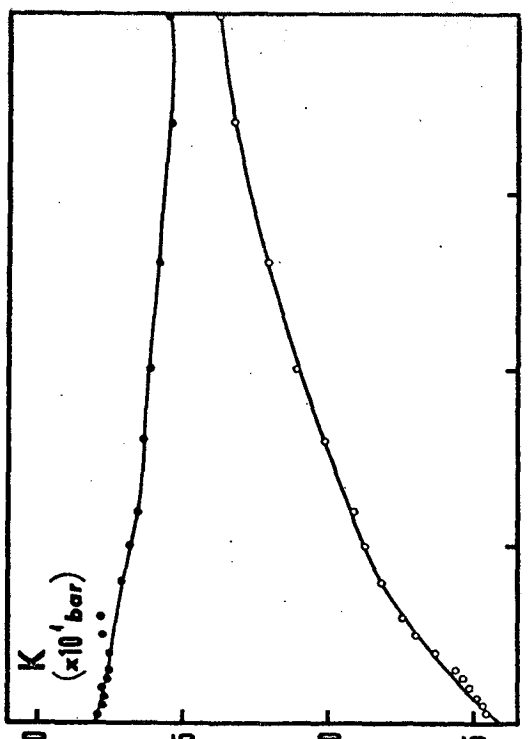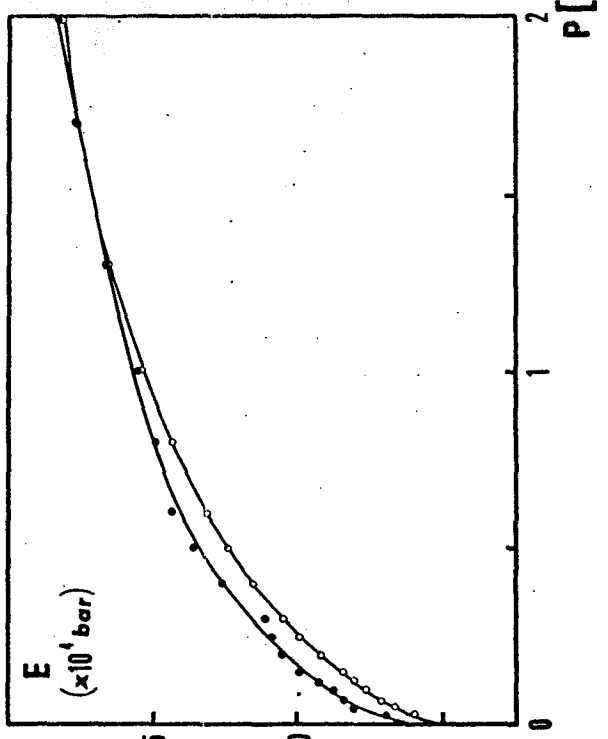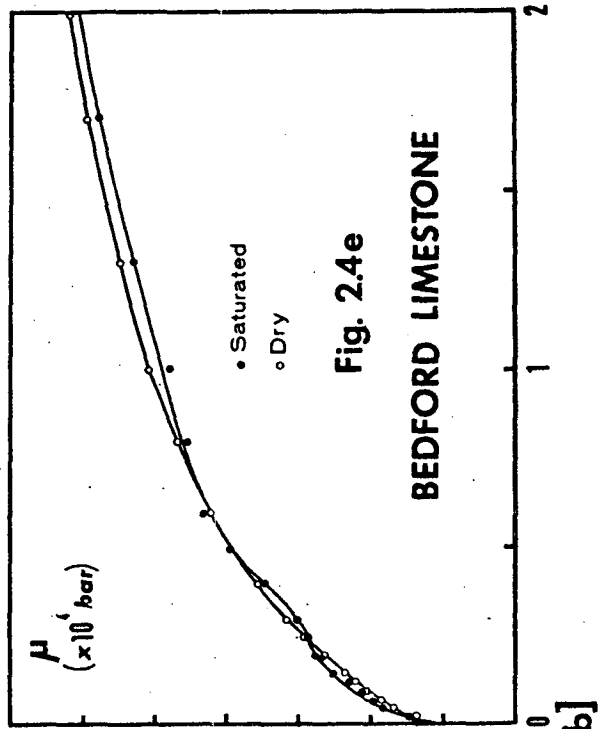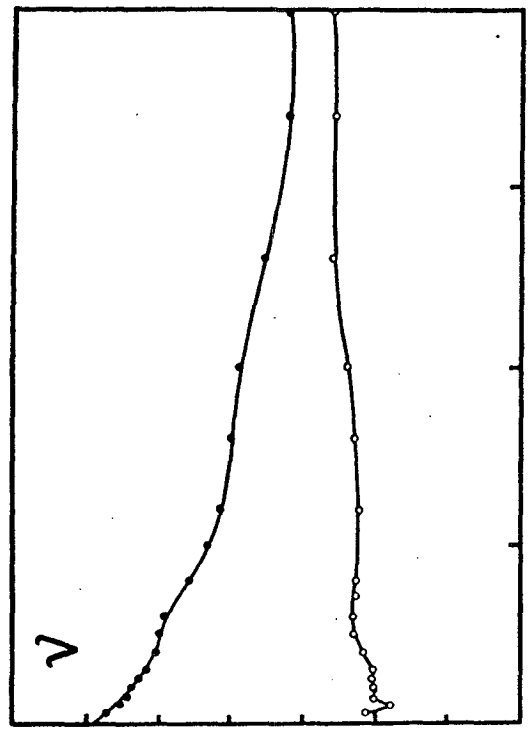
Fig. 2.4e

BEDFORD LIMESTONE

FIG 2.5

BEDFORD
LIMESTONE

$V_P \left(^{KM}/_{SEC}\right)$

P(KILOBAR)
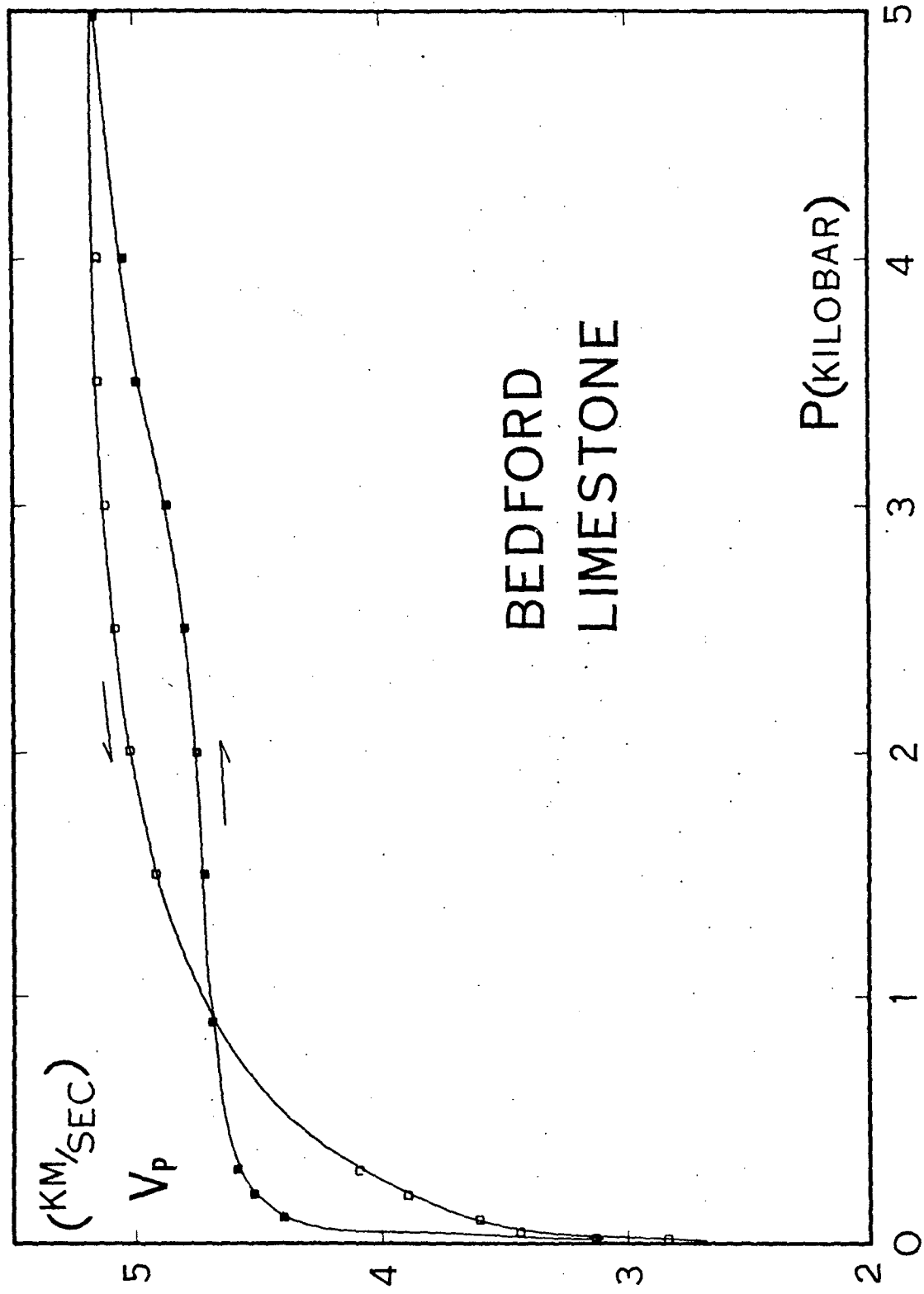
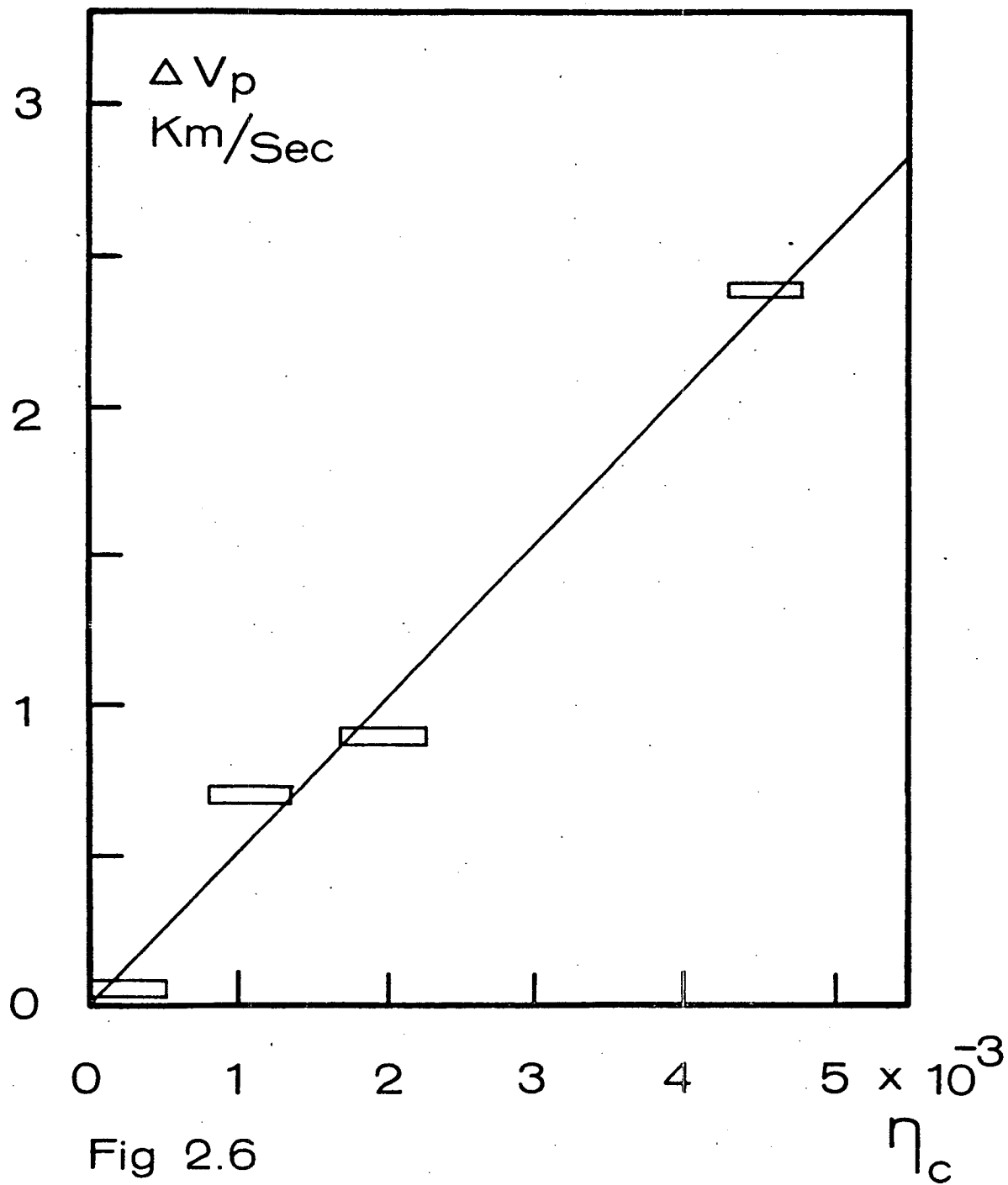Fig 2.6

Chapter 3

Effects of Viscous Fluid Inclusion on the

Propagation of Waves in Rock and Applications

to the Earth

1. Introduction

An understanding of the mechanical behavior of fluid-
filled rocks of low porosity is important in geophysics for
the correct interpretation of the elastic properties of the
earth's crust and mantle. We previously reported data on
the effects of saturation in rocks (Chapt. 2). In this chapter
we discuss the effects of viscosity on the propagation of
waves in low porosity aggregates. The results have inter-
esting implications on the effects of partial melt such as
may occur in the Upper Mantle.

Several authors have studied the effects of inclusions
of air, water, and low viscosity organic oils. Aside from
the effect of fluid pore pressure, the replacement of air
by water in high porosity rocks causes an increase of
compressional velocity and a decrease of shear velocity.
King (1) investigated the effects of air, salt water and
kerosene. His results indicated that V_p was commonly
highest when the saturating fluid was salt water while the
corresponding shear velocity was lowest. The dry rocks on
the other hand had low V_p but relatively high V_s, similar
to those observed in rocks saturated with kerosene.

Replacement of air with liquid in a high porosity

rock affects several important parameters such as density, effective elastic moduli, and the viscosity of the fluid phase. In such low porosity rocks as granites the change of the bulk density is negligible but the changes of the effective elastic moduli are large. Nur (2) reported that V_p increases greatly while V_s remains unchanged in a number of granite samples upon saturation with water. Dortmann and Magid (3) reported similar observations on various igneous rocks. The effective bulk modulus of the saturated rock was almost identical to that of the rock without porosity but the effective dynamic bulk modulus of dry rock was very low and increased rapidly with external pressure (which causes cracks to close).

Timur (4) observed a velocity increase in rock saturated with water as the water froze. Spetzler and Anderson (5) using ice aggregates noticed large decrease of both V_p and V_s when partial melt first appeared. Born (6) found that internal friction ϕ in a specimen of the Amherst sandstone increased with increasing water content and depended on frequency. Gordon and Davis (7) also noticed that ϕ is dependent on the presence of fluid, its viscosity and wave frequency. Garanin (8) found a nonlinear increase of absorption coefficient and wave velocity with increasing viscosity over a limited range of viscosity.

The introduction of a liquid phase replacing either air or solid involves changes of both viscosity and bulk

modulus of the inclusion. It is however, important to investigate the influence of these two parameters independently. Here the effects of viscosity are reported.

2. Experimental procedure

A large range of viscosity must be used to show the influence of viscosity on velocities and attenuation. All other parameters should preferably remain constant. For this experiment two core samples of Barre granite were used, one for the measurement of V_p and the other for V_s, with various fluids in the microcracks. The properties of this granite are summarized in Table 3.1. The measurement techniques are identical to those used previously by us (Chapter 2) and similar to those used by Birch (9) and Simmons (10). Barium titanate transducers (PZT 4), 0.10" thick, attached to the specimen with an electrically conducting epoxy (Traduct BA-2902, manufactured by the Tracon Co., Medford, Mass.) which hardened to 70°C for 12 hours were used for generating compressional waves. AC-cut quartz transducers (gold-plated, coaxial, manufactured by the Valpey Co., Holliston, Mass.) to generate shear waves were mounted on the second core with a non-conducting epoxy (Trabond BA2101). Agreement of the V_p of the two samples measured at room conditions before the transducers were attached was better than 1%, indicating that the two cores had similar elastic properties and could be assumed identical.

Variation of the viscosity of the fluid in the micro-

cracks is obtained by the use of glycerol, $C_3H_5(OH)_3$, at various temperatures, together with water and air. The viscosity of glycerol, unusually sensitive to temperature is shown in fig. 3.1. A change of temperature from -77^oC to 100^oC changes the viscosity of the glycerol by ten orders of magnitude. The compressibility of glycerol changes by a factor of only three over the temperature range -77^oC to $+100^oC$ despite the very large change in viscosity (11). In the measurements of glycerol-saturated rock, each sample was immersed in a constant temperature bath filled with methanol dry ice mixtures. Temperatures were measured with an iron-Constantan thermocouple which was attached to the specimen and therefore indicated the temperatures at the outer surface. Repeated readings in separate runs indicated that temperature was determined within 1^oC resulting in a corresponding approximate error in viscosity of 2%, a value sufficiently small to be neglected. The added measurements with water and air in the microcracks of the rocks provide a range of viscosities from 10^{-4} to 10^9 poise. For comparison, the viscosity of molten basalt is 10^5-10^7 poise (12).

The effects of temperature on the intrinsic properties of the solid phases of the rock can be neglected. Velocities in the two samples subject to temperatures from -77^oC to $+100^oC$ and air dried change significantly less than in the glycerol saturated samples. Changes of sample length due

to thermal strains are also small and were neglected.

Techniques of saturating the specimen were similar to those used previously by us (Chapter 2) and described by Brace (13). Drying was done at about 90°C in a vacuum furnace. For saturation with glycerol, the container was kept at 90°C-100°C for 36 hours. Gas pressure of 10 bars was applied and removed a few times to facilitate the flow of glycerol into the cracks. Although the degree of saturation of the samples was not tested, the results of Brace (14) indicate that the saturation with water is very high. The viscosity of glycerol at 100°C is about 15 times that of water. Dortmann and Magid (3) found that saturation of igneous rocks with machine oil took 4-5 times longer than with water. The fact that viscosity of glycerol at 100°C is comparable with that of oil and that glycerol also wets silicates, suggests that the degree of saturation should be comparable with that of water.

The velocities measured as a function of increasing temperature with glycerol in the cracks were compared with the velocities obtained as a function of decreasing temperature. The apparent reversibility suggested that the temperature distribution in the sample was sufficiently steady and uniform when a measurement was made.

Rough estimates of the effects of the viscosity of the saturating fluid on the attenuation of elastic waves were obtained by holding constant the input voltage to the

transducers and comparing the output voltage throughout each temperature cycle. The variation of voltage between measurements did not exceed 10% and was probably, on the average, only a few percent. The dominant frequency in the received signals was approximately $\frac{1}{2}$ Mh for both compressional and shear waves.

3. Wave velocities, relative attenuation, and elastic constants.

The data obtained on V_p and V_s in our experiment are given in Table 3.2, together with the effective elastic properties of Young's modulus, bulk modulus, shear modulus, and Poisson's ratio calculated from V_p and V_s. In visco-elastic materials with large internal friction, the velocities depend not only on shear and bulk moduli but also on ϕ 15). Although the absolute value of ϕ is not known, in our experiment the large relative value at the peak suggests that internal friction should perhaps not be neglected in computing the *true* effective elastic constants. The large value of ϕ also implies that a discrepancy between static and dynamic elastic constants may exist over some viscosity range.

The dependence of V_p and V_s on the viscosity of the fluid that fills the microcracks in the Barre granite is shown in fig. 3.2. The values are those measured on the glycerol saturated rock except at the very low viscosity range where values were obtained with water ($\eta = 10^{-2}$

poise) and air ($\eta = 1.3 \cdot 10^{-4}$ poise). The value of V_p obtained on a dry sample, 3.93 km/s, is much lower than the values for rock saturated with water of glycerol. The value of V_s in dry rock though, is about that of water-saturated rock. Both compressional and shear wave velocities increase significantly with increasing viscosity. At relatively high viscosities of the fluid phase the velocities vary almost linearly with the logarithm of the viscosity. Hence they are more sensitive to viscosity at low values. Both velocities possess an inflection point near $\eta = 10^{-1}$ poise. The relative change of V_s with viscosity near the inflection point, as well as elsewhere, is much larger than the relative change in V_p. We attribute this experimental observation to the fact that the effective bulk modulus of saturated rock is independent of viscosity, as seen in fig. 3.3, whereas the effective shear modulus depends strongly on the viscosity.

The relative attenuation may be estimated from the variation (with viscosity) of the amplitude of the received signals. The amplitude of the input pulse was held roughly constant throughout each temperature run. Because too many parameters are involved it is not possible to determine the absolute magnitude of the input elastic pulse. From the runs on dry samples it appears though that the loss of power in the bond between the transducer and the rock is approximately independent of temperature and that the

transducers themselves radiated approximately the same signal in the temperature range of -77 to 100°C. The received amplitudes in the experiments with glycerol-saturated samples exhibited remarkable features. The compressional wave amplitudes were almost independent of viscosity whereas the shear wave amplitude A_s exhibited a pronounced minimum at about the same viscosity at which the inflection point in V_s occurred. Since both frequency and sample length remained practically unchanged throughout the experiment, the observed amplitudes can be converted into relative internal friction $\phi_{p,s} = -\ell n[A_{p,s}]$. The values shown in fig. 3.2 have been normalized, with ϕ of dry rock taken as unity. The attenuation of seismic shear energy has a sharp peak near $\eta = 10^{-1}$ poise. Values of ϕ for either dry or water saturated rock or for high viscosity glycerol are much smaller.

The calculated values of Young's modulus and Poisson's ratio are shown in fig. 3.3. Poisson's ratio decreases steadily with increasing viscosity, indicating that the effective shear modulus increases faster with viscosity than the bulk modulus. Young's modulus increases with viscosity almost like the effective shear modulus. The behavior resembles that of rocks saturated with water subject to increasing effective hydrostatic stress (Chapter 2). The phenomena are different, however: hydrostatic stress causes cracks to close whereas increasing fluid viscosity

essentially makes the fluid to behave increasingly like a solid.

4. Discussion of some theoretical aspects.

The increase of shear velocity by $\sim 22\%$ and compressional velocity by $\sim 7\%$ with the viscosity of the fluid phase in the Barre granite clearly demonstrates the importance of viscosity in solid aggregates with fluid-filled microcracks. The magnitude of the phenomena are especially surprising because they occur in rocks with crack porosity well below .01. Theoretical results by Walsh (16), previously verified by Nur (Chapter 2) explain the large changes observed in V_p upon saturation with water. Several investigators have considered the theoretical aspects of viscous inclusions. Biot (17) treated the problem of fluid in tubular and spherical inclusions. Formal solutions in which viscoelastic relations were assumed but in which no specific form was assigned to the viscous phases have been considered in some detail by Knopoff and MacDonald (18),and Collins and Lee (19). While these theories are useful mathematically they do not provide a particular physical mechanism of attenuation. Walsh (16) used solutions for the elastic response of aggregates to stress and the visco-elastic correspondence principle to obtain the viscous terms. As in the elastic solution the role of the inclusion shape is very important. Crack-like inclusions cause large changes in the response of a composite to stress even if porosity is small.

The bulk modulus of the fluid inclusion was shown previously (Chapter 2) to affect the bulk modulus of the aggregate. The present experimental results indicate that the effective shear modulus depends on the viscosity of the fluid phase. These observations are in remarkable agreement with Walsh's theoretical results which show that there exists a frequency at which the shear modulus has an inflection point and the internal friction a pronounced peak. This characteristic frequency ω_d is rather low and is related to the viscosity, and the intrinsic shear modulus, μ_0, by

$$\frac{\omega_d \eta}{a \mu_0} \approx 1 \tag{3.1}$$

where a is approximately equal to the average crack aspect ratio α. Furthermore Walsh's expressions indicate that internal friction and velocities are frequency dependent. In the neighborhood of ω_d he found that

$$\phi_s = \frac{A \omega / \omega_d}{B + (\omega / \omega_d)^2} \tag{3.2}$$

$$\bar{\mu} = \mu_0 \frac{1 + (\omega / \omega_d)^2}{B + (\omega / \omega_d)^2} \tag{3.3}$$

where A and B are constants that depend on the shape and density of pores and cracks. Our experimental data were obtained at a constant frequency ω while viscosity, and therefore ω_d, varied greatly. Walsh's work can be used

with our data to obtain other results. Combining equations 3.1, 3.2, and 3.3 gives

$$\phi_s \approx \frac{A\omega\eta/\alpha\mu_0}{B+(\omega\eta/\alpha\mu_0)^2}$$

3.4

and

$$\bar{\mu} \approx \mu_0 \frac{1+(\omega\eta/\alpha\mu_0)^2}{B+(\omega\eta/\alpha\mu_0)^2}$$

3.5

Note that frequency ω and viscosity η appear always as the product $\omega\eta$. The dependence of velocities and internal friction on viscosity, if Newtonian, can be used to evaluate their dependence on frequency at a constant viscosity--a relationship that is much more difficult to obtain experimentally.

Our results are similar to the results reported by Kê (20, 21) and McLean (22) on the effects of grain boundary viscosity in polycrystalline aluminum and brass. Kê found that polycrystalline aluminum and brass exhibit a temperature dependent internal friction ϕ and shear modulus $\bar{\mu}$ very much like those of viscoelastic material. A peak of internal friction was observed at some critical frequency ω_d at which an inflection point in the value of the effective shear modulus was also observed. This peak occurred at 290°C although aluminum melts at 660°C. With the assumption that the structural disorder at grain boundaries is associated with a viscosity, Kê showed that the critical frequency ω_d is related to viscosity η, the intrinsic shear modulus μ_0

and the ratio of the thickness of the viscous layer to grain diameter α by

$$\frac{\omega_d \eta}{\alpha \mu_o} = 1 \qquad\qquad 3.6$$

which has the form as equation 3.1. The expression for viscosity as a function of temperature for molten aluminum is approximately

$$\eta = \eta_o e^{K/T} \qquad\qquad 3.7$$

where η_o and K are constants and T is absolute temperature. Kê found that the viscosities he computed from equation 3.6 agreed with equation 3.7 extremely well. He concluded that grain boundaries in metals show a viscous behavior even several hundred degrees below the melting temperature. Further experiments at various frequencies by Kê (21) demonstrated that frequency and viscosity are indeed interchangeable. Because grain boundary creep rate varies linearily with stress it is relatively important at low stresses (23). Consequently this mechanism is likely to have significant effects on elastic wave propagation in polycrystalline aggregates.

In summary it is clear that shear modulus and internal friction in shear in a solid with inclusions of viscous fluids are very sensitive to both viscosity and frequency. At low concentrations of fluid with reasonably high bulk modulus the effective bulk modulus of the aggregate is al-

most identical to that of the solid itself and internal
friction associated with compressional waves is almost
independent of frequency.

5. Application to the earth.

Our results may be applied in two ways to the study of
the earth. They may be used to predict the effect of partial
melt, in rocks, on the elastic and anelastic properties.
Secondly, they may be used to infer the viscosity of the
fluid phase in the low velocity zone, abbreviated LVZ,
from seismic observation on the earth and with the plausible
assumption that the LVZ is caused by partial melting.

The relatively high attenuation (24), low viscosity
(25), and occurrence of zones of low velocity (26) in the
upper mantle are all compatible with the presence of small
amounts of a fluid phase. In order to apply our results
to the earth through equation 3.1, three of the four para-
meters must be known. The frequency ω and intrinsic shear
modulus μ_o are readily available from seismic investiga-
tions. The frequency is determined from the observed
waves while the shear modulus can be estimated from travel
times and phase velocities of surface waves (29). The
estimation of the viscosity of the fluid phase and the aspect
ratio α are less certain. The viscosity can be estimated
by thermodynamic considerations (27, 28) but the uncertainty
of both temperature and pressure effects on viscosity are
very large. Viscosity estimates from the responses of such

large regions as Fennoscandia to surface loads (25), are
irrelevant to the determination of the viscosity of the
fluid phase. Clearly, the viscosity of grain boundary zones
is much smaller than the apparent viscosity of the whole
aggregate.

Neither is the shape of the fluid phase in the earth
known. The available data for various metals indicate
the presence of a very narrow viscous zone, with an aspect
ratio $\alpha = 10^{-6}$ to 10^{-7} (20, 21). For Barre granite,
saturated with glycerol, α, computed from equation 3.1
(with $\omega_d = .5 \times 10^6 cps, \eta = .14 \text{ poise}, \mu_0 = 3.5 \times 10^{11} \text{cgs}$), equals
2×10^{-7}. These two values are remarkably close and in the
present discussion, they are <u>assumed</u> to be representative
of the upper mantle.

If rocks with viscous pockets respond to stress like
the glycerol saturated Barre granite, then

$$\left.\frac{\omega \eta}{\alpha \mu_0}\right|_{\text{laboratory}} \approx \left.\frac{\omega \eta}{\alpha \mu_0}\right|_{\text{mantle}} \qquad 3.8$$

and equations 3.2 to 3.5 are valid for parts of the earth.
Thus when frequency, viscosity of the fluid phase, and
the intrinsic shear modulus in the earth are known, the
velocities and internal friction can be estimated from the
Laboratory results. These results can be used to estimate
viscosities of the fluid phase from the seismic data.
Aki (29) postulated that a strong shear modulus anisotropy

exists beneath Japan in order to explain the observed Love
and Rayleigh Wave velocities. If this anisotropy is caused
by the presence of intergranular viscous material mostly
in the form of horizontal flat pockets, then the ratios R
of the effective shear modulus for Rayleigh waves to that
of Love waves at various depths are estimates of the ratio
of the effective shear modulus of mantle material with
melt to the intrinsic modulus. From Aki's model, R = .82
at a depth of about 25 km, and R = .75 at 60 km. These
values correspond to $\eta = 5 \times 10^8$ poise and $\eta = 3.5 \times 10^5$
poise respectively in the laboratory measurement. The
frequency of the surface waves was about .03 cps and the
intrinsic shear modulus of the mantle $\mu_o = 44 \times 10^{10}$ at 25 km
and $.72 \times 10^{10}$ dynes/cm^2 at 60 km. Thus from equation 3.6
the viscosity of the fluid phase 10^{16} poise at 25 km and
10^{13} poise at 60 km, a substantial decrease with depth.
This trend is compatible with the decrease of Q with depth
(30) over this depth range and the bulk viscosity computed
by McConnell (25).

The decrease of the calculated viscosity with depth
can be estimated from the temperature distribution in the
earth. The theoretical considerations of Gordon and Nelson
(31) lead to an approximate expression for grain boundary
viscosity in the earth.

$$\eta = \eta_o \exp\left[(K_1/T)(1 + K_2 P)\right] \qquad 3.9$$

where η_0, K_1 and K_2 are constants. At relatively shallow depth where $\partial T / \partial z$ is large, the temperature effect is dominant and viscosity is expected to decrease significantly with depth. At great depth, where $\partial T / \partial z$ is small the increase in pressure causes viscosity to increase. If the effect of pressure is neglected in the upper mantle, the viscosities under Japan compared with the measured values of viscosity as a function of temperature for glasses and volcanic rocks (32) correspond to a temperature of 450 to 600°C at 25 km and 500 to 670°C at 60 km. At the same depths, Clark and Ringwood's (33) temperature-depth relations give approximately 350 to 450°C and 600-700°C respectively. Improvements in the data on viscosity of silicate melts may lead in the future to improved estimates of temperature in the earth.

If the mechanism of the LVZ is that of grain boundary viscosity, then we may use our laboratory to infer certain features about the LVZ; viz. the dependence of attenuation and depth of the LVZ on frequency.

Consider first for simplicity a portion of an upper mantle in which the viscosity increases with depth according to the relation

$$\ln \left(\eta / \eta_0 \right) = K_1 Z + K_0 \qquad \text{3.10}$$

From the laboratory results, and assuming again that equations 3.1 to 3.5 hold, a region of rapid increase of velocities should be noticeable as shown in fig. 3.4.

Furthermore a low Q zone exists at a depth which depends on the frequency of the wave, for a given viscosity variation. At higher frequency the low Q and large dV/dz zones will seem shallower than at lower frequency.

Consider next the viscosity distribution that roughly corresponds to equation 3.9. Viscosity first decreases rapidly with depth and then increases at a smaller rate. The velocity and internal friction structure obtained from the laboratory data are shown in fig. 3.4 for various frequencies. For compressional waves the lowest velocity and the thickness of the LVZ are approximately independent of frequency. For shear waves however the shape of the LVZ and the lowest velocity depend significantly on frequency. At higher frequencies the shear velocity in the zone is higher and the LVZ thinner than at low frequencies. The apparent internal friction in shear has a single or a double peak depending on frequency. Velocities obtained by Archambeau et al. and Anderson and Smith (34) (fig. 3.5) show a larger decrease in V_s than in V_p because the effective bulk modulus remains almost constant through the LVZ while the effective shear modulus decreases by 15%. An upper bound on the viscosity of the melt can be obtained from the decrease of the shear modulus. If we take the intrinsic shear modulus $\mu_0 = .75 \, Mb$, $\bar{\mu}/\mu_0 = .80$ and $\omega = .1$ cps the viscosity of the fluid phase in the LVZ is $\eta \leqslant 10^{13}$ poise at a depth of 80-100 km. An independent estimate of

the lower bound of η can be obtained from equation 3.8 with the assumption that the LVZ is a region in which a maximum of attenuation exists. For $\omega = .1$ cps $\eta \geqslant 10^7$ poise. Although the difference between the two estimated bounds or viscosity is significant, the difference between the corresponding temperatures is only $100^{\circ}C$ to $200^{\circ}C$.

6. Conclusions.

Results from laboratory measurements of velocities and attenuation through rock saturated with viscous phase indicate that many of the observed seismic peculiarities in the upper mantle are compatible with the presence of partial melt or grain boundary viscosity. The structure of the low velocity zone with its pronounced decrease in shear velocity can be predicted from the laboratory data. Viscosities of the melt (10^{16} poise at 25 km, 10^{13} p. at 60 km and 10^7-10^{13} at 80 km) estimated from seismic data are compatible with the temperature expected at these depths.

The presence of partial melt causes seismic wave velocities, depth and thickness of the LVZ and internal friction to depend on the wave frequency. Longer period waves will be associated with more pronounced low velocity zones. Shorter period waves will be associated with less pronounced zones. Peaks of attenuation and locally large values of dV/dZ can occur in a region in which viscosity increases or decreases monotonously. The depth to this

region is frequency dependent.

The seismic equation of state becomes considerably more complicated with the introduction of terms to account for the presence of a liquid phase. Both V_p and V_s depend on frequency because the effective shear modulus is a function of frequency. To describe this dependence, viscosity and the configuration of liquid phase must be known in addition to the elastic constants of the solid phases and their densities.

References:

(1) King, M.S., Wave velocities in rocks as a function of changes in overburden pressure and pore fluid saturants, Geophysics, 31, 1, 50, 1966.

(2) Nur, Amos, The effect of fluid filled pores on seismic velocities of rocks, abstract, S.S.A. meeting, eastern section, 1968.

(3) Dortmann, N.B., and M.Sh. Magid, Velocity of elastic waves in crystalline rocks and its dependence on moisture content,(in English), Dok. Acad. Sci. USSR, earth sciences, 179, 1, 1968.

(4) Timur, A., Velocity of compressional waves in porous media at permafrost temperatures, Geophysics, 33(4), 584, 1968.

(5) Spetzler, H., and D.L. Anderson, The effect of temperature and partial melting on velocity and attenuation in a simple binary mixture, J. Geophy. Res., 73(18), 6051, 1968.

(6) Born, W.T., The attenuation constant of earth materials, Geophysics, 6, 132, 1941.

(7) Gordon, R.B., and L.A. Davis, Velocity and attenuation of seismic waves in imperfectly elastic rocks, J. Geophy. Res., 73(12), 3917, 1968.

(8) Garanin, V.A., On the dependence of the absorbing and velocity properties of two phase mediums on the viscosity of the pore filling (in Russian), Prikladnaya Geofizika 52, 83, 1968.

(9) Birch, F., The velocity of compressional waves in rocks to 10 kb. Part 2, J. Geophy. Res., 66, 2199, 1961.

(10) Simmons, Gene, Velocity of shear waves in rocks to 10 kilobars, 1, J. Geophy. Res., 69(6), 1123, 1964.

(11) Weast, R.C., Handbook of chemistry and physics, F-11 and F-35, The Chemical Rubber Co., Cleveland, Ohio, 1967.

(12) Volarovich, V., and K. Tolstoi, The simultaneous measurement of viscosity and electrical conductivity of some silicates at temperatures up to 1400°C, J. Soc. Glass Technol., 20, 54, 1936.

(13) Brace, W.F., A.S. Orange, and T.R. Madden, The effect of pressure on the electrical resistivity of water saturated crystalline rocks, J. Geophys. Res., 71, 3939, 1965.

(14) Brace, W.F., and A.S. Orange, Further studies of the effects of pressure on electrical resistivity of rocks, J. Geophy. Res., 73(16), 5407. 1968.

(15) Bland, D.R., The theory of linear viscoelasticity, Pergamon Press, 1960, p. 160.

(16) Walsh, J.B., A new analysis of attenuation in partially melted rocks, J. Geophy. Res., (in press), 1969.

(17) Biot, M.A., Theory of propagation of elastic waves in a fluid saturated porous solids I. Low frequency range, J. Accoust. Soc. Am., 28, 2, 1956.

(18) Knopoff, L., and G.J.F. MacDonald, Models for acoustic loss in solids, J. Geophys. Res., 65, 2191, 1960.

(19) Collins, F., and C.C. Lee, Seismic waves attenuation characteristics from pulse experiments, Geophysics, 21, 16, 1956.

(20) Ke, T.S., Stress relaxation across grain boundaries in metals, Phys. Rev., 72(1), 41, 1947.

(21) Ke, T.S., Experimental evidence of the viscous behavior of grain boundaries in metals, Phys. Rev., 71(8), 533, 1947.

(22) McLean, D., Grain boundaries in metals, Oxford University Press, London, 1957.

(23) McClintock, F.A., and Ali S. Argon, Mechanical behavior of materials, Ch. 19, p. 632, Addison-Wesley Publ. Co., Reading, Mass., 1966.

(24) Kanamori, H., Attenuation of P waves in the upper and lower mantle, Bull. Earthq. Res. Inst., 45, 299, 1967.

(25) McConnell, R.K., Jr., Isostatic adjustment in a layered earth, 70(20), 5171, 1965.

(26) Johnson, L.R., Array measurements of P velocities in the upper mantle, J. Geophy. Res., 72, 6309, 1967.

(27) Gordon, R.B., Diffusion creep in the earth's mantle, J. Geophy. Res., 70, 2413, 1965.

(28) McKenzie, D.P., The viscosity of the mantle, Geophy. J., 14, 297, 1967.

(29) Aki, K., Seismological evidence for the existence of soft thin layers in the upper mantle under Japan, J. Geophy. Res., 73(2), 585, 1968.

(30) Tsai, Y.B., and K. Aki, Simultaneous determinations of the seismic moment and attenuation of seismic surface waves, Bull. Seism. Soc. Am., 59(1), 275, 1969.

(31) Gordon, R.B., and C.W. Nelson, Anelastic properties of the earth, Rev. Geophys., 4(4), 457, 1966.

(32) Clark, S.P., Jr., Viscosity in 'Handbook of physical constants', Geol. Soc. Amer. Mem. 97, p. 297, 299, 1966.

(33) Clark, S.P., Jr., and A.E. Ringwood, Density distribution and constitution of the mantle, Rev. Geophys., 2, 35, 1964.

(34) Anderson, D.L., and C. Sammis, The low velocity zone, J. Geophy. Res. (in press), 1969.

Table 3.1

Physical Properties of Barre granite

Property			Remarks
Density		2.650 gm/cm^3	
Porosity	crack	.003$\pm$.0005	
	pore	.003$\pm$.002	
	total	.006$\pm$.001	
Velocity			
at room conditions			
V_p(dry)		3.90 km/s	
V_p(saturated)		5.45 km/s	
V_s(dry)		2.58 km/s	
V_s(saturated)		2.63 km/s	
at 10 kilobars			
V_p		6.40	Different sample. Birch (1960)
V_s		3.70	Simmons (1964)
Average grain size		3 mm	
Modal analysis (% volume)			Birch (1960)
Qz		26%	
K-Felspar(orthoclase)		25%	
Plagioclase(albite)		37%	
Mica-Biotite		9%	
-Muscovite		3%	

Table 3.2

Physical parameters of saturated Barre granite sample at various temperatures.

Fluid	Temperature	Viscosity $\log(\eta/\eta_0)$	V_p km/s	V_s km/s	$\tilde{\mu}$	$\bar{K}$	$\bar{E}$	ν	$\bar{\mu}/\mu_0$
Air	18	-4	(4.000)	2.580	17.57	(18.82)	(40.20)	.144	.531
Water	18	-2	5.080	2.630	18.26	43.78	48.10	.317	.545
Glycerol	158[2]	-1.6	5.081	2.643	18.44	43.56	48.49	.315	.550
	124[2]	-1.2	5.085	2.666	18.76	43.24	49.18	.310	.560
	98	-.8	5.095	2.700	19.24	42.87	50.23	.305	.574
	74	-.4	5.117	2.753	20.00	42.44	51.84	.296	.597
	56	0.0	5.148	2.800	20.69	42.36	53.40	.290	.618
	40	.5	5.190	2.838	21.26	42.76	54.72	.287	.635
	25	1.0	5.213	2.870	21.74	42.74	55.80	.283	.649
	11	1.5	5.230	2.900	22.20	42.60	56.76	.278	.663
	1	2.0	5.250	2.927	22.61	42.60	57.63	.274	.675
	- 8	2.5	5.260	2.950	22.97	42.41	58.39	.271	.686
	- 18	3.0	5.275	2.971	23.30	42.39	59.10	.268	.695
	- 25	3.5	5.290	2.992	23.63	42.36	59.79	.265	.705
	- 32	4.0	5.308	3.014	23.98	42.40	60.53	.262	.716
	- 43	5.0	5.340	3.061	24.73	42.30	62.09	.255	.738
	- 55	6.0[2]	5.370	3.107	25.48	42.22	63.59	.248	.761
	- 63	7.0[2]	5.402	3.145	26.11	42.22	64.97	.244	.779
	- 71	8.0[2]	5.435	3.190	26.86	42.16	66.47	.237	.802
	- 78	9.0	5.470	3.238	27.68	42.08	68.11	.230	.826
Solid	--	--	6.00	3.54	33.05	47.52	82.63	.220	1.000

1 Viscosity is given in $\log(\eta/\eta_0)$ where $\eta_0 = 1$ poise.
2 Extrapolated from measured data.

75.

Figure Captions

fig. 3.1   Viscosity of glycerol (after Weast[11]). The
glycerol was used as fluid inclusion in rock.

fig. 3.2   Effects of viscosity of a fluid phase on velocity
and attenuation of elastic waves. Both V_p and
V_s increase with viscosity, particularly at
$\eta \approx .1$ to 1 poise where internal friction is
particularly high.

fig. 3.3   Effective isotropic elastic constants cal-
culated from the velocities. Shear and
Young's moduli increase and Poisson's ratio
decrease with increasing viscosity. Bulk
modulus is almost constant.

fig. 3.4   Relations between viscosity distribution and
velocities and internal friction. Viscosity
increases linearily on a log scale with depth
(upper figure) or has a minimum (lower figure).

fig. 3.5   Upper mantle velocity structure (after Ander-
son and Sammis[34]). The low velocity zone
is more pronounced for shear than compressional
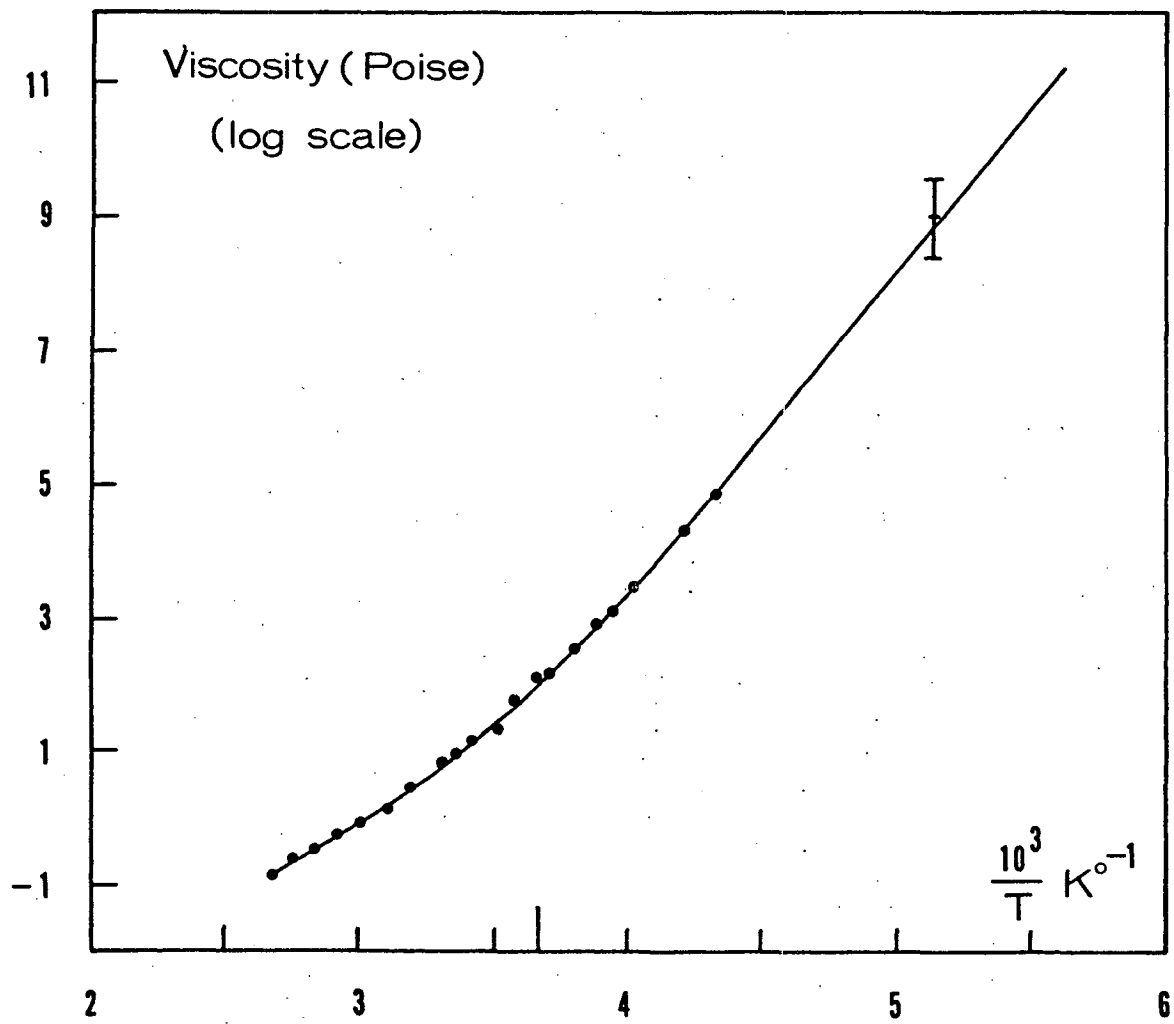waves, consistant with the presence of viscous
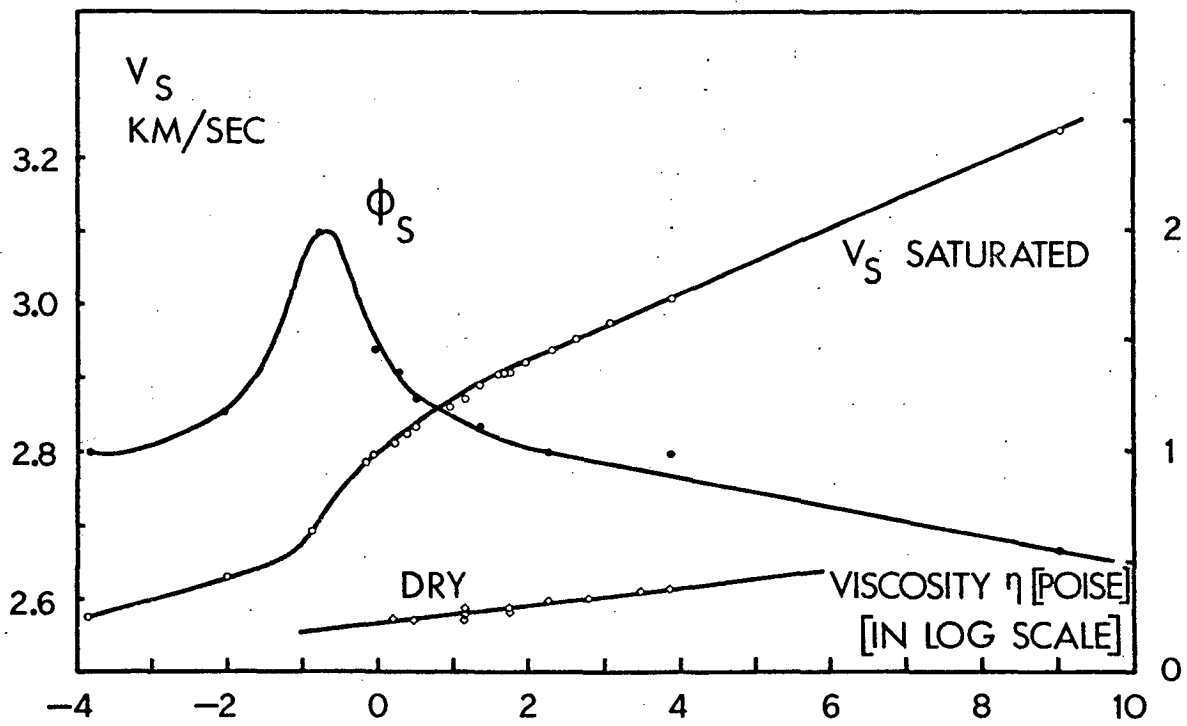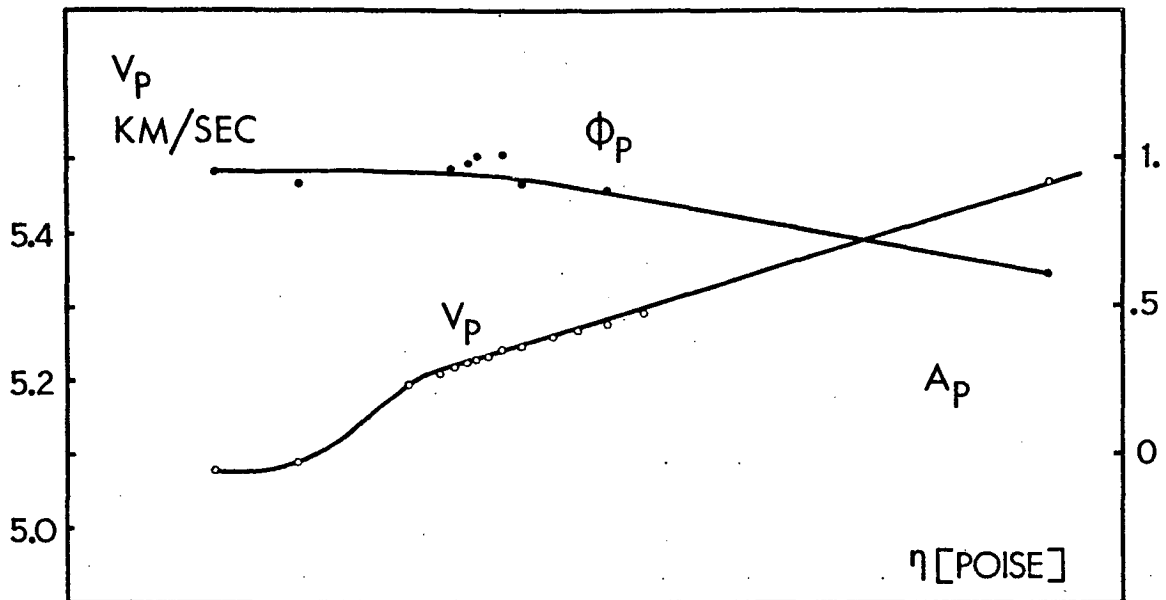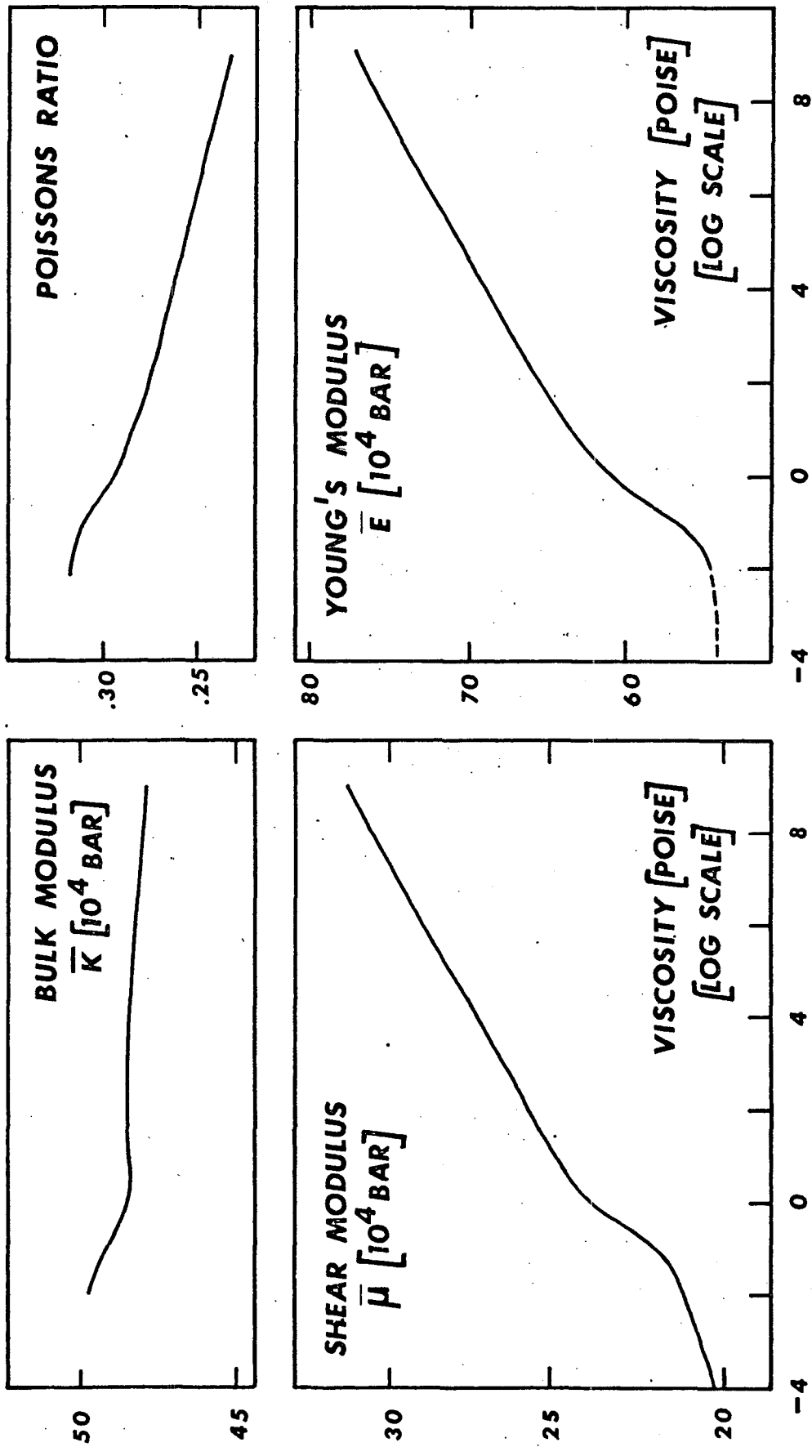pockets.

Fig 3.1

FIG 3.2

POISSONS RATIO

.30
.25

BULK MODULUS
$\overline{K}$ [10^4 BAR]

50
45

YOUNG'S MODULUS
$\overline{E}$ [10^4 BAR]

80
70
60

VISCOSITY [POISE]
[LOG SCALE]

-4   0   4   8

SHEAR MODULUS
$\overline{\mu}$ [10^4 BAR]

30
25
20

VISCOSITY [POISE]
[LOG SCALE]

-4   0   4   8

FIG 3.3

fig 3.4

Left panel labels (top to bottom): VISCOSITY η log scale, V_p, high ω, V_s, low ω, high ω, φ, low ω, DEPTH

Right panel labels (top to bottom): VISCOSITY η log scale, V_p, high ω, low ω, V_s, high ω, low ω, φ, DEPTH

KM / SEC

4   5   8   9   10

0

.33 V_s .18 V_p

ANDERSON   ARCHAMBEAU

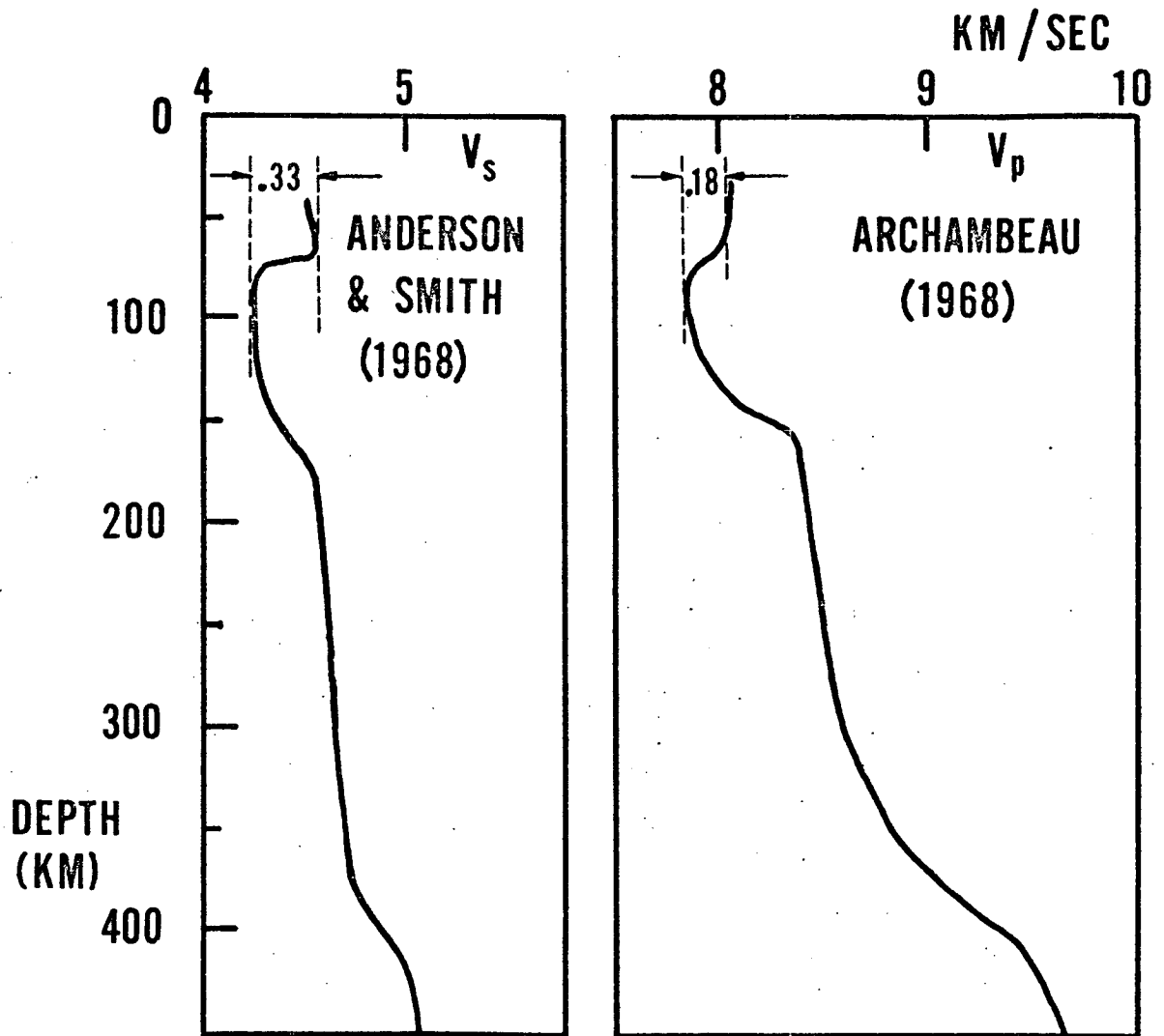& SMITH   (1968)

(1968)

100

200

300

DEPTH
(KM)

400

FIG 3.5

Chapter 4

Stress induced velocity anisotropy in rock:

an experimental study

1. Introduction

The fact that uniaxial stress causes larger changes of elastic properties in certain rocks in the direction of the applied stress which are larger than the changes in the perpendicular direction was demonstrated by Tocher (1957). This behavior seems clearly to be associated with the microcracks that exist in granitic rocks, a suggestion made long ago by Zisman (1933) to explain the effect of hydrostatic stress on elastic properties of rock. At effective[*] stress levels up to about 1 kb, the elastic properties of some rocks are controlled mainly by the properties of the microcracks. Such rocks include granites, schists, monzonites, quartz diorites, and in general, those igneous rocks that contain quartz. The effect of non hydrostatic stress on elastic wave velocities, which we report here, are possibly important for seismic crustal studies, in situ stress determinations and perhaps also for the interpretation of velocity anisotropy of the low velocity zone.

In rocks, crack shapes are approximated reasonably

---

* Effective stress is defined as the confining pressure minus the pore pressure.

well by penny shaped ellipsoids (Walsh 1965), which allows
one to describe the effects of cracks with only three para-
meters--the crack aspect ratio (width to length), the
porosity, and the distribution in space of the crack nor-
mals.

The effect of an applied non-hydrostatic stress is
to close cracks in some directions and leave cracks open
in other directions. The stress necessary to close a
penny shaped crack is proportional to its aspect ratio
(Walsh 1965)--the narrower cracks close at lower pressure.
The effective elastic constants of a solid with cracks are
determined by the distribution of orientations of open
cracks (Walsh 1965). If cracks are closed in some directions
but open in others, rocks that are intrinsically isotropic
show a directional dependence of the effective elastic con-
stants and are in general anisotropic. The elastic proper-
ties of a rock, which initially has a random crack distri-
bution, could possibly remain isotropic under hydrostatic
pressure, attain hexagonal symmetry under uniaxial stress,
and orthorhombic symmetry under three different principal
stresses.

In order to investigate the effects of non hydrostatic
stresses on the elastic properties of rocks, we have
measured the velocities of elastic waves in several directions
on the Barre and Westerly granites. These materials have
been used in laboratory studies by others (Table 4.1).

2. Experimental procedure

A cylinder 10 cm in diameter and 10 cm long of Barre granite, carefully machined on a cylindrical grinder to fit closely the corresponding hemi-cylindrical holes in two steel blocks was loaded uniaxially in a simple press. At zero stress the velocities of compressional waves in the Barre sample were 3.79, 3.90, and 3.93 km/s in three mutually perpendicular directions. The axis of the cylinder was along the 3.90 km/s direction and transducers were mounted along the 3.79 km/s direction for velocity measurements across the cylinder. The geometry and certain conventions used later are shown in fig. 4.1. Because the validity of our results depend on having a uniaxial stress and because such factors as elastic mismatch between the steel blocks and the rock cylinder, non-uniformity of the rock, and the small holes cut in side of cylinder for transducers could lead to non-uniaxial stress, we checked the state of stress in the sample with strain gages mounted on the flat ends of the cylinder. If it is truly uniaxial the strain in direction θ would be

$$\epsilon(\theta) = \frac{1+\nu}{E}\,\sigma\cos^2\theta - \frac{\nu}{E}\,\sigma \qquad\qquad 2.1$$

The results of measuring ϵ as a function of direction, shown in fig. 4.2, show that terms of higher order than $\cos^2\theta$ are less than 10%.

Instrumentation was similar to that used by Birch

(1961) and Simmons (1964) and identical to that used by us
(Appendix A) for previous work on the elastic properties of
rocks. Transducers (barium titanate for P-waves and AC-
cut quartz for S-waves) were cemented with a conductive
epoxy to the rock surface in each of two slots cut on
opposite sides of the rock cylinder, at the center of its
length. A Velonex model 350 pulse generator was used to
obtain a 0.1 pulse of 50 to 500 volts. Time delays were
measured with a variable length mercury delay line, similar
to that described by Birch (1960).

3. Results of measurements

Four sets of measurements were made: (1) Compressional
waves normal to axis, (2) shear waves propagating normal to
axis and polarized normal to axis, (3) shear waves propagat-
ing normal to axis and polarized parallel to axis, and (4)
shear waves propagating parallel to axis. Each set con-
sists of velocity as a function of uniaxial stress and as
a function of the angle Θ (fig. 4.1). All wave velocities
in this experiment were obtained after the sample was
dried and allowed to come to equilibrium with room conditions.
The data are given in Tables 4.2 through 4.5 and shown in
figures 4.3 through 4.8.

Although velocity increases in all directions with
increasing uniaxial stress, the size of the increase clearly
depends on the angle between the stress and the propagation
direction of the compressional wave. For shear waves, it

depends on the direction of polarization as well as on the direction of propagation. The largest effect on velocity is observed when the wave propagates in the direction of the applied stress and the smallest in a direction perpendicular to it (figs. 4.3, 4.4). In addition, the velocity of the shear wave polarized parallel with the axis of the cylinder exhibits large dependence on direction (fig. 4.6) whereas that of the wave polarized normal to the axis appears to be (almost) independent of direction (fig. 4.8). These are the relations that would exist for single crystal elasticity.

The interesting phenomenon of acoustic double refraction was observed for shear waves propagating along the axis of the cylinder (figs. 4.9 and 4.10). Although the phenomenon has been observed previously in single crystals (Waterman and Teutonico, 1957 and Simmons and Birch 1963), we believe this is the first time it has been observed in rocks in the laboratory. The observed arrival wave forms for the shear wave propagating parallel to the axis as a function of direction Θ, and at 400 bars, are displayed in fig. 4.9. The amplitude of the input signal was roughly the same for all angles. At $\Theta = 70°$, the arrival of two waves at different times is clearly seen. These arrivals may be traced to both larger and smaller values of Θ although the second arrival is difficult to pick at values less than $30°$ and the first arrival is

obscure at this amplification at values greater than $70°$. The velocity of the fast wave seen at $0° \leqslant \theta \leqslant 70°$ in fig. 4.4 is independent of θ whereas the velocity of the slow wave ($\theta \geqslant 70°$) varies with direction (Table 4.5). The apparent changes in wave forms with increasing stress, particularly for $\theta = 60°$ and $70°$ (fig. 4.10) are due to inter- ference between the two shear waves. As indicated in fig.4.10, the amplitudes of the two waves that travel along the axis are equal at about $\theta = 50°$ to $60°$ degrees. This could indicate that dissipation becomes anisotropic with stress--the dissipation of energy of the fast wave is smaller than the slow wave.

4.   Discussion of uniaxial results

The results show clearly that the Barre granite be- comes anisotropic under uniaxial stress condition. Both shear and compressional velocities change with direction, at a given stress level, in a manner expected from the elasticity of single crystals. In general, distinct shear waves with different velocities exist in any direction of propagation when uniaxial stress is applied; one direction of polarization is always in the plane which also includes the direction of the applied stress and the second direction of polarization is in an orthogonal plane. It is especially gratifying that at all stress levels the velocity of shear waves propagating along the cylinder axis and polarized parallel to the stress axis is equal within $\pm 1\%$ to the

velocity of shear waves propagating parallel to the stress axis and polarized perpendicular to the cylinder axis; similar statements could be made for other pairs of directions. We interpreted these results to indicate that the influence of stress on velocity in general can be described in terms of the anisotropy elements of an elastic crystal.

If we restrict our discussion to materials in which the change of velocity with stress is not too large and for waves of sufficiently small stress amplitudes, in order to avoid the effects of non-linear stress-strain behavior, then we may estimate the limits of both the effect of stress on the elastic constants and the effect of the stress amplitude of the wave. In one dimension we have

$$\epsilon = \frac{1}{E}\sigma \qquad\qquad 4.1$$

where ϵ is strain, σ is the corresponding stress and E is an elastic parameter.

Differentiating with respect to σ yields

$$\frac{d\epsilon}{d\sigma} = \frac{1}{E}\left(1 - \frac{\sigma}{E}\cdot\frac{dE}{d\sigma}\right) \qquad\qquad 4.2$$

Linear elasticity can describe the material adequately when $\frac{\sigma}{E}\cdot\frac{dE}{d\sigma} \ll 1$.

Our measurements indicate that Young's modulus E can change by as much as 10% per 100 bars. If $E = 10^6$ bars then $dE/d\sigma \approx 10^3$. Therefore, the dynamic stress level in the rock should not exceed a few bars for satisfactory

linear approximation. Because the maximum stress amplitude
of the waves is .01 bar or less, the effect of stress waves
on the dynamic stress-induced anisotropy is negligible.

The uniaxial stress field has a high degree of symmetry,
that of the hexagonal system. If the initial crack dis-
tribution were isotropic, no lower symmetry in the elastic
properties would be anticipated although a higher one could
be possible. If however the initial crack distribution was
not random the induced anisotropy may have a form less
symmetrical than hexagonal. Indeed the variation of the
velocity of SV with direction with more than one extreme
point is not compatible with hexagonal symmetry. Because
this variation is small, we assume that hexagonal symmetry
describes the stressed rock and proceed to compute the
various effective dynamic elastic constants as a function of
the applied uniaxial stress. The transformation of velocities
to elastic constants is available in several references
(Stoneley 1948; Hearmon 1961 for example). For convenience
of notation, we take the 3-axis parallel to the direction
of the applied stress, the 2-axis parallel to the cylinder
axis, and the 1-stress orthogonal to the 1 and 2 axes. The
values of E_{33}, E_{11}, μ_{13} and μ_{12} are given in Table 4.6 and
are shown in figure 4.11. We notice that much like the
results in chapter 2 at very low stress levels the values
of Poisson's ratio are small and increase slowly with stress.
The Young's moduli (fig. 4.11a) and the shear moduli

(fig. 4.11b) also increase with increasing stress, as a strong function of direction. Noteworthy is the observation that the influence of stress as well as direction on the Young's moduli E's is greater than on the shear moduli.

5. Biaxial loading

In order to extend our observations to a biaxial state of stress, we measured compressional velocities on 13 cm cubes of Westerly and Barre granite loaded in a stress system that consisted of two uniaxial presses mounted at 90° to each other. Equal velocity contours on a σ_1, σ_2 plane are shown in fig. 4.12. These lines indicate the range of biaxial stress combinations which will produce a given velocity. We conclude from these results that the velocity is not uniquely related to stress because various biaxial stress combinations can produce the same velocity in a given direction.

6. Conclusions

Application of non-hydrostatic stress to a rock that contains micro-cracks induces elastic anisotropy. The stressed rock exhibits many features of anisotropic crystals, including that of acoustic double refraction.

References:

Birch, Francis, The velocity of compressional waves in rocks to 10 kilobars, part 1, J. Geophy. Res., 65, 1083, 1960; part 2, 2199, 1961.

Hearman, R.F.S., An introduction to applied anisotropic elasticity, Oxford University Press, ch. 6, New York, 1961.

Simmons, Gene, Velocity of shear waves in rocks to 10 kilobars, 1, J. Geophy. Res., 69(6), 1123, 1964.

Simmons, Gene, and Francis Birch, Elastic constants of Pyrite, J. Appl. Phys., 34(9), 2736, 1963.

Stoneley, R., The seismological implications of aeolotropy in continental structure, Monthly Notices, Roy. Astron. Soc., Geophy. Suppl., 5, 343, 1949.

Tocher, D., Anisotropy in rocks under simple compressions, Trans. Am. Geophys. Union, 31(1), 89, 1957.

Walsh, J.B., The effect of cracks on the compressibility of rock, J. Geophy. Res., 70(2), 381, 1965.

Waterman, P.C., and L.H. Teutonico, Ultrasonic double refraction in single crystals, J. Appl. Phys., 28, 266, 1957.

Zisman, W.A., Comparison of the statically and seismologically determined elastic constants of rocks, Proc. Nat. Acad. Science, 19(7), 653, 1933.

Table 4.1

Physical Properties of Barre Granite

Property		Remarks
Density	2.650 gm/cm^3	
Porosity crack	.003$\pm$.0005	
pore	.003$\pm$.002	
total	.006$\pm$.001	
Velocity		
at room conditions		
V_p(dry)	3.90 km/s	
V_p(saturated)	5.45 km/s	
V_s(dry)	2.58 km/s	
V_s(saturated)	2.63 km/s	
at 10 kilobars		
V_p	6.40	Different sample. Birch (1960)
V_s	3.70	Simmons (1964)
Average grain size	3 mm	
Modal analysis (% volume)		
Qz	26%	
K-Felspar(orthoclase)	25%	
Plagioclase(albite)	37%	
Mica-Biotite	9%	
-Muscovite	3%	

Table 4.2

Compressional wave velocity (km/sec) in Barre granite as a function of magnitude and direction of uniaxial stress

stress bars	Angle between stress and dir. of propagation									
	0°	10°	20°	30°	40°	50°	60°	70°	80°	90°
0	3.79	3.82	3.79	3.79	3.78	3.79	3.79	3.79	3.79	3.79
25	3.94	3.94	3.90	3.89	3.88	3.86	3.83	3.81	--	--
50	4.04	4.03	4.03	3.99	3.95	3.92	3.86	--	--	--
75	4.13	4.15	4.10	4.07	4.06	3.98	3.90	--	--	--
100	4.22	4.22	4.22	4.15	4.12	4.04	3.95	3.89	3.84	3.85
150	4.37	4.41	4.37	4.30	4.26	4.15	4.05	--	--	
200	4.51	4.53	4.51	4.42	4.36	4.28	4.15	4.05	3.93	3.92
250	4.60	4.61	4.58	4.52	4.46	4.34	4.23	--	--	--
300	4.67	4.68	4.65	4.59	4.54	4.40	4.30	4.19	4.04	4.02
350	4.73	--	--	--	--	--	--	--	--	4.05
400	4.78	--	--	--	--	--	--	--	--	4/08

Table 4.3

Shear Wave Velocity (SH) in Barre granite as a function of magnitude and direction of uniaxial stress. Velocity in KM/SEC.

Stress Bar	Angle between stress and direction of propagation									
	0°	10°	20°	30°	40°	50°	60°	70°	80°	90°
0.	2.63	2.63	2.63	2.63	2.63	2.63	2.63	2.62	2.62	2.63
50.	2.69	2.70	2.70	2.69	2.69	2.67	2.65	2.65	2.64	2.65
100.	2.74	2.78	2.78	2.77	2.76	2.73	2.70	2.68	2.67	2.68
150.	2.83	2.84	2.84	2.83	2.81	2.78	2.75	2.73	2.71	2.71
200.	2.88	2.89	2.89	2.87	2.86	2.83	2.79	2.77	2.74	2.74
250.	2.92	2.93	2.93	2.92	2.90	2.87	2.83	2.80	2.77	2.77
300.	2.96	2.96	2.97	2.95	2.93	2.89	2.85	2.82	2.79	2.79
350.	2.99	3.00	2.99	2.98	2.96	2.93	2.87	2.85	2.82	2.82
400.	3.03	3.03	3.03	3.01	2.99	2.95	2.90	2.87	2.84	2.84

Table 4.4

Shear Wave Velocity (SV) in Barre granite as
a function of magnitude and direction of uniaxial stress.
Velocity in KM/SEC.

Pressure Bar	Angle between applied stress and direction of propagation									
	$0°$	$10°$	$20°$	$30°$	$40°$	$50°$	$60°$	$70°$	$80°$	$90°$
0.	2.61	2.63	2.64	2.63	2.64	2.63	2.64	2.63	2.63	2.63
50.	2.68	2.69	2.70	2.70	2.70	2.69	2.68	2.67	2.66	2.66
100.	2.76	2.77	2.77	2.76	2.77	2.75	2.74	2.73	2.73	2.73
150.	2.83	2.84	2.84	2.83	2.83	2.82	2.81	2.79	2.79	2.80
200.	2.89	2.90	2.89	2.89	2.89	2.88	2.86	2.86	2.86	2.87
250.	2.95	2.96	2.95	2.94	2.94	2.93	2.91	2.91	2.91	2.92
300.	2.99	3.00	2.99	2.91	2.98	2.97	2.95	2.95	2.96	2.96
350.	3.04	3.05	3.04	3.03	3.02	3.00	2.99	3.00	3.00	3.00
400.	3.07	3.08	3.08	3.07	3.05	3.04	3.02	3.02	3.03	3.04

Table 4.5

Shear wave velocities (km/sec) in the direction perpendicular to that of the applied stress as a function of stress and direction of polarization of the transducers. The measured velocity is for polarization in the plane of the stress for $0° < \theta < 70°$ and perpendicular to stress for $\theta > 70°$ (see fig. 4.10b).

stress bars	Angle between direction of stress and plane of transducers' polarization									
	0°	10°	20°	30°	40°	50°	60°	70°	80°	90°
0	2.65	2.65	2.65	2.64	2.64	2.64	2.63	2.63	2.63	2.63
50	2.73	2.72	2.72	2.70	--	--	--	2.65	2.65	2.66
100	2.79	2.78	2.77	2.78	2.78	2.77	--	2.67	2.67	2.69
150	2.85	2.84	2.84	2.84	2.84	2.84	--	2.70	2.70	2.72
200	2.90	2.91	2.90	2.90	2.90	2.88	--	2.72	2.73	2.75
250	2.93	2.93	2.93	2.94	2.94	2.93	--	2.74	2.75	2.78
300	2.98	2.98	2.98	2.98	2.98	2.97	2.97	2.76	2.77	2.80
350	3.00	3.00	3.00	3.00	3.00	3.00	3.00	2.78	2.79	2.82
400	3.02	3.02	3.02	3.02	3.02	3.02	3.02	2.80	2.81	2.83

Table 4.6

Various effective elastic constants (in b) in Barre granite
as a function of uniaxial stress (in bars).

Stress	E_{11}	E_{33}	μ_{12}	μ_{13}	ν_{13}	ν_{31}	ν_{12}
0	.367	.367	.183	.183	.036	.036	.036
50	.370	.407	.187	.191	.060	.067	.037
100	.378	.436	.190	.198	.073	.086	.045
150	.388	.475	.194	.212	.067	.082	.064
200	.396	.502	.198	.219	.070	.088	.064
250	.412	.517	.203	.225	.070	.093	.070
300	.420	.536	.205	.231	.072	.092	.084
350	.425	.547	.210	.236	.071	.091	.079
400	.436	.562	.213	.242	.070	.085	.086

Figure Captions:

Fig. 4.1   Geometrical relations. The cylindrical rock sample
            is subjected to an applied uniaxial stress.
            Velocities of elastic waves are measured either
            along a diameter or along the axis of the
            cylinder. The sample, with the transducers
            attached, is rotated with respect to the applied
            stress so that the wave always travels through
            exactly the same path in the rock, while only
            the relative direction of stress σ is being
            changed. Directions of polarization of the
            shear transducers are indicated by SV and SH.

Fig. 4.2   Strain as a function of stress levels and
            direction θ . Strain gages were mounted on
            the ends of the cylinder in order to test the
            assumption of a uniaxial stress throughout
            the sample. Agreement with theoretical curve,
            dashed line, is better than 10%.

Fig. 4.3   Compressional wave velocity as a function of
            and stress direction of propagation. At $\sigma =$
            300 bars the velocity in the stress direction
            increased by about 20% while at the perpendicu-
            lar direction the increase is only about 5%.

Fig. 4.4   Dependence of the compressional velocity on
            direction at a given stress level. The

dependence on direction has similar form at all stress levels.

Fig. 4.5   The velocity of the shear wave SH. SH is polarized in the plane that includes the direction of stress when $\theta = 0°$ and is perpendicular to stress when $\theta = 90°$. Velocity depends both on direction and magnitude of applied stress.

Fig. 4.6   SH velocity dependence on direction. The dependence is similar to that of P-velocity although the relative difference between the velocities normal and perpendicular to stress are smaller.

Fig. 4.7   Velocity of the SV wave as a function of stress. The velocity is almost identical in all directions, unlike the SH velocity. The plane of polarization always includes the direction of the applied stress.

Fig. 4.8   Variation of SV wave velocity with direction. The direction of the uniaxial stress is in the plane of polarization at all values of θ.

Fig. 4.9   Observed received wave form travelling along the axis of the cylinder at 400 bar at various angles θ between the direction of applied stress and direction of polarization of the transducers.

At $\theta = 70°$ the fast wave is polarized in the plane that includes the direction of the applied stress.

Fig. 4.10   The shape of the received shear wave form which travelled along the cylinder's axis perpendicular to the applied stress. (a) $\theta = 60°$. The amplitude first decreases with increasing stress, due to interference, then increases again. (b) $\theta = 70°$. The amplitude of the fast wave is greatly reduced and the SV and SH phases can be identified.

Fig. 4.11   Effective elastic constants. The constants describe the induced velocity anisotropy: (a) Young's moduli (b) Shear moduli, in directions parallel and perpendicular to the applied stress.

Fig. 4.12   Velocity in a state of biaxial stress. The same velocity, in a given direction in Barre granite is observed for many stress combinations. Combinations of two stresses which given the same compressional wave velocity (solid line) are presented in this equal velocity diagram.
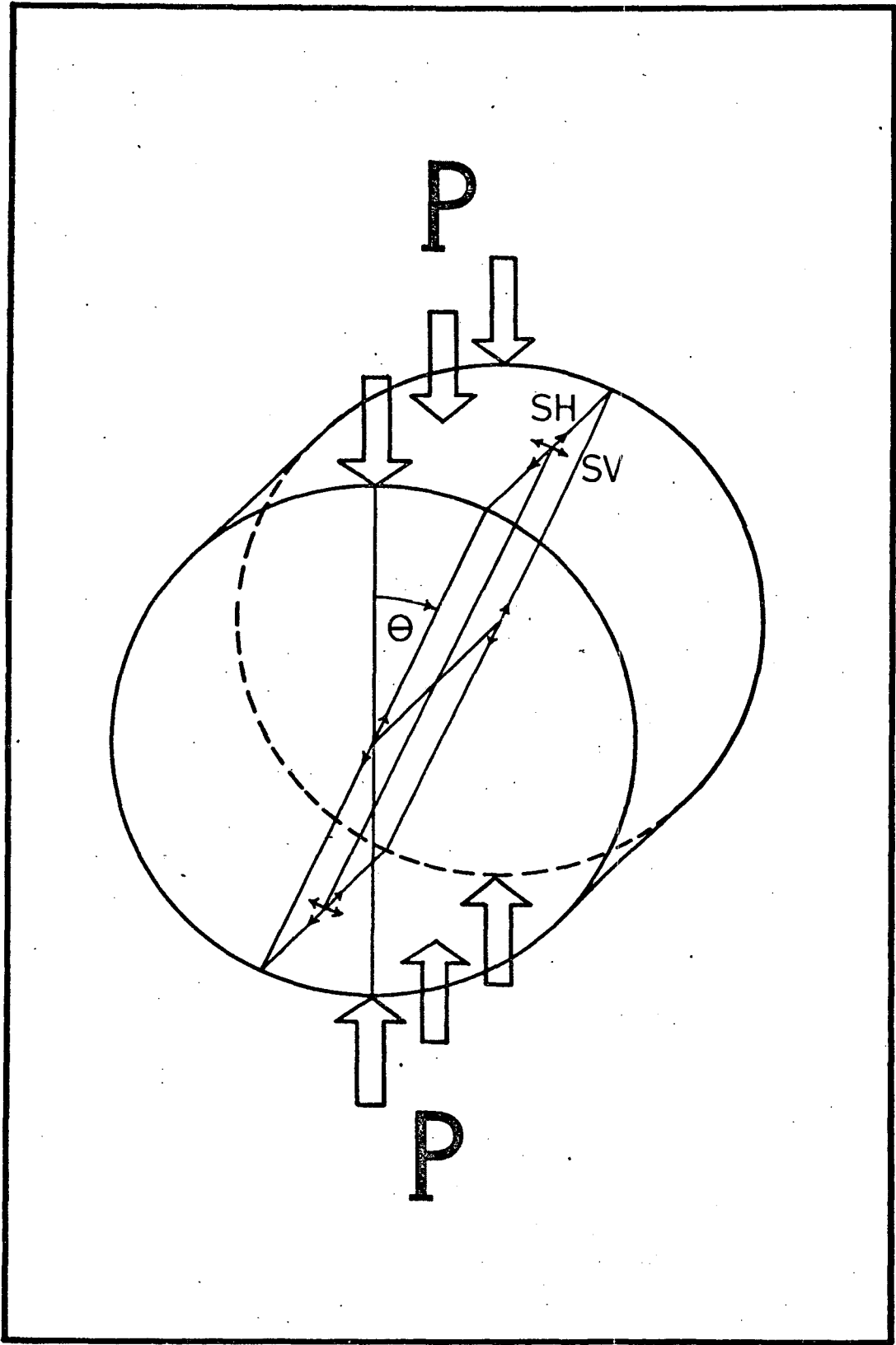
FIG 4.1
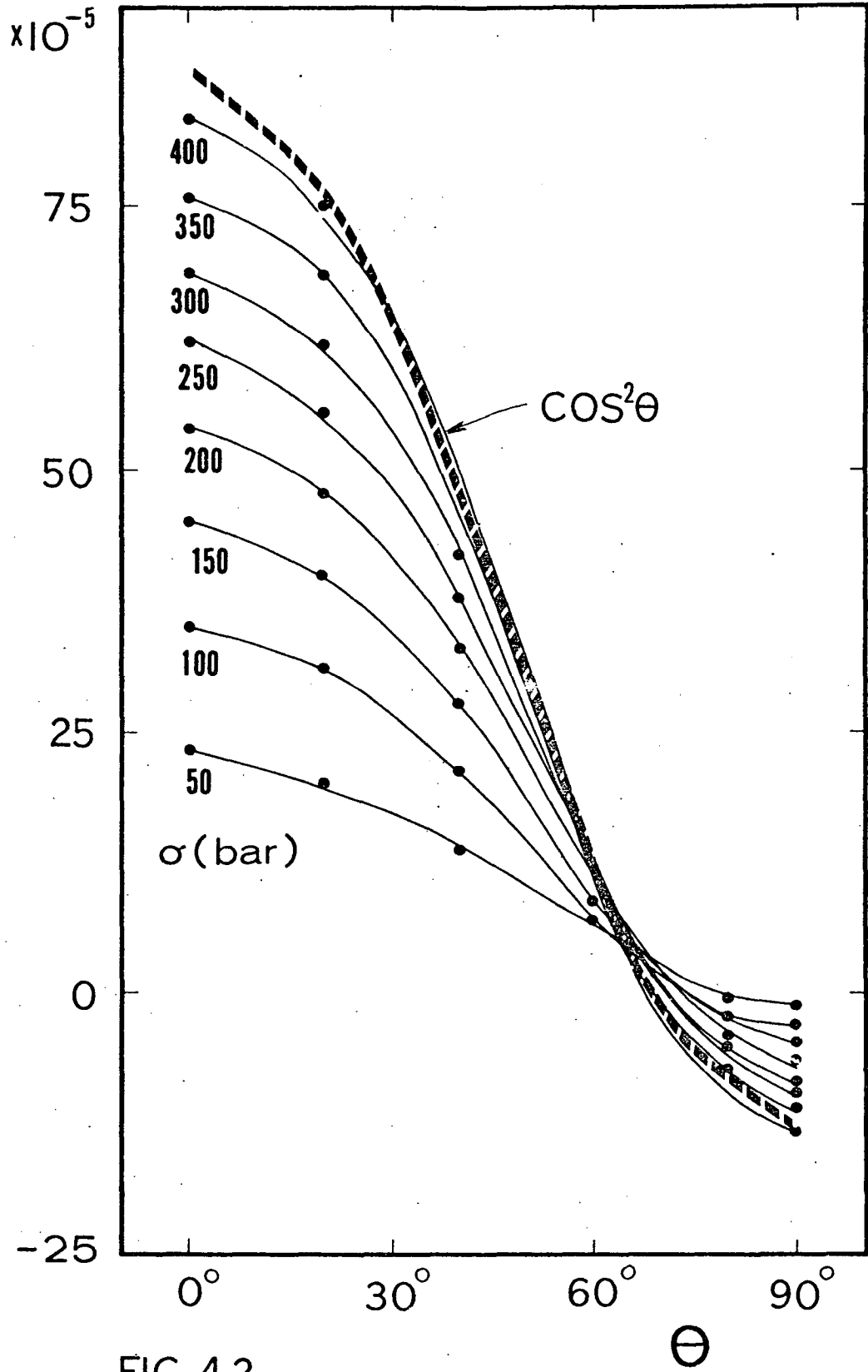
FIG. 4.2
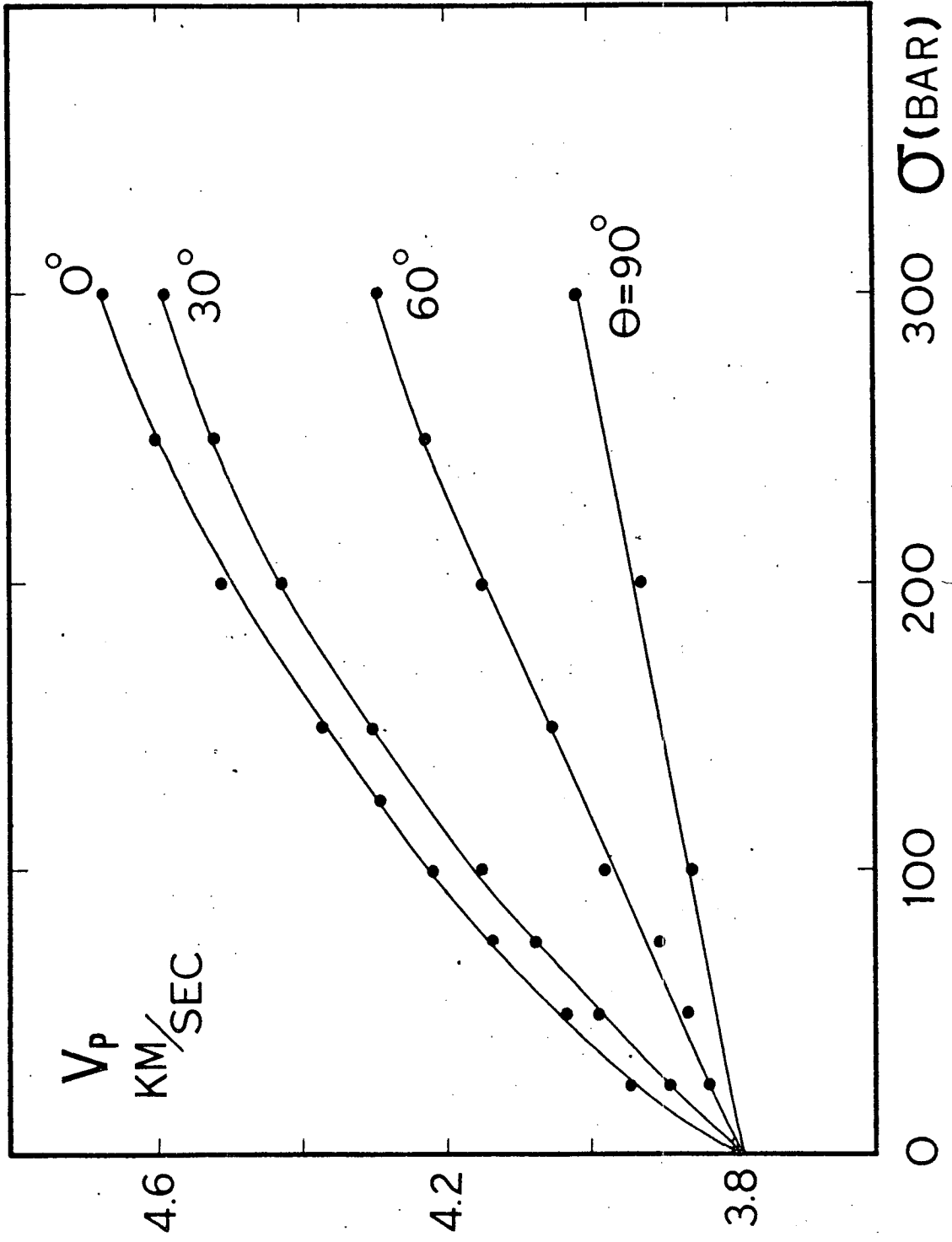
FIG 4.3
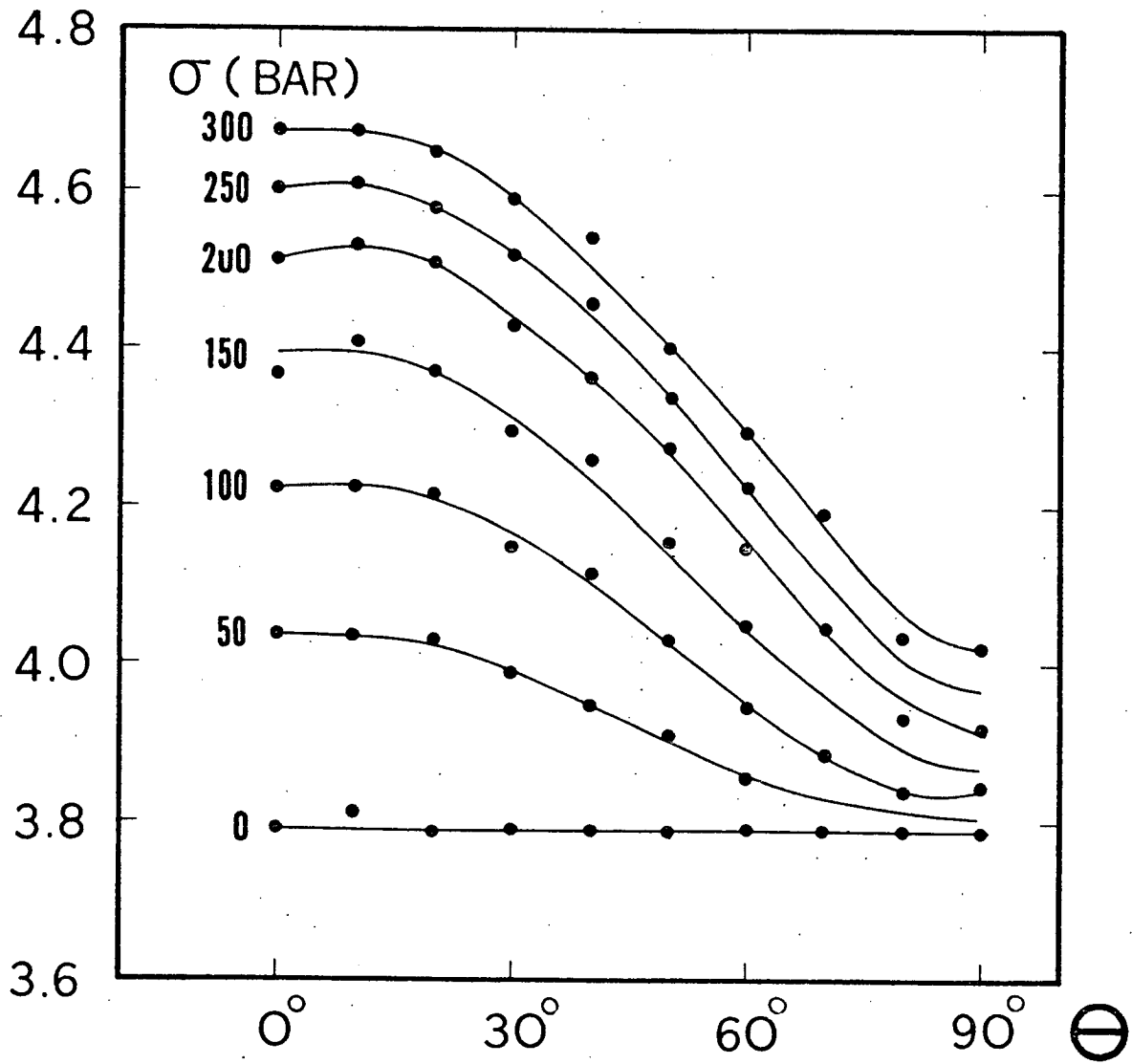
FIG 4.4
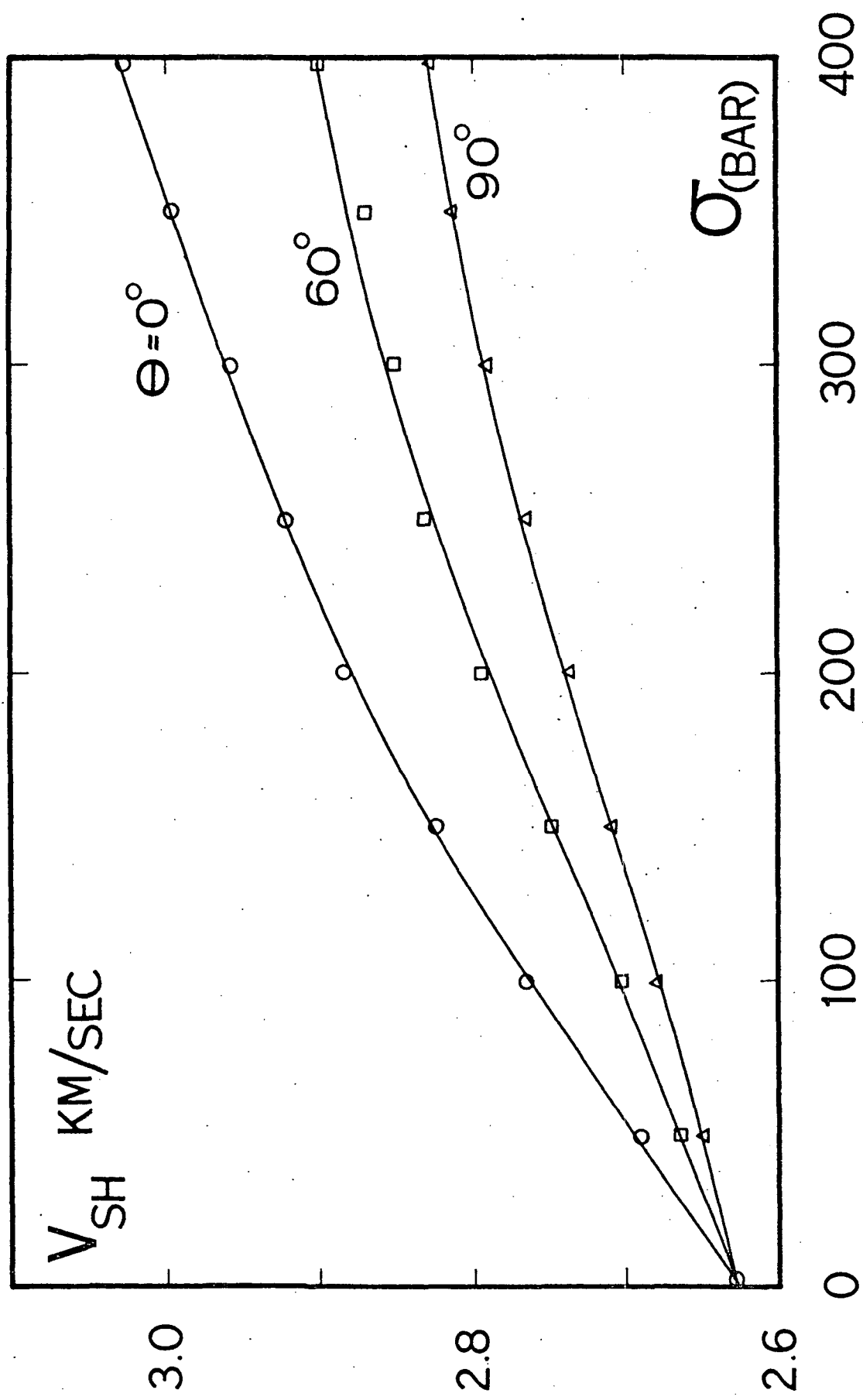
FIG 4.5
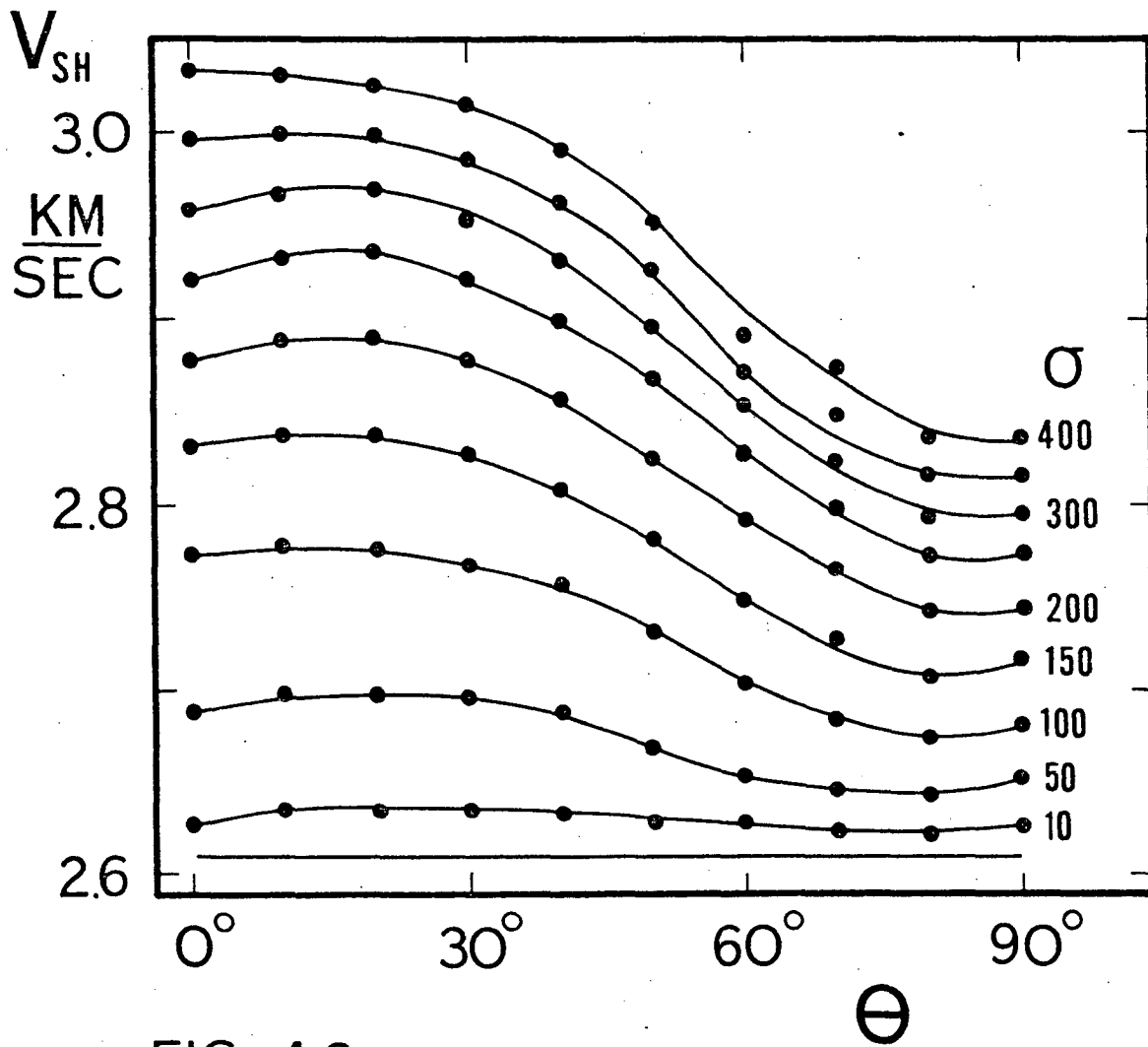
FIG. 4.6
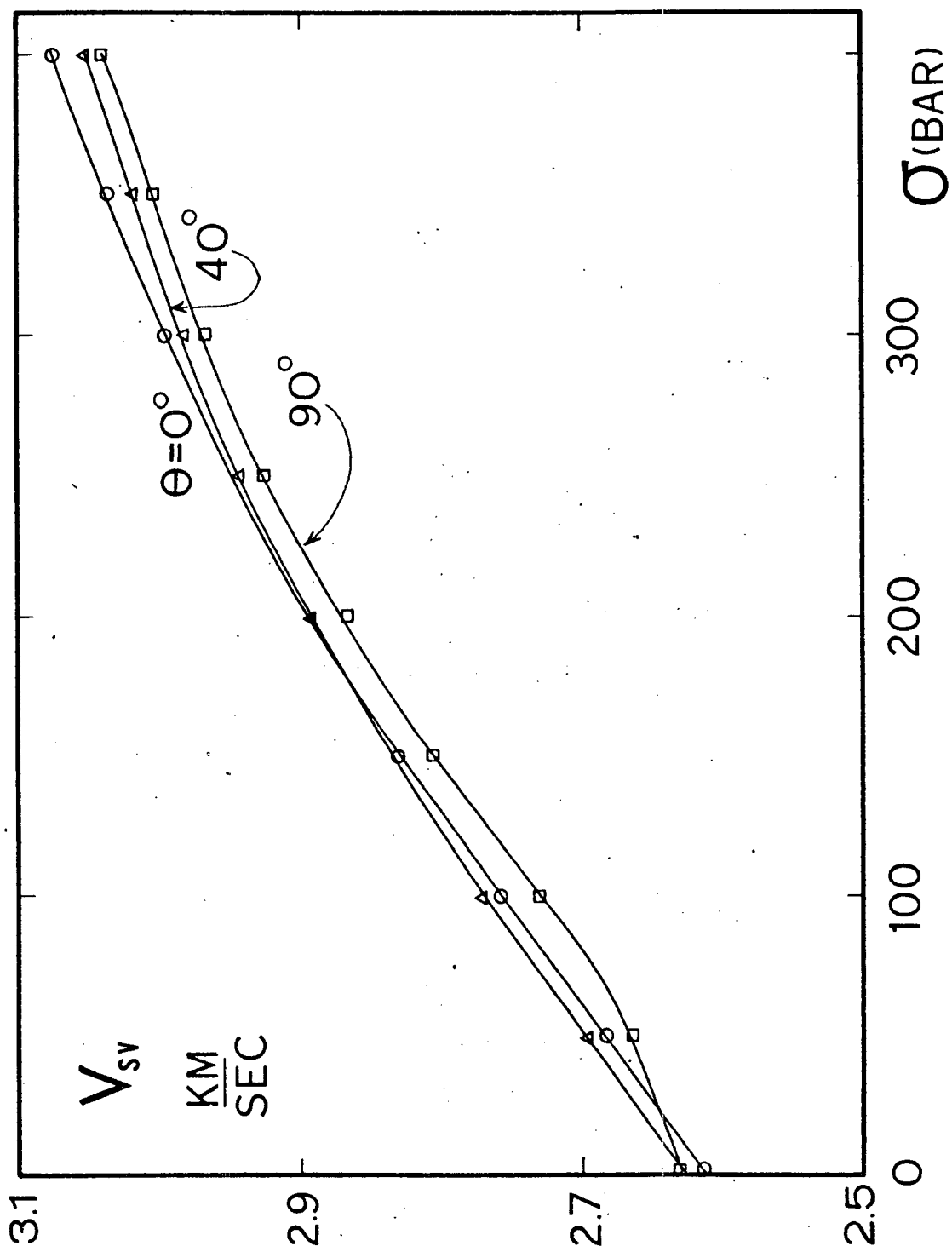
FIG. 4.7
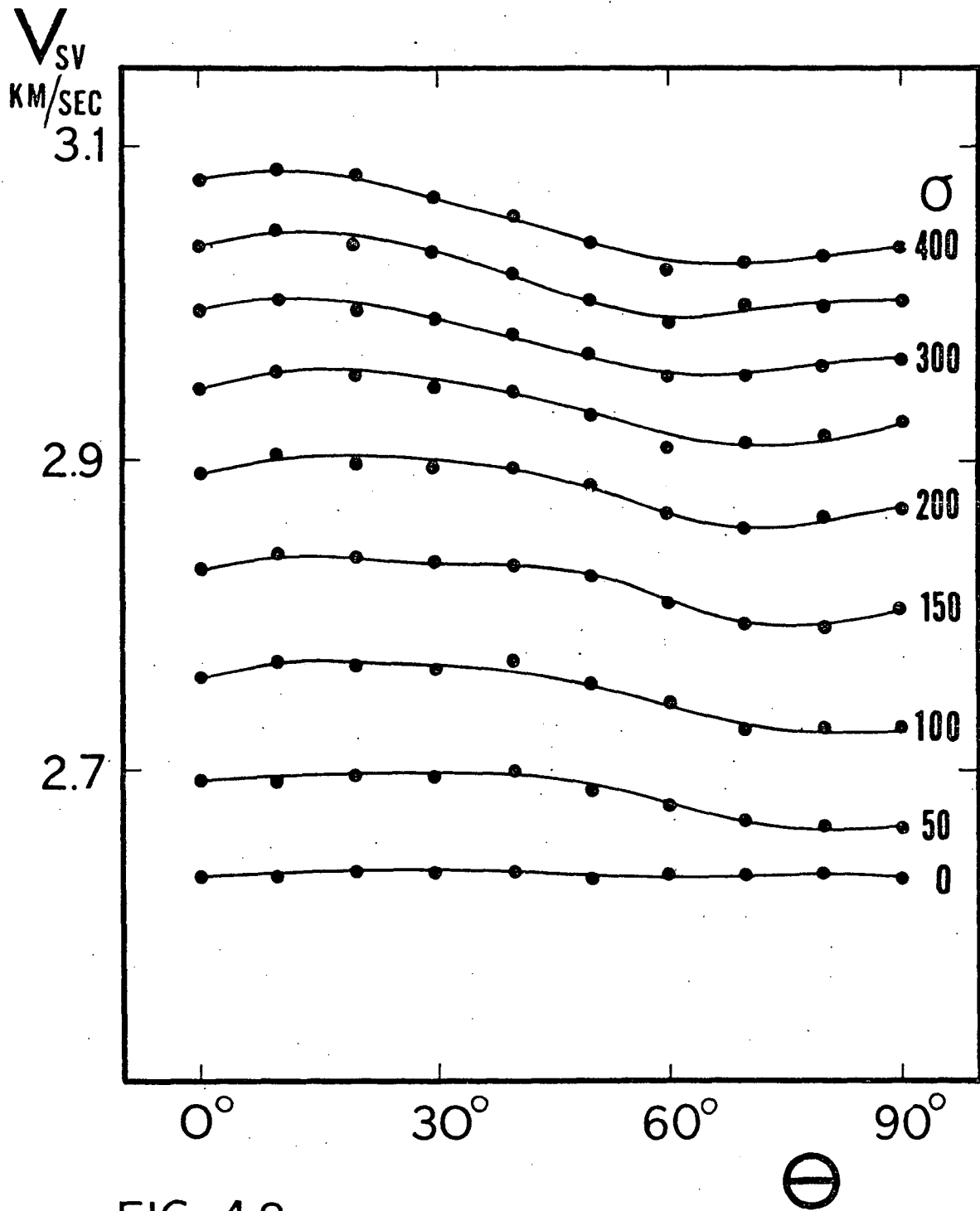
FIG. 4.8
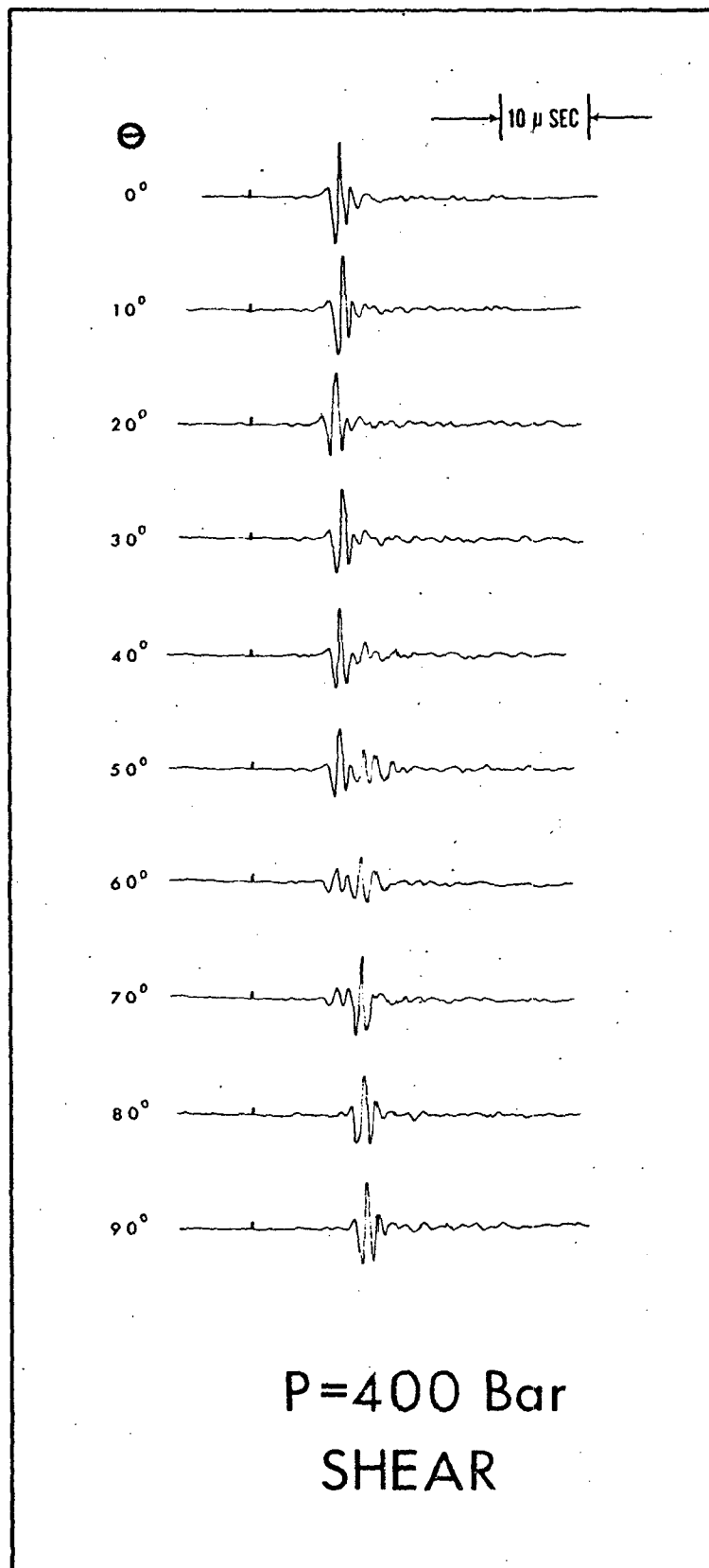
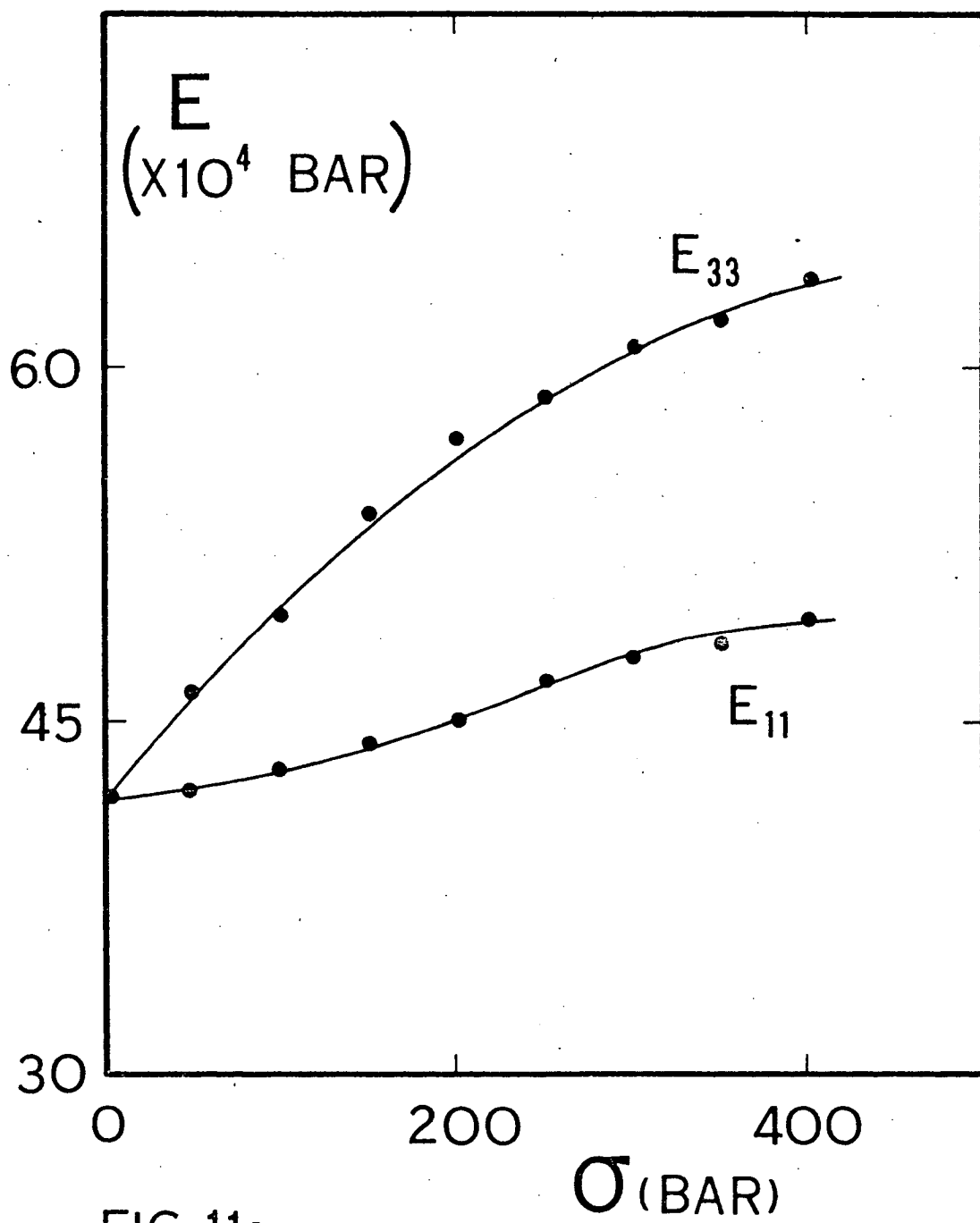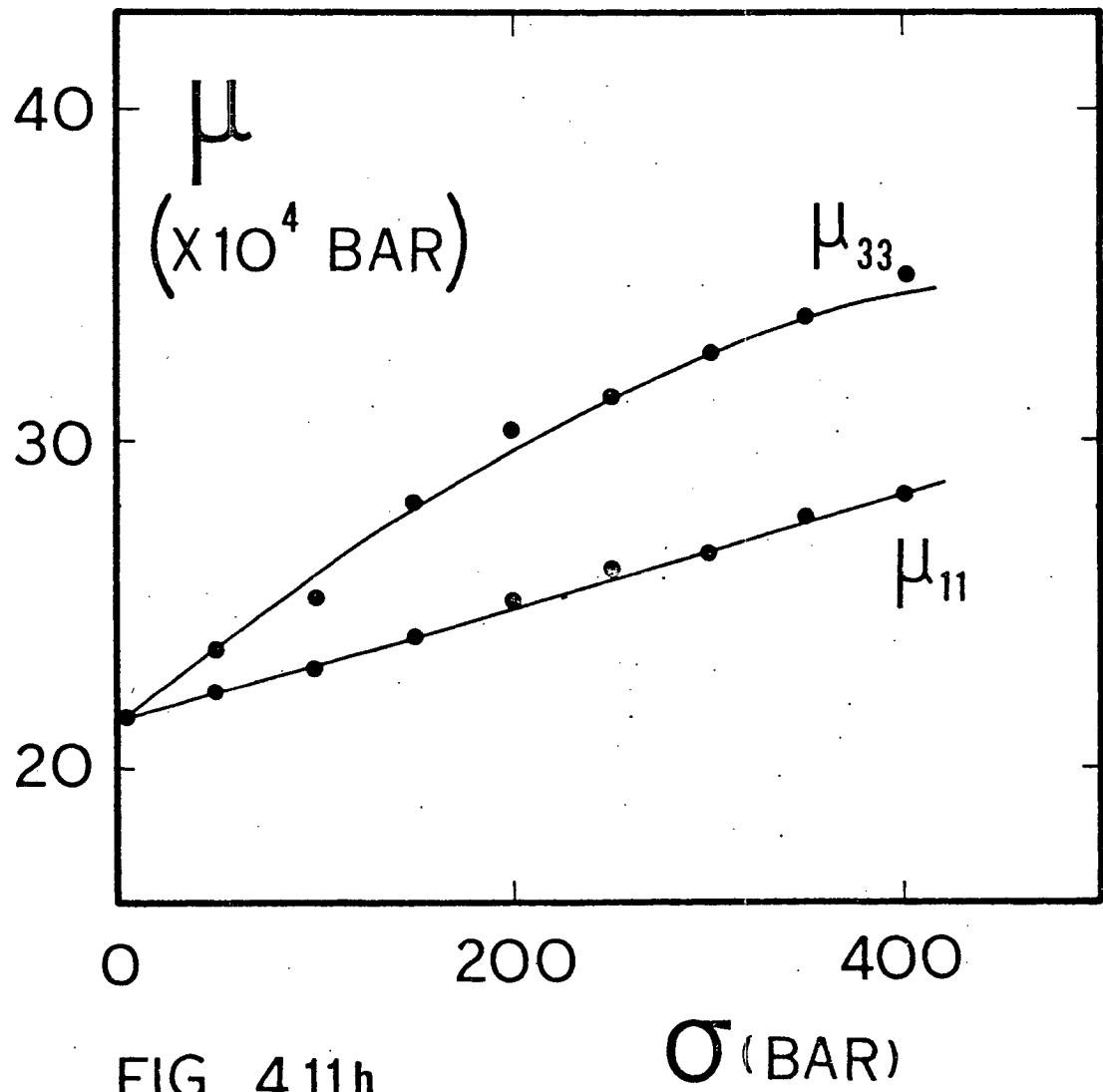FIG 4.9
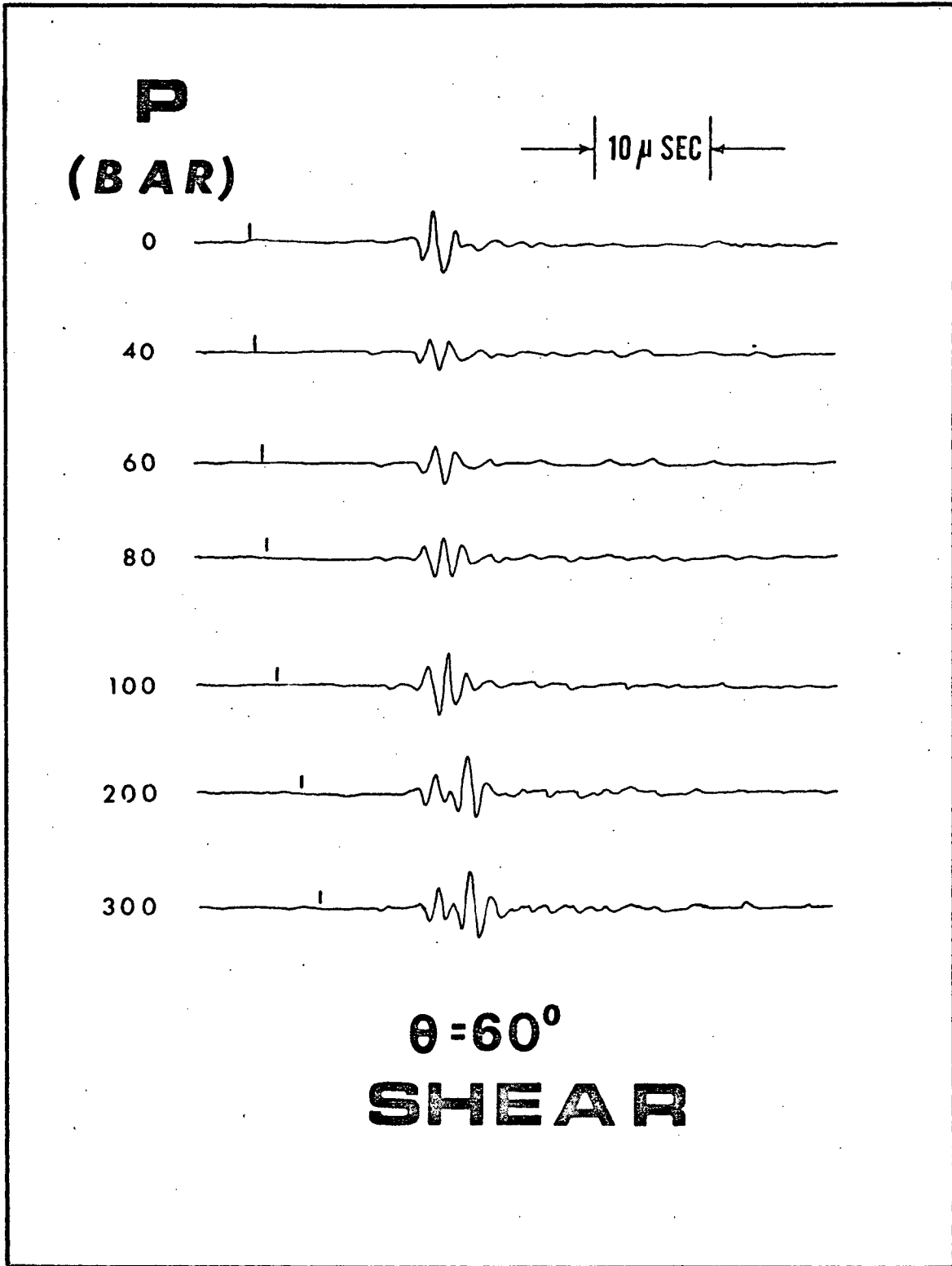
FIG   4.10 a
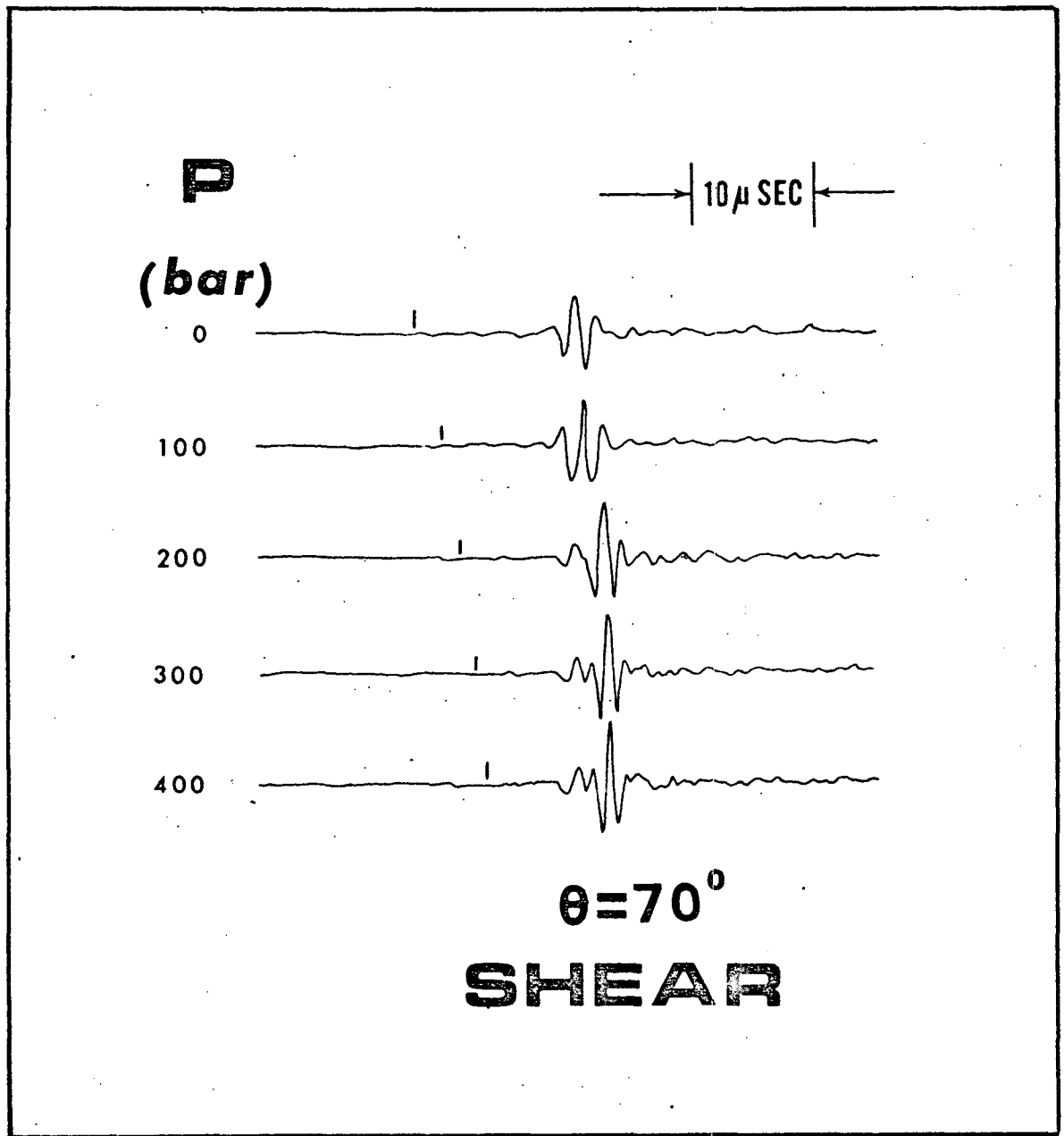
FIG 4.10 b
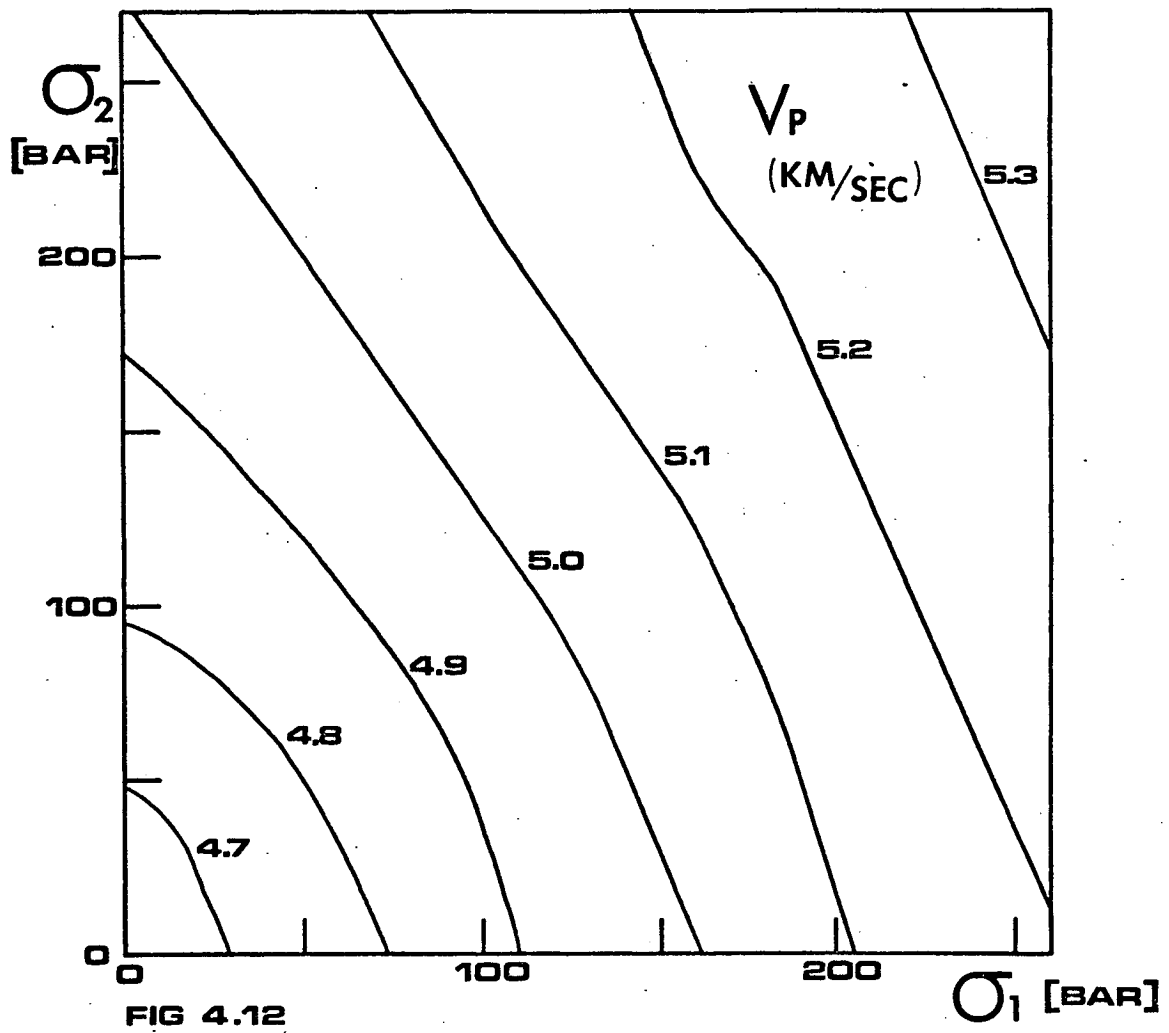
FIG. 11a

FIG. 4.11b

FIG 4.12

Chapter 5

Stress induced velocity anisotropy in rock: a
theoretical study

1. Introduction

Results of measurements of velocities in rock subject
to non-hydrostatic stress, reported in chapter 4 suggest
that the propagation of compressional and shear waves
through a stressed rock is very similar to wave propagation
in elastic crystals. Velocities were found to depend on
direction relative to the direction of the applied stress
and shear waves showed ultrasonic birefraction. These
effects, observed only at low effective stress are caused
by the presence of microcracks in the rocks, a suggestion
first made by Zisman (1933) to explain the pressure effects
on elastic properties.

The influence of stress on velocities is important for
crustal studies and possibly in the upper mantle. In
the crust most rock contains cracks and therefore exhibits
strong dependence of various properties on stress. In
the upper mantle the presence of zones of melt under high
pressure of viscous inclusions causes low effective stress
at which our results in chapter 4 are valid. In this chapter
we extend the theory of rock with random crack distribution,
derived by Walsh (1965a,b,c) to a non uniform distribution.

Walsh showed that an ellipsoidal crack in an elastic
medium closes when

$$\sigma_n = E\alpha \qquad\qquad 1.1$$

where E is Young's modulus, α = a/c is the ratio of the crack's width a to length c, and σ_n is the stress normal to the crack at great distance from it. Eq. 1.1 indicates that line cracks ($\alpha = 0$) close under very small stress whereas round pores ($\alpha = 1$) remain open under small stress. Changes with stress of an effective elastic property are associated with the change of the distribution of pores and cracks. Because rocks exhibit strong stress dependence of elastic properties only at relatively low stress levels, the aspect ratios of most of the cracks must be small.

Walsh (1965) also derived expressions for several elastic properties in terms of the intrinsic solid properties, crack shape, and the distribution of crack directions. His expressions can be applied to the effects of an increment of hydrostatic stress which causes a number of cracks, uniformly distributed in all directions, to close. If however, the applied stress increment is not hydrostatic the resulting effect is a crack distribution which depends on direction because cracks whose normals are parallel to the maximum stress will close before cracks with normals perpendicular to it. The mathematical development is simpler if we begin with a model in which all cracks have identical aspect ratio α and later generalize to a model with a distribution of $0 \leqslant \alpha \leqslant 1$.

We assume that the aspect ratio is sufficient for the

description of the shape of the cracks, and that the maximum crack length is small compared to the size of the sample in a static test or the wave length in a dynamic test. The term crack is restricted therefore in this paper to those discontinuities whose longest dimensions do not exceed the wave length of the dominant frequency in the ultrasonic experiment used to obtain the necessary data. As a practical limitation, the crack length must be less than about 1 cm.

2. Single α model and the effective Young's moduli

Suppose a rock contains penny shaped cracks which initially are randomly distributed in orientation. All cracks have identical aspect ratios, α . A crack will be closed if $\sigma_n \geqslant E\alpha$ where σ_n is the applied stress component normal to the crack. The angular distribution of open cracks under some simple condition of stress permits a generalization of Walsh's (1965b) expressions which relate isotropic crack distribution to effective elastic constants. For any modulus H_{ij} in the direction i and j,

$$\frac{1}{H_{ij}} = \frac{1}{H_0}\left[1 + m_{ij} \oint\!\!\oint N_{ij}(\theta,\beta) \sin^2\beta \cos\beta \, d\beta \, d\theta \right] \qquad 2.1$$

where

H_{ij} = effective elastic modulus in plane ij (i≠j)
        and/or direction i (i=j)

H_0 = intrinsic modulus of the solid

m_{ij} = a constant

$N_{ij}(\theta,\beta)$ = density of crack direction distribution

The angle β is measured from direction 1 and θ is measured in the orthogonal plane (fig. 5.1).

We define a general term

$$I_{ij} = \iint N_{ij}(\theta, \beta) \sin^2\beta \cos\beta \, d\beta \, d\theta \qquad \text{2.2}$$

clearly when the function N_{ij} is known the effective modulus can be obtained immediately. The crux of the problem then is to determine N_{ij}. If a uniaxial stress σ is applied in the direction $\varphi = 0$ then the normal stress component in direction φ is

$$\sigma_n(\varphi) = \sigma \cos^2\varphi \qquad \text{2.3}$$

cracks will be closed when $\sigma_n(\varphi) \geqslant E\alpha$. If φ_0 is the direction in which $\sigma_n = E\alpha$, then

$$\varphi_0 = \cos^{-1}\left[\left(\frac{E\alpha}{\sigma}\right)^{1/2}\right] \qquad \text{2.4}$$

In the case of hydrostatic pressure, all cracks remain open so long as $\sigma \leqslant E\alpha$ and all are closed when $\sigma \geqslant E\alpha$. It will be shown below that discontinuous crack closure occurs only when the spectrum of crack shapes is discrete. When two equal stresses are applied at $\varphi = 90^\circ$ ($\sigma_1 = \sigma_2$, $\sigma_3 = 0$) then

$$\varphi_0 = \sin^{-1}\left[\left(\frac{E\alpha}{\sigma}\right)^{1/2}\right] \qquad \text{2.5}$$

Consider first the uniaxial stress σ. All cracks whose normal directions β are larger than φ_0 remain open.

Integrating eq. 2.2 over all open cracks from φ_o to $\pi/2$ yields the expression for crack effects on Young's modulus E_{33}, parallel to the direction of uniaxial stress

$$I_{33} = 4 \int_0^\pi \int_{\varphi_o}^{\pi/2} \cos^2\beta \, \sin\beta \, d\beta = \frac{4\pi}{3} \cos^3\varphi_o$$

and from eq. 2.4

$$I_{33} = \frac{4\pi}{3} \left[\left(\frac{E\alpha}{\sigma}\right)^{3/2} \right] \qquad 2.6$$

For the effective Young's modulus in a direction perpendicular to a uniform tangential stress ($\sigma_1 = \sigma_2$, $\sigma_3 = 0$) the integration extends over the range $0 \leq \beta \leq \varphi_o$ and yields

$$I_{33}^* = 4 \int_0^\pi \int_0^{\varphi_o} \cos^2\beta \, \sin\beta \, d\beta = \frac{4\pi}{3} \left[1 - \cos^3\varphi_o \right]$$

and from eq. 2.5

$$I_{33}^* = \frac{4\pi}{3} \left[1 - \left(1 - \frac{E\alpha}{\sigma}\right)^{3/2} \right] \qquad 2.7$$

which is shown in fig. 5.2. The integration to obtain I_{11} for the Young's modulus perpendicular to the direction of uniaxial stress E_{11} is somewhat more complicated. At a given β (fig. 5.3)

$$L = \rho \cos\theta = R \cos\varphi_o$$

and

$$\rho = R \sin\beta$$

hence

$$\theta = \cos^{-1}\left[\frac{\cos\varphi_o}{\sin\beta} \right] \qquad 2.8$$

and the integration of eq. 2.2 yields

$$I_{11} = 2 \int_0^{\varphi_0} \int_0^{2\pi} d\theta' \cos^2\beta \sin\beta \, d\beta + \int_{\varphi_0}^{\pi/2} \int_\theta^{\pi/2} d\theta' \cos^2\beta \sin\beta \, d\beta$$

$$= \frac{4\pi}{3} \left[1 - \frac{6}{\pi} \int_{\pi/2-\varphi_0}^{\pi/2} \cos^{-1}\left(\frac{\cos\varphi_0}{\sin\beta} \right) \cos^2\beta \sin\beta \, d\beta \right] \qquad 2.9$$

which can be evaluated to yield (App. I)

$$I_{11} = \frac{2\pi}{3} \left[3 \left(\frac{E\alpha}{\sigma} \right)^{1/2} - \left(\frac{E\alpha}{\sigma} \right)^{3/2} \right] \qquad 2.10$$

3. The effective shear moduli for single α model

The relationship between the effective shear $\bar{\mu}_{ij}$ and Young's moduli $\bar{E}_{ii}$ will be used to obtain the $\bar{\mu}_{ij}$ by integrations which are similar to, or identical with, the ones used to obtain E_{ii} in the preceding sections.

Consider first a small pure shear applied to a material under uniaxial stress in the plane of the shear. (It is convenient in this section to rotate the coordinate system about the X_3 direction by $\pi/4$, as shown in fig. 5.4.) The pure shear $\Delta\sigma_{13}$ is equivalent to a combination of two equal, perpendicular axial stresses, $\Delta\sigma_{33}$ and $\Delta\sigma_{11}$ opposite in sign and at an angle of $\pi/4$ to the applied shear stress.

The two stresses $\Delta\sigma_{11}$, $\Delta\sigma_{33}$ cause displacements ΔU_1, ΔU_3 and strains $\Delta\epsilon_{11}$, $\Delta\epsilon_{33}$ in directions X_1, X_3, respectively.

For any material,

$$\Delta\epsilon_{11} = \frac{1}{\bar{E}_{11}} \left(\Delta\sigma_{11} - \bar{\nu}_{13} \Delta\sigma_{33} \right) \qquad 3.1$$

and

$$\Delta \epsilon_{33} = \frac{1}{\bar{E}_{33}} \left(\Delta \sigma_{33} - \bar{\nu}_{31} \Delta \sigma_{11} \right)$$

where the bar indicates effective quantity.

Following the method of MacKenzie (1949) and Satô (1953), we can relate the effective strains to displacements

$$\Delta \epsilon_{11} = \frac{\partial \Delta u_1}{\partial x_1} \approx \frac{\Delta u_1}{a}$$

$$\Delta \epsilon_{33} = \frac{\partial \Delta u_3}{\partial x_3} \approx \frac{\Delta u_3}{a}$$

3.2

where a is the dimension of an elastic element. For pure shear $\Delta \sigma_{11} = -\Delta \sigma_{33}$ and neglecting hysteresis, $\bar{E}_{33} = \bar{E}_{11}$ and $\bar{\nu}_{13} = \bar{\nu}_{31}$ we obtain

$$\frac{\Delta u_1}{a} = \frac{1 + \bar{\nu}_{13}}{\bar{E}_{11}} \Delta \tau_{13}$$

$$\frac{\Delta u_3}{a} = \frac{1 + \bar{\nu}_{31}}{\bar{E}_{33}} \Delta \tau_{13}$$

3.3

The effective shear modulus can now be obtained from the known displacements and stresses,

$$\Delta \epsilon_{13} = \frac{1}{2} \left(\frac{\partial \Delta u_1}{\partial x_3} + \frac{\partial \Delta u_3}{\partial x_1} \right) \approx \frac{1}{2} \left(\left| \frac{\Delta u_1}{a} \right| + \left| \frac{\Delta u_3}{a} \right| \right) = \frac{1 + \bar{\nu}_{31}}{\bar{E}_{33}} \Delta \tau_{13} \quad 3.4$$

Formally the shear stress-strain relations in a linear infinitesimal elastic solid are

$$\Delta \epsilon_{13} = \frac{1}{2\bar{\mu}_{13}} \Delta \tau_{13}$$

3.5

where $\bar{\mu}_{13}$ is the effective shear modulus and

$$\Delta \tau_{13} = \frac{1}{2} \left(\Delta \sigma_{11} + \Delta \sigma_{33} \right)$$

Hence

$$\frac{1}{2\bar{\mu}_{13}} = \frac{1 + \bar{\nu}_{31}}{\bar{E}_{33}}$$

or

$$\overline{\mu}_{13} = \frac{\overline{E}_{33}}{2(1+\overline{\nu}_{31})}$$ 3.6

This relationship is correct insofar as Poisson's ratio is assumed to be independent of a stress distribution. The correct value for Poisson's ratio will depend on the method employed to obtain the effective elastic constants and requires long and difficult analysis. Here we bypass this problem by assuming that the effective Poisson ratios are indeed independent of stress. It will be shown below that the corresponding error in velocity is small.

We obtain $\overline{\mu}_{13}$ from $\overline{E}_{33}$, the effective Young's modulus associated with crack distribution due to uniaxial stress, and now can evaluate the contribution of all open cracks to the effective Young's modulus in the plane of the applied stress, in the direction of pure shear. Thus the principal normal stresses which are applied at 45° to this direction cause non-symmetrical open crack distribution as shown in fig. 5.4. The integration over this crack distribution, evaluated in Appendix II, yields (fig. 5.2)

$$I_{13} = \frac{4\pi}{3}\left[3\left(\frac{E\alpha}{\sigma}\right)^{1/2} + \left(\frac{E\alpha}{\sigma}\right)^{3/2}\right]$$ 3.7

It is important to note that the influence of a stress applied at 45° is the same as the average of the effects of the same stress at 0° and 90°, namely that

$$I_{13} = \frac{1}{2}\left[I_{11} + I_{33}\right]$$ 3.8

It will be seen below that this relationship leads to shear modulus which is independent of direction in the X_1X_3 plane.

The problem of obtaining the shear modulus term I_{12} in the X_1X_2 plane is simpler than that of obtaining I_{13}. The effective shear modulus is related to the effective Young's modulus in the direction perpendicular to uniaxial stress, namely.

$$\overline{M}_{12} = \frac{E_{11}}{2(1 + \overline{\nu}_{12})} \qquad\qquad 3.9$$

with the corresponding expression

$$I_{12} = \frac{1}{2}\left[3\left(\frac{E\alpha}{\sigma}\right)^{1/2} - \left(\frac{E\alpha}{\sigma}\right)^{3/2}\right] \qquad\qquad 3.10$$

We have thus obtained estimates of I_{ij} which yield four elastic constants, using eq. 2.1 namely $\overline{E}_{33}$, $\overline{E}_{11}$, $\overline{M}_{13}$ and $\overline{M}_{12}$ by integration over the open cracks distributed under uniaxial stress. The E_{33} and E_{11} are the Young's moduli in the X_3 and X_1 directions, respectively. The $\overline{M}_{13}$ and $\overline{M}_{12}$ are the shear moduli in the plane perpendicular to X_2 and X_3 respectively.

4. A spectrum of α values

The results obtained so far for a single α model indicate some trends which can be compared with available data in a qualitative way. We notice that theoretically an effective elastic property in the direction of the applied stress is more influenced by stress than the same property in a perpendicular direction (figs. 5.1). Notice, however,

that our model with a single value of α does not describe adequately the elastic behavior of rock under hydrostatic pressure. In the model all cracks close at the same pressure and the variation in effective elasticity with pressure is discontinuous. This prediction does not agree with the experimental data that are available in chap. 3.

The single α results can be generalized however, to include a spectrum of α values $0 \leqslant \alpha \leqslant 1$ by superposition. We add not only contributions from cracks in various directions, as we have done so far, but also contributions from cracks with various shapes. In particular if the crack shape density distribution function $A(\alpha)$ is continuous, we need only integrate with respect to α. We denote the open crack contribution for the single model by $I(\alpha)$. Integrating over all crack shapes we obtain

$$Y_{ij} = \int_0^{\alpha_o} A(\alpha) \cdot I_{ij}(\alpha)\, d\alpha + \int_{\alpha_o}^1 A(\alpha)\, d\alpha \qquad 4.1$$

where $\alpha_o = \sigma/E$, σ being the current stress magnitude. The first term is the summed contribution of cracks with $\alpha < \alpha_o$

which are closed in some directions. The second term is the contribution of cracks with $\alpha > \alpha_o$, all of which are still open. Under hydrostatic stress conditions

$$Y_{HYDROS.} = \int_{\alpha_o}^1 A(\alpha)\, d\alpha \qquad 4.2$$

When uniaxial stress is applied the term for Young's modulus in the direction X_3 of the stress becomes

$$Y_{33} = \int_0^{\alpha_0} A(\alpha)\left(\frac{E\alpha}{\sigma}\right)^{3/2} d\alpha + \int_{\alpha_0}^1 A(\alpha)\, d\alpha \qquad 4.3$$

and for the shear modulus

$$Y_{13} = \frac{1}{4}\int_0^{\alpha_0}\left[3\left(\frac{E\alpha}{\sigma}\right)^{1/2} + \left(\frac{E\alpha}{\sigma}\right)^{3/2}\right] A(\alpha)\, d\alpha + \int_{\alpha_0}^1 A(\alpha)\, d\alpha \qquad 4.4$$

In direction X_1 perpendicular to the direction of the applied

stress

$$Y_{11} = \frac{1}{2}\int_0^{\alpha_0}\left[3\left(\frac{E\alpha}{\sigma}\right)^{1/2} - \left(\frac{E\alpha}{\sigma}\right)^{3/2}\right] A(\alpha)\, d\alpha + \int_{\alpha_0}^1 A(\alpha)\, d\alpha \qquad 4.5$$

and for the shear modulus

$$Y_{12} = Y_{11} \qquad 4.6$$

It is therefore possible to determine these four

moduli in a stressed rock, given the spectrum density

function of the crack parameter and the state of stress.

The integrals we derived can be utilized to obtain the

velocity under uniaxial conditions but we must first find a

simple way to obtain the initial crack spectrum $A(\alpha)$.

5. Determination of the spectrum of crack shapes

Consider the hydrostatic loading test. From Walsh

(1965a) we find that under this stress condition an effective

elastic property $\tilde{E}$ can be obtained from the corresponding

intrinsic property E_0 and crack parameters

$$m\left(\frac{E_0}{\tilde{E}} - 1\right) = N \qquad 5.1$$

where m is a numerical constant and N is the total number

of cracks. The value of N is related to the aspect ratio

density function $A(\alpha)$ thru

$$\int_{\alpha_o}^{1} A(\alpha)\, d\alpha = N \qquad \text{and} \qquad \int_{o}^{1} A(\alpha)\, d\alpha = N_o \qquad 5.2$$

or in a differential form

$$\frac{dN}{d\alpha} = A(\alpha) \qquad 5.3$$

where α is obtained from $\quad \alpha = P/E_o$

thus

$$\frac{dN}{dP} = \frac{dN}{d\alpha} \cdot \frac{d\alpha}{dP} = \frac{A(\alpha)}{E_o} \qquad 5.4$$

or

$$A(\alpha) = E_o \frac{dN}{dP} \qquad 5.5$$

but from eq. 5.1

$$\frac{dN}{dP} = \frac{d}{dP}\left(m \frac{E_o}{\bar{E}}\right) \qquad 5.6$$

which can be obtained from measurements of E under hydro-

static pressure.

Thus

$$A(\alpha) = E_o\, m \frac{d}{dP}\left(\frac{E_o}{\bar{E}}\right) \qquad 5.7$$

similarly

$$A(\alpha) = M_o\, m' \frac{d}{dP}\left(\frac{M_o}{\bar{M}}\right) \qquad 5.8$$

The aspect ratio density distribution function can

therefore be obtained from the measurement of an elastic property as a function of hydrostatic pressure. If a rock with cracks is initially isotropic then $A(\alpha)$ is sufficient to determine its behavior under a general state of stress.

On the basis of the symmetry of a uniaxial stress field we assume that the associated induced anisotropy has hexagonal symmetry with fine independent elastic constants. We can write the stiffness tensor (Bisplinghof et al. 1966)

$$\sigma_{ij} = C_{ijk\ell} \in_{k\ell}$$

and the compliance tensor

$$\in_{ij} = S_{ijk\ell} \in_{k\ell}$$

In terms of the more familiar technical constants we have (Lekhnitski, 1963)

$$S_{1111} = 1/E_{11} \qquad\qquad S_{1122} = -\nu_{12}/E_{11}$$
$$S_{3333} = 1/E_{33} \qquad\qquad S_{1212} = 1//\mu_{12} \qquad\qquad 5.9$$
$$S_{1133} = -\nu_{13}/E_{11} = -\nu_{31}/E_{33} \qquad S_{1313} = 1//\mu_{13}$$

We can also obtain the C_{ijkl} without much difficulty. For small values of ν_{ij} the values of C_{ijkl} are, within a few percent

$$C_{3333} = E_{33} \qquad\qquad (\pm\ .2\%)$$
$$C_{1111} = E_{11} \qquad\qquad (\pm\ .2\%) \qquad\qquad 5.10$$
$$C_{1122} = -\nu_{12}\, E_{11} \qquad\qquad (\pm\ 1\%)$$
$$C_{1133} = -\nu_{13}\, E_{11} = -\nu_{31}\, E_{33} \qquad (\pm\ 1\%)$$

and exactly by

$$C_{1212} = \mu_{12}$$
$$C_{1313} = \mu_{13}$$

The approximate errors in the first four terms, computed
from the values in Chapter 3, are given in parentheses. They
do not exceed 1% for the off-diagonal elements and a fraction
of a percent for the diagonal elements. From Sections 4
and 5 we already have expressions for $1/E_{11}$, $1/E_{33}$, $1/\mu_{12}$
and $1/\mu_{13}$. The value of γ_{12}/E_{11} can be obtained from eq.
5.9 while expressions for γ_{13}/E_{11} or γ_{31}/E_{33} have not been
derived so far. Walsh (1965c) derived an approximate
expression for Poisson's ratio in rock with cracks but the
extension of his results to the anisotropic case is lengthy
and will not be derived. Instead we will obtain these
values from eq. 21 in app. III. It can be shown, from the
experimental values of γ_{ij} in the previous chapter, that
errors in the effective elastic of constants of ones a few
percent are introduced through the use of eq. 21. (App. III).

6. Aspect ratio distribution in Barre granite

The aspect ratio density function $A(\alpha)$ can be expressed
numerically or by some analytic fit to data. Most such
analytic expressions involve excessive computation which
tend to complicate our present investigation. Furthermore,
both Westerly and Barre granite samples show an initial
velocity anisotropy variation of about 10%, which implies
an initial crack distribution that is anisotropic. However,
the stress induced velocity anisotropy is not greatly affected
by the initial anisotropy if all velocities, or other per-

tinent elastic parameters, are measured along the same path through the sample while the various stresses are applied in different directions. For Barre granite, the absolute error in velocity does not exceed 2% which is negligible for the present analysis. Instead of an exact fit to the data, $A(\alpha)$ is approximated by the simple form

$$A(\alpha) = A_0 - A_1 \alpha \qquad \text{for} \quad \alpha \leq A_0/A_1 = \beta \qquad 6.1$$
$$= 0 \qquad \text{for} \quad \alpha > \beta$$

This function is shown in fig. 5.5 together with the numerically derived spectrum from measurements in a single direction in Barre and Westerly granites. Because the final velocity values are obtained by integration of $A(\alpha)$ the linear approximation employed here is satisfactory. The value $A_1 = A_0/\beta$ is obtained at $\alpha = \beta$, where $\beta = \sigma_0/E_0$ and where σ_0 denotes the pressure at which all cracks are closed under hydrostatic stress. For Westerly $\beta \approx .2 \times 10^{-3}$ and for Barre $\beta \approx .5 \times 10^{-3}$. Equations 4.2 to 4.6 are integrated in appendix III to yield the effective elastic constants, which are used to obtain the wave velocities in terms of the intrinsic velocities V_p^0 and V_s^0. The velocities in the Barre granite are, for hydrostatic stress σ

$$V_P = V_p^0\left\{1 + 2.5\left[\frac{1}{2} - \left(\frac{\sigma}{E\beta}\right) + \frac{1}{2}\left(\frac{\sigma}{E\beta}\right)^2\right]^{1/2}\right\} \quad \text{for} \quad \sigma \leq E\beta \qquad 6.2$$
$$= V_p^0 \qquad \text{for} \quad \sigma \geq E\beta$$

and

$$V_S = V_s^0\left\{1 + 1.92\left[\frac{1}{2} - \left(\frac{\sigma}{E\beta}\right) + \frac{1}{2}\left(\frac{\sigma}{E\beta}\right)^2\right]^{-1/2}\right\} \quad \text{for} \quad \sigma \leq E\beta \qquad 6.3$$
$$= V_s^0 \qquad \text{for} \quad \sigma \geq E\beta$$

The velocity of waves propagating in the direction of an applied uniaxial stress σ,

$$V_{P33} = V_P^0 \left\{ 1 + 2.5\left[\tfrac{1}{2} - \tfrac{3}{5}\left(\tfrac{\sigma}{E\beta}\right) + \tfrac{3}{14}\left(\tfrac{\sigma}{E\beta}\right)^2\right]\right\}^{-1/2} \text{ for } \quad \sigma \leqslant E\beta \qquad 6.4$$

$$= V_P^0 \left\{ 1 + \tfrac{10}{35}\left(\tfrac{E\beta}{\sigma}\right)^{3/2}\right\}^{-1/2} \qquad\qquad \text{ for } \quad \sigma \geqslant E\beta$$

and the wave polarized in the plane including the stress direction

$$V_{S13} = V_S^0 \left\{ 1 + 1.92\left[\tfrac{1}{2} - \tfrac{2}{5}\left(\tfrac{\sigma}{E\beta}\right) + \tfrac{9}{70}\left(\tfrac{\sigma}{E\beta}\right)^2\right]\right\}^{-1/2} \text{ for } \quad \sigma \leqslant E\beta \qquad 6.5$$

$$= V_S^0 \left\{ 1 + 1.92\left[\tfrac{1}{5}\left(\tfrac{E\beta}{\sigma}\right)^{1/2} + \tfrac{1}{35}\left(\tfrac{E\beta}{\sigma}\right)^{3/2}\right]\right\}^{-1/2} \text{ for } \quad \sigma \geqslant E\beta$$

and finally the velocity of the waves propagating in a direction normal to the applied uniaxial stress

$$V_{P11} = V_P^0 \left\{ 1 + 2.5\left[\tfrac{1}{2} - \tfrac{1}{5}\left(\tfrac{\sigma}{E\beta}\right) + \tfrac{3}{70}\left(\tfrac{\sigma}{E\beta}\right)^2\right]\right\}^{-1/2} \text{ for } \quad \sigma \leqslant E\beta \qquad 6.6$$

$$= V_P^0 \left\{ 1 + 2.5\left[\tfrac{2}{5}\left(\tfrac{E\beta}{\sigma}\right)^{1/2} - \tfrac{2}{35}\left(\tfrac{E\beta}{\sigma}\right)^{3/2}\right]\right\}^{-1/2} \text{ for } \quad \sigma \geqslant E\beta$$

and

$$V_{S12} = V_S^0 \left\{ 1 + 1.92\left[\tfrac{1}{2} - \tfrac{1}{5}\left(\tfrac{\sigma}{E\beta}\right) + \tfrac{3}{70}\left(\tfrac{\sigma}{E\beta}\right)^2\right]\right\}^{-1/2} \text{ for } \quad \sigma \leqslant E\beta \qquad 6.7$$

$$= V_S^0 \left\{ 1 + 1.92\left[\tfrac{2}{5}\left(\tfrac{E\beta}{\sigma}\right)^{1/2} - \tfrac{2}{35}\left(\tfrac{E\beta}{\sigma}\right)^{3/2}\right]\right\}^{-1/2} \text{ for } \quad \sigma \geqslant E\beta$$

For Barre granite we used $V_p^0 = 5.90$ km/sec and $V_s^0 = 3.65$ km/sec. The computed velocities are compared with the measured values in fig. 5.6. The agreement is quite good. The small discrepancy in V_p is probably due to the simplified form of $A(\alpha)$. Perhaps the clearest agreement

between model and data is seen in the relatively small difference between the two shear velocities and the large differences between the two compressional wave velocities.

The velocities in various directions other than the principal directions of stress can be found from the general expressions for velocities in anisotropic media. Brady (1969) suggested that the effective elastic constants in any direction should be obtained through an integration over the open crack distribution about that direction. The anisotropy resulting from Brady's method will generally be inconsistent with the anisotropy of a general linear elastic solid and the relationship between elastic constants and wave velocities will not be that which is found for linear elastic solids. Because we have assumed that the effective elastic constants are related to the wave velocities in rock much like the relations in a linear elastic solid, which implies the validity of the linear wave equation, we can obtain the various elastic properties from their principal values using only one transformation namely that of a fourth rank tensor. Any other transformation is inconsistant with linear elastic velocity anisotropy. For uniaxial loading this anisotropy is hexagonal with the added empirical condition based on the data in ch. 3 that V_{sl3} does not depend on direction. The velocities of elastic waves propagating in a given direction with respect to the direction of the applied stress can therefore be expressed

very simply in terms of the largest $(V_\parallel)$ and smallest $(V_\perp)$ velocities which are parallel and perpendicular to the applied stress, respectively (Appendix III).

$$V^2 = V_\perp^2 + (V_{\parallel}^2 - V_\perp^2)\cos^2\theta \qquad 6.8$$

which is valid for both V_p and V_{s12}. The second shear velocity equals the largest value of V_{s12}, namely

$$V_{S13}(\theta) = V_{S12}\big|_{\theta=0} \qquad 6.9$$

The surface representing the dependence of both V_p^2 and V_{s12}^2 on direction is spheroidal. The highest velocity is in the direction of the applied stress and the smallest is perpendicular to it. The computed values of V_p^2 and V_{s12}^2 are compared with the measured values for Barre granite in fig. 5.7. These results indicate satisfactory agreement between theory and data.

7. Application to stress changes associated with faulting.

The results of this analysis can be used to estimate the pattern of velocity changes that occur around active strike slip faults, such as the San Andreas fault. The stress accumulation around such a long fault can be considered as pure shear (Knopoff 1958, Chinnery 1963). The magnitude of the shear stress increases with time until faulting occurs. This motion releases part of the stress which is also pure shear. Pure shear of magnitude σ is statiscally equivalent to a compression σ and tension $-\sigma$

applied at 45° to the direction of the shear in the horizontal plane (fig. 5.8).

The velocity anisotropy induced by pure shear has the symmetry of the orthorhombic system with nine elastic constants--three distinct principal directions at right angles to each other. It can be shown however that only 5 elastic constants are required to describe adequately the wave velocities in a plane perpendicular to a principal direction. In the case of the crust under pure shear this plane is horizontal, and we can consider the dependence of velocity on direction in this plane only.

Assuming that the compressional wave velocity is similar in this two dimensional case to the hexagonal system the $(V_p)^2$ surface will have an elliptic shape, as indicated by eq. 6.8, namely,

$$V_0^2 = a_0^2 \sin^2\theta + b_0^2 \cos^2\theta \qquad 7.1$$

a_0 is the compressional wave velocity in the direction of tension and b_0 in the direction of compression, both roughly $\pi/4$ from the fault plane.

Suppose shear stress has changed over a period of time and a new velocity distribution exists

$$V_1^2 = a_1^2 \sin^2\theta + b_1^2 \cos^2\theta \qquad 7.2$$

where

$$a_1 = a_0 + \Delta a \qquad \text{and} \qquad b_1 = b_0 + \Delta b$$

Because the magnitude of the change in compression equals
that in tension the velocity changes will also be approximate-
ly equal in magnitude while opposite in sign or

$$\Delta a = -\Delta b \qquad\qquad 7.3$$

combining eq.7.1 to 7.3 and neglecting higher order terms of Δb

$$V_1^2 - V_0^2 \approx \frac{2\Delta b}{V_0}\left(\cos^2\theta - \sin^2\theta\right) \qquad\qquad 7.4$$

also

$$V_1^2 - V_0^2 \approx \Delta V \cdot 2V_0 \qquad\qquad 7.5$$

thus the change of velocity associated with the change of
pure shear has the form

$$\Delta V \approx \Delta b \left(\cos^2\theta - \sin^2\theta\right) \qquad\qquad 7.6$$

where θ is measured from the direction of maximum compression.
Values of $\Delta b > 0$ correspond to increasing shear stress while
$\Delta b < 0$ corresponds to decreasing stress such as that due
to sudden motion on the fault.

The change of velocity is positive in the direction
of compression and negative in the direction of tension.
No velocity change will occur either along or normal to
the fault plane at $\theta \approx \pi/4$, as shown in fig. 5.8.

Eisler (1969) obtained compressional wave velocity
changes in directions roughly parallel and perpendicular
to the San Andreas fault in the Gabilan range in Cali-

fornia and interpreted the drop of velocity to indicate
reduction of stress. Our results clearly indicate that an
increase or a decrease of shear stress always causes velocity
to decrease in some directions and increase in others.
Therefore it is necessary to determine stress changes from
at least three velocity profiles in different directions.

It is important to evaluate the influence of the pre-
sence of water in rocks _in situ_. It was shown in chap. 2
that the presence of water greatly increases V_p while V_s
is almost unaffected. The bulk modulus of a water saturated
rock is similar to the modulus of the rock without cracks.
The compressional velocity will vary with direction in a
saturated and stressed rock depending on the variation of
the effective shear modulus, or shear wave velocity. The
change of velocity, however, due to a change of stress will
be much smaller than in the dry rock. The measurements on
dry and saturated rock (chap. 2) indicate that in dry
granites $dV_p/dP \approx .01$ km/sec. bar while in saturated
rock $dV_p/dP \approx .003$ km/sec bar. The shear wave velocity does
not depend much on saturation, and the change of velocity
with stress in saturated rock will be equal to the change
in dry rock.

8. Conclusions

The general stress dependence of the elastic response
in any direction of a rock with cracks can be predicted
from the measurement of this response to hydrostatic stress.

All of the main features of the measured velocities in a rock subject to uniaxial stress appear also in the theoretical expressions.

The importance of the initial crack distribution is quite clear from our analysis. An anisotropic distribution does not however pose a great obstacle in the analysis and if known can be included in the crack shape density function $A(\alpha)$ which now becomes direction dependent. A geometrical series expression such as

$$A(\alpha, \eta) = A_0 + A_1 \cos^2 \eta + A_2 \cos^4 \eta + \ldots . \qquad 8.1$$

can probably be used and it seems most likely that retaining A_i only up to A_1 will suffice for most rocks.

It is possible to obtain this more generalized crack shape density function from a limited number of velocity measurements in various directions on unstressed rock samples (Aleksandrov et al. 1968). In the case of hexagonal symmetry the analysis in this chapter is applicable and with some modifications can be used to yield $A(\alpha, \eta)$.

The extension of the analysis from uniaxial stress applied to isotropic rock to triaxial (three distinct principal stresses) stress is conceptually easy but the computations become increasingly more complicated as the expressions for the distribution of open cracks become more complicated. Numerical methods can be used when necessary. Of the various possible triaxial loadings the biaxial ex-

perimental arrangement ($\sigma_1 \neq \sigma_2$, $\sigma_3 = 0$) can be easily achieved by applying stress to the flat ends of the cylindrical sample which was described in chapter 3 (fig. 4.1).

We can speculate on the extension of the correspondence between the symmetries of the stress field and the stress induced velocity anisotropy to more general cases of initial crack anisotropy and triaxial stress. Various combinations are presented in Table 5.1 indicating that all the elastic symmetry systems should be anticipated. Of particular importance is the influence of the direction of application of stress with respect to the principal directions of initial anisotropy. The resulting induced anisotropy probably depends significantly on this relative direction-- if for example the material possesses initially hexagonal symmetry of apparent elastic properties and the applied stress is uniaxial the resulting anisotropy can be hexagonal, orthorhombic, or monoclinic depending on the direction of the principal stress.

Despite the complications that arise from generalizing our results, a basic theory permits now the prediction of velocities of elastic waves in rocks which have an initial and stress induced velocity anisotropy, and its dependence on stress. The determination of the necessary crack parameters is simple and practical.

APPENDIX 1

Integration of crack contributions to

transverse Young's modulus

The value of I_{1j} (eq. 2.9) is to be evaluated

$$I_{11} = 1 - \frac{6}{\pi} \int_{\pi/2 - \varphi_0}^{\pi/2} \cos^{-1}\left[\frac{\cos\varphi_0}{\sin\beta}\right] \cos^2\beta \, \sin\beta \, d\beta \qquad 1.$$

Let $\quad J = \frac{\pi}{6}\left(1 - I_{11}\right) \qquad\qquad 2.$

and if $\quad \beta = \pi/2 - \alpha \quad, \quad d\beta = -d\alpha \qquad\qquad$ (fig. 5.3)

then

$$J = \int_0^{\varphi_0} \cos^{-1}\left[\frac{\cos\varphi_0}{\cos\alpha}\right] \sin^2\alpha \cos\alpha \, d\alpha \qquad 3.$$

Let $\quad z = \cos\alpha \qquad\qquad$ and $\qquad \cos\varphi_0 = 1/k$

$$J = \int_1^k \cos^{-1}\left(\frac{z}{k}\right) \frac{(z^2-1)^{1/2}}{z^4} dz \qquad 4.$$

Integration by parts yields

$$J = \frac{1}{3} \int_1^k \frac{(z^2-1)^{3/2} \, dz}{z^3 (k^2 - z^2)^{1/2}} \qquad 5.$$

Substitute $\quad z = k/(x^2+1)^{1/2}$

$$J = \frac{1}{3k^3} \int_0^{\sqrt{k^2-1}} \frac{(k^2-1-x^2)^{3/2}}{x^2+1} dx \qquad 6.$$

and again substitute $\quad x = (k^2-1)\sin\theta$

$$J = \frac{K^2-1}{6K^3} \int_0^{\pi/2} \frac{1+2\cos2\theta+\cos^2 2\theta}{(K^2+1)/(K^2-1)-\cos2\theta} \, d\theta =$$

$$= -\frac{(K^2-1)}{6K^3} \cdot \frac{\pi}{2}\left(2+\frac{K^2+1}{K^2-1}\right) + \frac{2K}{3}\int_0^{\pi/2} \frac{d\theta}{(K^2+1)-(K^2-1)\cos2\theta}$$

Substitute $\eta = \tan\theta$

$$J = \frac{\pi(1-3K^2)}{12K^3} + \frac{K}{3}\int_0^{\infty} \frac{d\eta}{1+K^2\eta^2} = \frac{\pi(K-1)^2(2K+1)}{12K^3}$$

and since $\cos\varphi_0 = 1/K$

$$I_{\parallel} = 1 - \frac{1}{2}\left(1-\cos\varphi_0\right)^2\left(2+\cos\varphi_0\right)$$

or

$$I_{\parallel} = \frac{1}{2}\left(3\cos\varphi_0 - \cos^3\varphi_0\right)$$

expression 3 was also evaluated by a numerical integration and the results are identical to eq. 10. Introducing eq. 2.4 in 10. we find

$$I_{\parallel} = \frac{2\pi}{3}\left[3\left(\frac{E\alpha}{\sigma}\right)^{1/2} - \left(\frac{E\alpha}{\sigma}\right)^{3/2}\right]$$

APPENDIX II.

Integration of open crack contributions to the

effective shear modulus in the plane of an applied

uniaxial stress

First we seek an expression for the angle θ (fig.

5.4) at a given β .

We notice that as long as $\beta < \pi/4$

$$L = b - z \qquad \qquad 1.$$

and

$$b = \sqrt{2} \cdot R \cos \varphi_0 \qquad \qquad 2.$$

also

$$Z = R \cos \beta \qquad \qquad 3.$$

and

$$L = \rho \cos \theta = R \sin \beta \cos \theta$$

hence

$$\sin \beta \cos \theta = \sqrt{2} \cos \varphi_0 - \cos \beta$$

or

$$\theta = \cos^{-1} \left[\frac{\sqrt{2} \cos \varphi_0 - \cos \beta}{\sin \beta} \right] \qquad \qquad 4.$$

The required integral is now, from eq. 2.2, over all

open cracks

$$I_{13} = 4\pi \int_0^{\pi/4 - \varphi_0} \cos^2 \beta \sin \beta \, d\beta + 4 \int_{\pi/4 - \varphi_0}^{\pi/4 + \varphi_0} \left[\int_0^{\pi} d\theta' \right] \cos^2 \beta \sin \beta \, d\beta \qquad 5.$$

$$+ 4\pi \int_{\pi/4 + \varphi_0}^{\pi/2} \cos^2 \beta \sin \beta \, d\beta = \frac{4\pi}{3} - 4 \int_{\pi/4 - \varphi_0}^{\pi/4 + \varphi_0} \cos^{-1} \left[\frac{\sqrt{2} \cos \varphi_0 - \cos \beta}{\sin \beta} \right] \cos^2 \beta \sin \beta \, d\beta = \frac{4\pi}{3} - 4.]$$

where J is the integral to be evaluated.

Integrating by parts

$$J = \int_{\pi/4-\varphi_0}^{\pi/4+\varphi_0} \frac{(1-\sqrt{2}\cos\varphi_0\cos\beta)\cos^2\beta \, d\beta}{\sin\beta[\sin^2\beta - (\sqrt{2}\cos\varphi_0-\cos\beta)^2]^{1/2}} \qquad 6.$$

Let $\quad X = \cos\beta, \quad C = \dfrac{\cos\varphi_0}{\sqrt{2}} \qquad$ and $\qquad S = \dfrac{\sin\varphi_0}{\sqrt{2}}$

and

$$J = \frac{1}{3}\int_{C-S}^{C+S} \frac{(2cX^4 - X^3)\, dX}{(1-4c^2+4cX-2X^2)^{1/2}(X^2-1)} \qquad 7.$$

Letting $\quad \sin\theta = \dfrac{X-c}{S}$

$$J = \frac{1}{3\sqrt{2}}\int_{-\pi/2}^{\pi/2}\Big[2c^3 + 4c^2s\cdot\sin\theta + 2cs^2\sin^2\theta - c - s\cdot\sin\theta + 2c \qquad 8.$$

$$-\frac{c+\frac{1}{2}}{c+1+s\cdot\sin\theta} + \frac{c-\frac{1}{2}}{c-1+s\cdot\sin\theta}\Big]d\theta$$

which yields after lengthy computations

$$J = \frac{\pi}{12}\Big(\cos^3\varphi_0 + 3\cos\varphi_0 - 4\Big) \qquad 9.$$

This result was checked for a few values of φ_0 by numerical integration. The results are identical.

Substituting back in (5) we obtain

$$I_{13} = \frac{4\pi}{3}\Big(3\cos\varphi_0 + \cos^3\varphi_0\Big) \qquad 10.$$

When $\beta > \pi/4$ the analysis follows the same steps with identical final expression for I_{13}. Substituting eq. 2.4 in 10. yields

$$I_{13} = \frac{4\pi}{3}\Big[3\Big(\frac{E\alpha}{\sigma}\Big)^{1/2} + \Big(\frac{E\alpha}{\sigma}\Big)^{3/2}\Big]$$

APPENDIX III

Elastic wave velocities in rock with a spectrum of
crack shapes

Equation 5.1 relates the integral over a crack distribution to an effective elastic constant

$$Y_{ij} = \frac{1}{C}\left(\frac{E_o}{E_{ij}} - 1\right) \tag{1.}$$

where C is a constant.

The ij's indicate the directions at which this quantity is determined. The second index j relates to the plane of polarization of shear.

Introducing now a spectrum of crack shapes with a density distribution (Fig. 5.5)

$$A(\alpha) = A_o - A_1\alpha \qquad\qquad \alpha \leqslant \beta \tag{2.}$$
$$ = O \qquad\qquad \alpha \geqslant \beta$$

combined with eqs. 4.2 to 4.6 we obtain

$$\frac{E_o}{E_{hyd.}} = 1 + c\left[b_1 - b_2/\beta\right] \tag{3.}$$

$$\frac{E_o}{\bar{E}_{33}} = 1 + c\left[a_1 + b_1 - \frac{1}{\beta}(a_2 + b_2)\right] \tag{4.}$$

$$\frac{E_o}{\bar{E}_{11}} = 1 + c\left[\frac{1}{2}(3a_3 - a_1) + b_1 - \frac{1}{2\beta}(3a_4 - a_2) - b_2/\beta\right] \tag{5.}$$

and $\tag{6.}$

$$\frac{M_o}{\bar{\mu}_{hyd.}} = 1 + c'\left[b_1 - b_2/\beta\right]$$

$$\frac{M_0}{M_{13}} = 1 + c'\left[\frac{1}{4}(3a_3 + a_1) + b_1 - \frac{1}{4\beta}(3a_4 + a_2) - \frac{b_2}{\beta}\right] \qquad \text{7.}$$

$$\frac{M_0}{M_{12}} = 1 + c'\left[\frac{1}{2}(3a_3 - a_1) + b_1 - \frac{1}{2\beta}(3a_4 - a_2) + \frac{b_2}{\beta}\right] \qquad \text{8.}$$

where the expressions for a_i and b_i are

for $\sigma \leq E\beta$

for $\sigma \gg E\beta$

$$a_1 = \int_0^{\alpha_0}\left(\frac{E\alpha}{\sigma}\right)^{3/2} d\alpha = \frac{2}{5}\left(\frac{\sigma}{E}\right) \qquad\qquad a_1' = \frac{2}{5}\beta^{5/2}\left(\frac{E}{\sigma}\right)^{3/2}$$

$$b_1 = \int_{\alpha_0}^{\beta} d\alpha \quad = \beta - \frac{\sigma}{E} \qquad\qquad b_1' = 0$$

$$a_2 = \int_0^{\alpha_0}\left(\frac{E}{\sigma}\right)^{3/2}\alpha^{5/2} d\alpha = \frac{2}{7}\left(\frac{\sigma}{E}\right)^2 \qquad\qquad a_2' = \frac{2}{7}\beta^{7/2}\left(\frac{E}{\sigma}\right)^{3/2}$$

$$b_2 = \int_{\alpha_0}^{\beta}\alpha\, d\alpha \quad = \frac{1}{2}\left(\beta^2 - \left(\frac{\sigma}{E}\right)^2\right) \qquad\qquad b_2' = 0$$

$$a_3 = \int_0^{\alpha_0}\left(\frac{E\alpha}{\sigma}\right)^{1/2} d\alpha = \frac{2}{3}\frac{\sigma}{E} \qquad\qquad a_3' = \frac{2}{3}\beta^{3/2}\left(\frac{E}{\sigma}\right)^{1/2}$$

$$a_4 = \int_0^{\alpha_0}\left(\frac{E\alpha}{\sigma}\right)^{1/2}\alpha\, d\alpha = \frac{2}{5}\left(\frac{\sigma}{E}\right)^2 \qquad\qquad a_4' = \frac{2}{5}\beta^{5/2}\left(\frac{E}{\sigma}\right)^{1/2}$$

Introducing these terms into eqs. 3 to 8 we find the velocities at various states of stress.

For the case of a hydrostatic stress

$$\frac{E_0}{E_{hydros.}} = 1 + c\beta\left[\frac{1}{2} - \frac{\sigma}{E\beta} + \frac{1}{2}\left(\frac{\sigma}{E\beta}\right)^2\right] \qquad \text{for } \sigma \leq E\beta \qquad \text{9.}$$

$$= 1 \qquad\qquad\qquad\qquad \text{for } \sigma \gg E\beta$$

and

$$\frac{\mu_0}{\bar{\mu}\,\text{hydr.}} = 1 + c'\beta\left[\frac{1}{2} - \frac{\sigma}{E\beta} + \frac{1}{2}\left(\frac{\sigma}{E\beta}\right)^2\right] \qquad \text{for} \quad \sigma \leq E\beta \qquad 10$$

$$= 1 \qquad\qquad\qquad \text{for} \quad \sigma \gg E\beta$$

In case of uniaxial stress the elastic parameters in the direction of the applied stress are related to stress as follows

$$\frac{E_0}{E_{33}} = 1 + c\beta\left[\frac{1}{2} - \frac{3}{5}\left(\frac{\sigma}{E\beta}\right) + \frac{3}{14}\left(\frac{\sigma}{E\beta}\right)^2\right] \qquad \text{for} \quad \sigma \leq E\beta$$

$$= 1 + c\beta\left[\frac{4}{35}\left(\frac{E\beta}{\sigma}\right)^{3/2}\right] \qquad\qquad \text{for} \quad \sigma \gg E\beta \qquad 11$$

$$\frac{\mu_0}{\mu_{13}} = 1 + c'\beta\left[\frac{1}{2} - \frac{2}{5}\left(\frac{\sigma}{E\beta}\right) + \frac{9}{70}\left(\frac{\sigma}{E\beta}\right)^2\right] \qquad \text{for} \quad \sigma \leq E\beta \qquad 12$$

$$= 1 + c'\beta\left[\frac{1}{5}\left(\frac{E\beta}{\sigma}\right)^{1/2} + \frac{1}{35}\left(\frac{E\beta}{\sigma}\right)^{3/2}\right] \qquad \text{for} \quad \sigma \gg E\beta$$

and the elastic parameters perpendicular to the uniaxial stress are given by

$$\frac{E_0}{E_{11}} = 1 + c\beta\left[\frac{1}{2} - \frac{1}{5}\left(\frac{\sigma}{E\beta}\right) + \frac{3}{70}\left(\frac{\sigma}{E\beta}\right)^2\right] \qquad \text{for} \quad \sigma \leq E\beta \qquad 13$$

$$= 1 + c\beta\left[\frac{2}{5}\left(\frac{E\beta}{\sigma}\right)^{1/2} - \frac{2}{35}\left(\frac{E\beta}{\sigma}\right)^{3/2}\right] \qquad \text{for} \quad \sigma \geq E\beta$$

and the shear

$$\frac{\mu_0}{\mu_{12}} = 1 + c'\beta\left[\frac{1}{2} - \frac{1}{5}\left(\frac{\sigma}{E\beta}\right) + \frac{3}{70}\left(\frac{\sigma}{E\beta}\right)^2\right] \qquad \text{for} \quad \sigma \leq E\beta \qquad 14.$$

$$= 1 + c'\beta\left[\frac{2}{5}\left(\frac{E\beta}{\sigma}\right)^{1/2} - \frac{2}{35}\left(\frac{E\beta}{\sigma}\right)^{3/2}\right] \qquad \text{for} \quad \sigma \geq E\beta$$

For Barre granite (fig. 5.5) all cracks are closed at 460 bar. If E = 1 Megabar then $\beta \approx .5 \times 10^{-3}$. The shear velocities are related to the shear moduli

$$\frac{(V_s^o)^2}{(V_{s_{ij}})^2} = \frac{\mu_o}{\bar{\mu}_{ij}} \qquad 15.$$

Assuming that Poisson's ratio is independent of stress; thus

$$\frac{(V_p^o)^2}{(V_{\rho_{ii}})^2} \approx \frac{E_o}{E_{ii}} \qquad 16.$$

Knowning the initial and final velocities the two constants C and C' can be obtained from eqs. 9 and 10 combined with 15. At $\sigma = 0$ we have then

$$\frac{(V_p^o)^2}{\bar{V}_p^2} = 1 + \frac{1}{2} C \beta \qquad 17.$$

and

$$\frac{(V_s^o)^2}{(\bar{V}_s)^2} = 1 + \frac{1}{2} C' \beta \qquad 18.$$

For $V_p^o = 5.9$, $V_p = 3.9$, $V_s^o = 3.65$ and $V_s = 2.6$ km/sec we obtain $C\beta = 2.5$ and $C'\beta = 1.92$. These values and eqs. 15 and 16 yield the expressions 6.2 to 6.7 for velocities in Barre granite in various directions relative to the applied stress direction.

At a given uniaxial stress level σ , the elastic constant in the principal direction can be utilized to obtain the velocities in all directions. In an hexagonal system the

three wave velocities are given (Stoneley, 1949)

$$V_P = \left[\frac{A+B}{2\rho} \right]^{1/2}$$

19.a

$$V_{SV} = \left[\frac{A-B}{2\rho} \right]^{1/2}$$

19.b

where $A = C_{1111} \sin^2\theta + C_{1313} + C_{3333} \cos^2\theta$

and $B = \left\{ \left[(C_{1111} - C_{1313}) \sin^2\theta - (C_{3333} - C_{1313}) \cos^2\theta \right]^2 + 4\left[C_{1133} + C_{1313} \right]^2 \sin^2\theta \cos^2\theta \right\}^{1/2}$

and also

$$\rho V_{SH}^2 = C_{1212} \sin^2\theta + C_{1313} \cos^2\theta$$

20.

In chapter 4 it was shown that V_{SV} is almost independent of angle θ while V_p clearly is dependent on direction. Thus all θ dependent terms must cancel in 19(b) which is satisfied by letting

$$(C_{1133} + C_{1313})^2 = (C_{1111} - C_{1313})(C_{3333} - C_{1313})$$

21.

which substituting in eq. 19(b) yields

$$V_{SV} = \left(\frac{C_{1313}}{\rho} \right)^{1/2}$$

22.

and

$$V_p = \left[\frac{C_{1111} \sin^2\theta + C_{3333} \cos^2\theta}{\rho} \right]^{1/2}$$

23.

Denoting $\rho V_{p3}^2 = C_{3333}$ and $\rho V_{p1} = C_{1111}$

eq. 23 becomes

$$V_p^2 = V_{p_1}^2 \sin^2\theta + V_{p_3}^2 \cos^2\theta \qquad \text{24.}$$

and similarly

$$V_{SH}^2 = V_{SH_1}^2 \sin^2\theta + V_{SH3} \cos^2\theta \qquad \text{25.}$$

The V_p^2 and V_{SH}^2 surfaces are therefore spheroids, and the V_{SV}^2 surface is a sphere.

We can test the validity of equation 21. Substituting in 21 from 5.10 yields

$$\left(\mathcal{V}_{13} E_{11} + \mu_{13}\right)^2 = \left(E_1 - \mu_{13}\right)\left(E_{33} - \mu_{13}\right) \qquad \text{26.}$$

expanding and neglecting higher power in $\mathcal{V}_{ij}$

$$2\mu_{13}\,\mathcal{V}_{13}\,E_{11} = E_{11} E_{33} - \mu_{13}\left(E_{11} + E_{33}\right) \qquad \text{27.}$$

and because $\mathcal{V}_{13}$ is small (table 4.2, chap. 4)

$$E_{11} E_{33} \approx \left(1 + \mathcal{V}_{13}\right)\mu_{13}\left(E_{11} + E_{33}\right) \qquad \text{28.}$$

or, letting $\mathcal{V}_{13} = \mathcal{V}_{12} = \mathcal{V}$

$$\frac{1}{\mu_{13}} = (1 + \mathcal{V})\left[\frac{1}{E_{11}} + \frac{1}{E_{33}}\right] \qquad \text{29.}$$

Substituting from eqs. 2.1 and 3.9 yields

$$\frac{2(1+\mathcal{V})}{E_o}\left(1 + \frac{m}{2}(I_1 + I_3)\right) = \frac{1+\mathcal{V}}{E_o}\left(2 + m(I_1 + I_3)\right) \qquad \text{30.}$$

which is an identity. Thus the observation that V_{SV} is almost independent of direction is in good agreement with

129.

the theoretical relationships between the shear and Young's

moduli in rock containing cracks, given small values of

Poisson's ratios.

References:

Aleksandrov, K.S., T.V. Ryzhova, B.P. Belikov, and L.A.
    Sabanova, Anisotropy of the elastic properties of
    rocks, Akad. Nauk. USSR, Izv. Ser. Geol., 6, 17, 1968.

Bisplinghof, R.L., J.W. Mar, and T.H.H. Pian, Statics of
    deformable solids, Addison-Wesley, Reading, Mass.,
    ch. 7, p. 185, 1965.

Brady, B.T., The effects of mechanical anisotropy on the
    transmission of low amplitude stress waves in brittle
    rock, Int. J. Rock Mech. Min. Sci., 6, 1969.

Chinnery, M.A., The stress changes that accompany strike
    slip faulting, Bull. Seism. Soc. Am., 53, 921, 1963.

Eisler, J.D., Investigation of a method for determining
    stress accumulation at depth-II, Bull. Seism. Soc.
    Amer., 59(1), 43, 1969.

Knopoff, L., Energy release in earthquakes, Geoph. J.,
    1, 44, 1958.

Lekhnitsky, S.G., Theory of elasticity of an anisotropic
    elastic body, ch. 1, Holdenday, San Francisco, 1963.

MacKenzie, J.K., The elastic constants of a solid containing
    spherical holes, Proc. Phys. Soc., London, 13, 63,
    2, 1949.

Sato, Y., Velocity of elastic waves propagated in media
    with small obstacles, Bull. Earthq. Res. Inst., 31(1),
    1, 1953.

Stoneley, R., The seismological implications of aelotropy
    in continental structures, Month. Not., Roy. Astron.
    Soc., Geoph. Suppl., 5, 343, 1949.

Walsh, J.B., The effect of cracks on the compressibility of
    rock, J. Geophy. Res., 70(2), 381, 1965.

Walsh, J.B., The effects of cracks on the uniaxial elastic
    compression of rocks, J. Geophy. Res., 70(2), 399, 1965.

Walsh, J.B., The effect of cracks in rocks in Poisson's ratio,
    J. Geophy. Res., 70(2), 5249, 1965.

Zisman, W.A., Comparison of the statically and seismologically
    determined elastic constants of rocks, Proc. Nat.
    Acad. Scien., 19(7), 653, 1933.

Table 5.1

The dependence of the symmetry of the induced velocity anisotropy on initial crack distribution, applied stress and its orientation.

Symmetry of initial crack distribution	applied stress	orientation of applied stress	symmetry of induced velocity anisotropy	number of elastic constants
uniform	hydrostatic	--	isotropic	2
	uniaxial	--	hexagonal	5
	triaxial(*)	--	orthorhombic	9
hexagonal	hydrostatic	--	hexagonal	5
	uniaxial	parallel to axis of symmetry	hexagonal	5
	uniaxial	normal to axis of symmetry	orthorhombic	9
	uniaxial	inclined	monoclinic	13
	triaxial(*)	parallel to axis of symmetry	orthorhombic	9
	triaxial(*)	inclined	monoclinic	13
orthorhombic	hydrostatic	--	orthorhombic	9
	uniaxial	parallel to axis of symmetry	orthorhombic	9
	uniaxial	inclined, in plane of symmetry	monoclinic	13
	uniaxial	inclined	triclinic	21
	triaxial(*)	parallel to axis of symmetry	orthorhombic	9
	triaxial(*)	inclined in plane of symmetry	monoclinic	13
	triaxial(*)	inclined	triclinic	21

(*) Three generally unequal principal stresses.

Figure Captions:

Fig. 5.1   The dependence of crack distribution in an
            aggregate in which all cracks have the same
            aspect ratio on the magnitude and direction of
            the applied stresses. When $\sigma_{33}=P$ and $\sigma_{11}=\sigma_{22}=0$
            then φ_0 is the angle of the cone of normals to
            closed cracks. When $\sigma_{33}=0$ and $\sigma_{22}=\sigma_{11}=p$ then
            $\pi/_2-\varphi_0$ is the angle of the corresponding cone.

Fig. 5.2   The change of various compliance elements with
            uniaxial stress σ_3 in a rock in which all cracks
            have the same aspect ratio. Properties in the
            direction of the applied stress (I_{33}, I_{13}) change
            more with stress than properties perpendicular
            to it (I_{11}, I_{12}). For comparison I_{33}^* is shown
            for biaxial loading normal to direction in
            which property is determined. Under hydro-
            static stress the change is discontinuous be-
            cause the crack shape spectrum is discreet.

Fig. 5.3   Distribution of closed cracks in stressed
            rock. Uniaxial stress is applied along X_1
            while elastic constants are to be determined
            along the X_3 direction. The cone of angle
            φ_0, contains the normals to cracks which were
            closed because of the applied stress.

Fig. 5.4   Distribution of closed cracks in stressed rock.
Uniaxial stress is applied at $45°$ from the
direction of a principal value of the shear
modulus. All normals to cracks which closed
by stress are within the cone φ_o.

Fig. 5.5   Normalized crack shape density function for
Barre and Westerly granites. Data shows a
relative high concentration of very narrow
cracks ($\alpha < 10^{-3}$). The solid line is
the form of $A(\alpha)$ that was used in computa-
tions.

Fig. 5.6   Computed and observed velocities in the
principal directions of the stress induced
anisotropy. (I) hydrostatic stress (II)
uniaxial stress parallel to and (III) per-
pendicular to the direction of wave propagation.
Agreement is particularly good regarding the
differences between I and II for both V_P and
V_{SH}.

Fig. 5.7   Variation of the computed and measured V_P^2
and V_{SH}^2 with direction at a given stress
level. Both V_P^2 and V_{SH}^2 depend on direction
in the same manner.

Fig. 5.8   Change of velocity associated with changes of
stress around faults. Velocity variation
is largest at $\theta = \pi/4$ from fault plane.

No velocity change occurs parallel or normal
to the fault plane ($\theta = 0$, $\pi/2$).
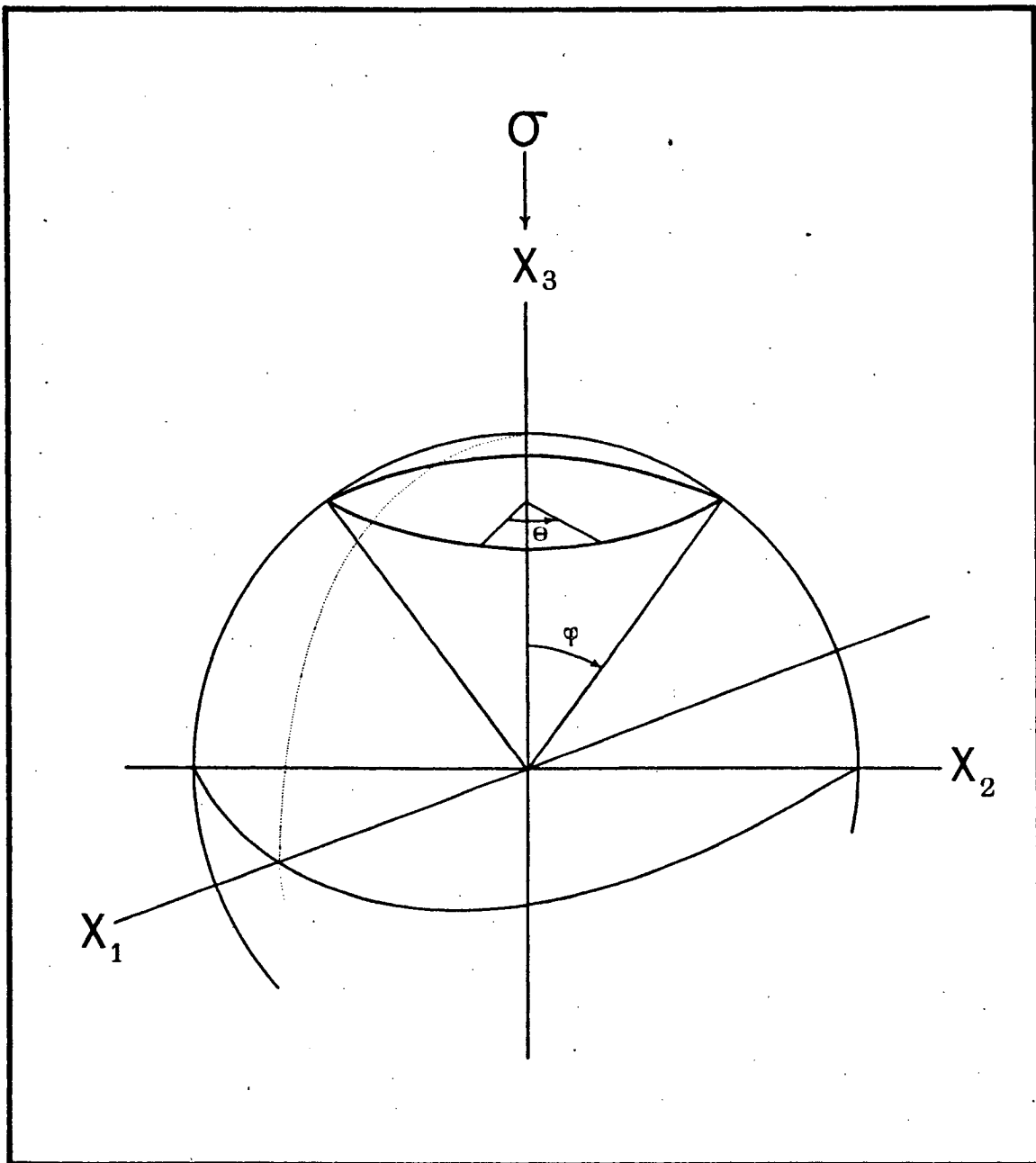
FIG 5.1
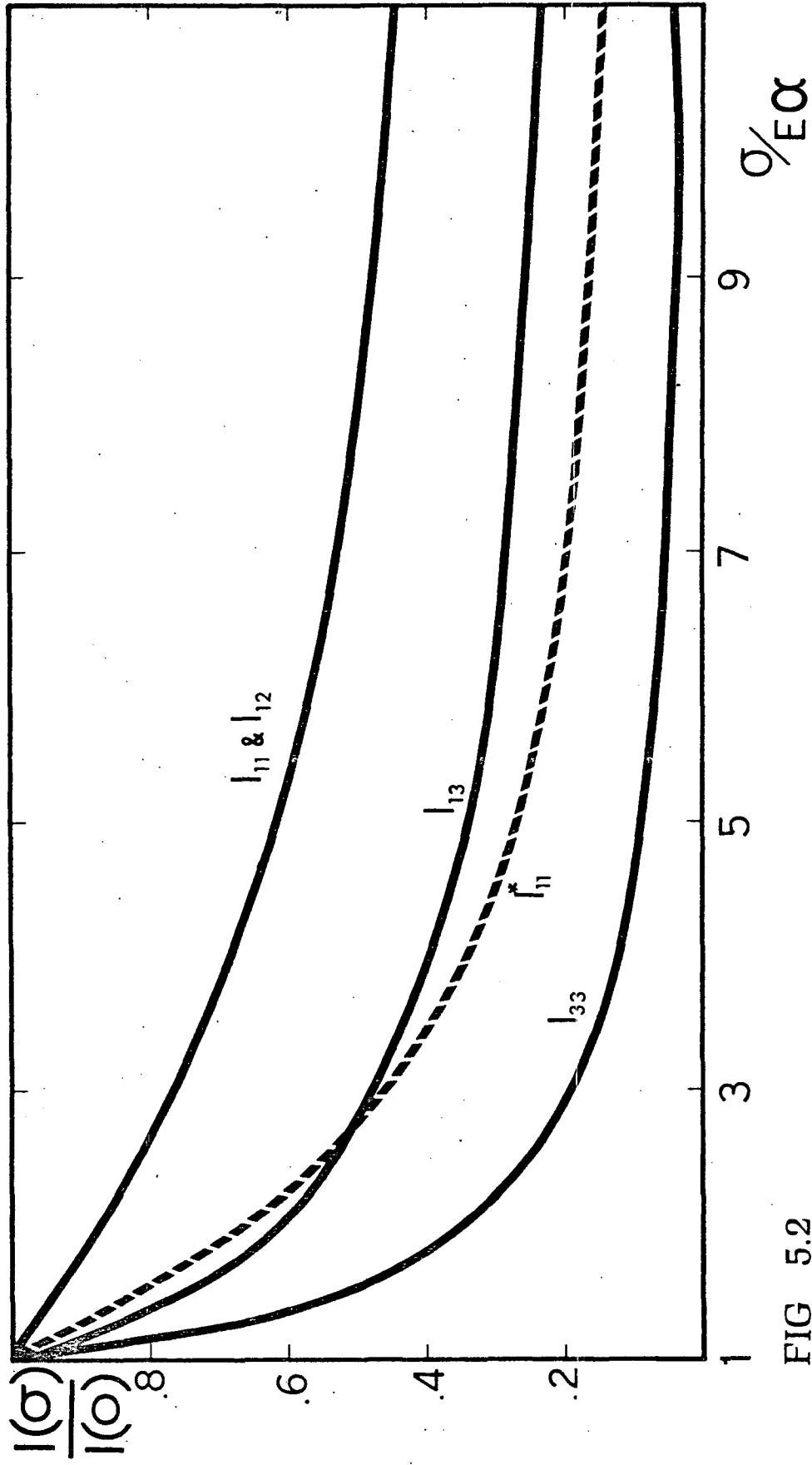
FIG 5.2
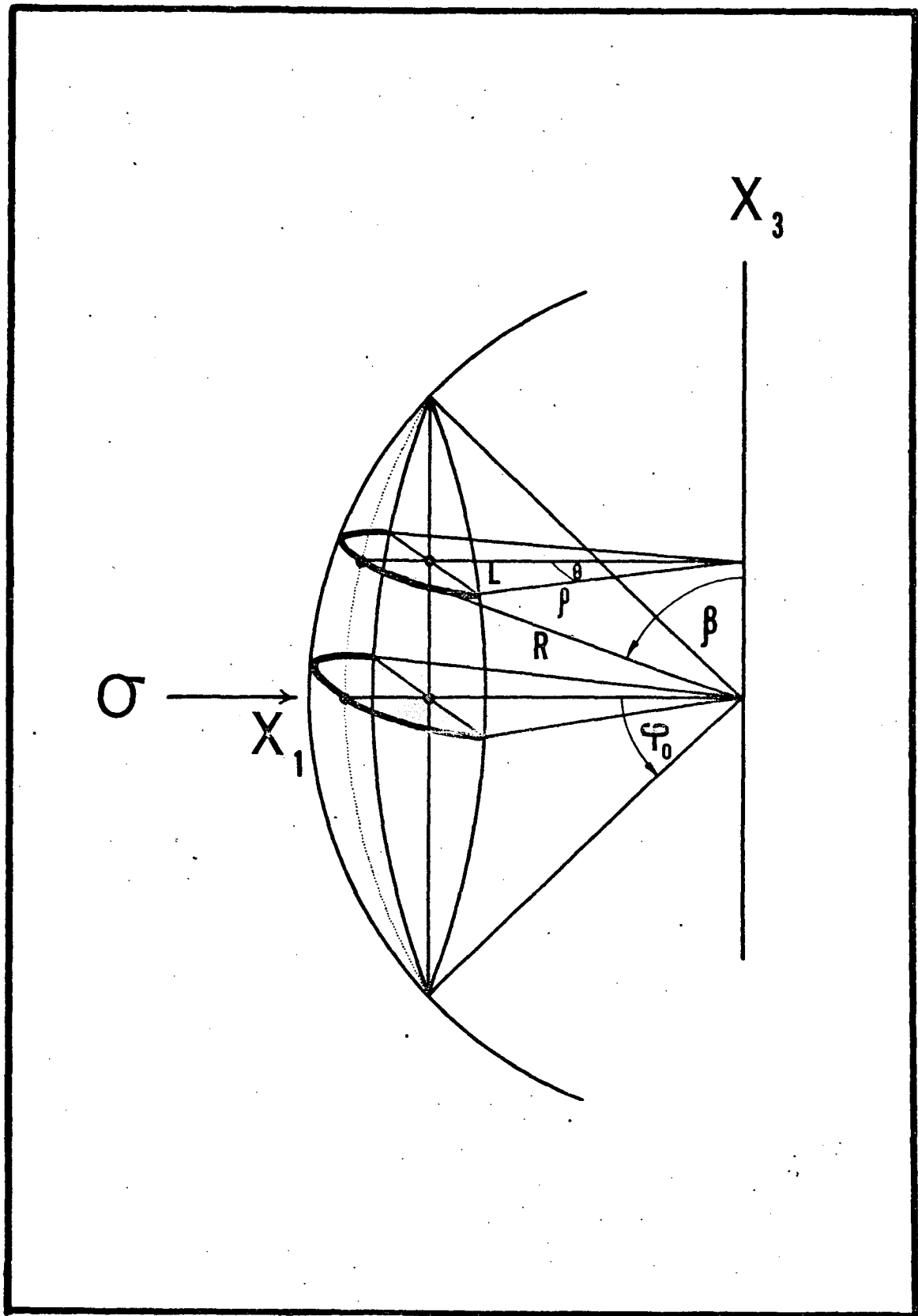
FIG 5.3
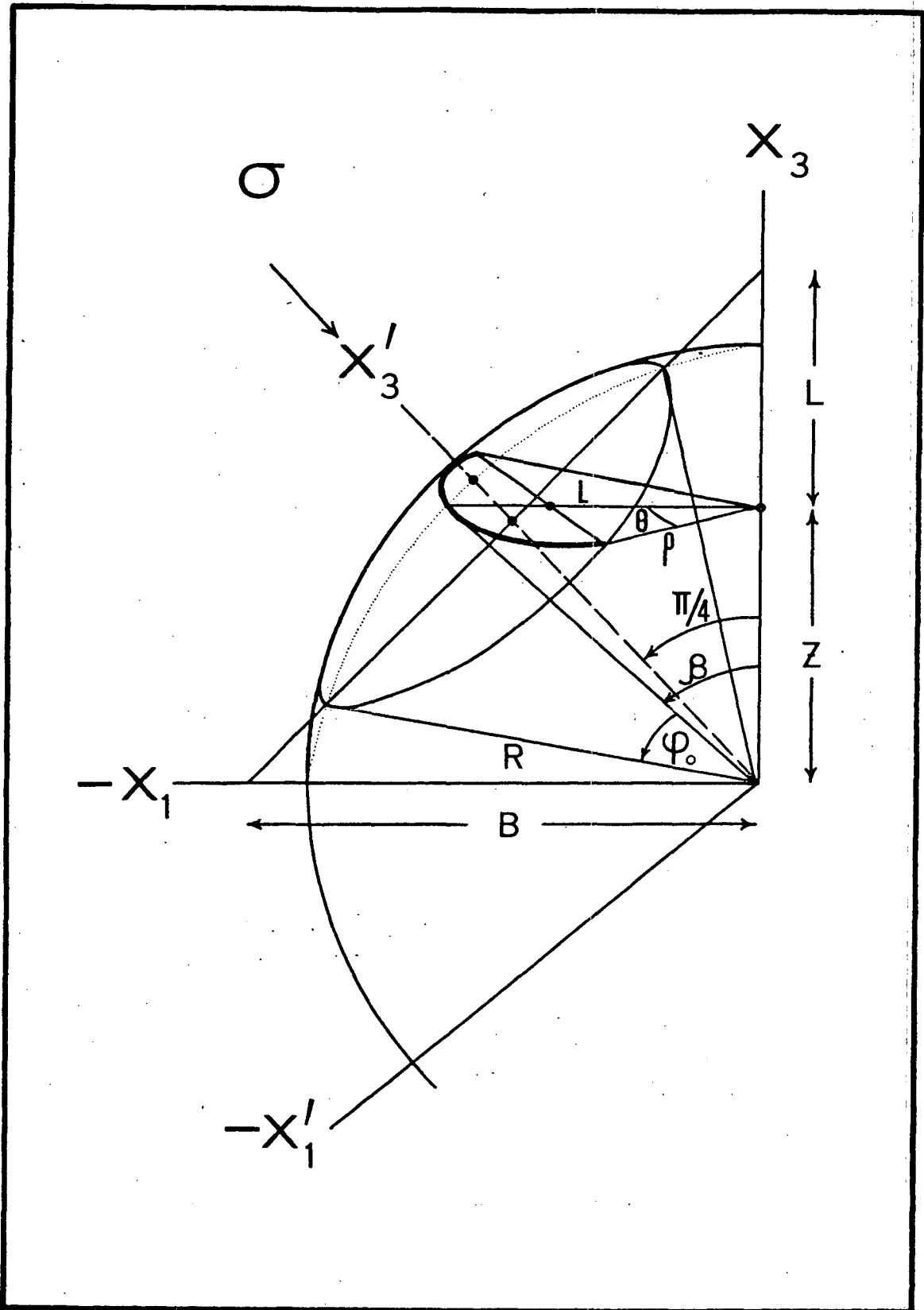
FIG 5.4
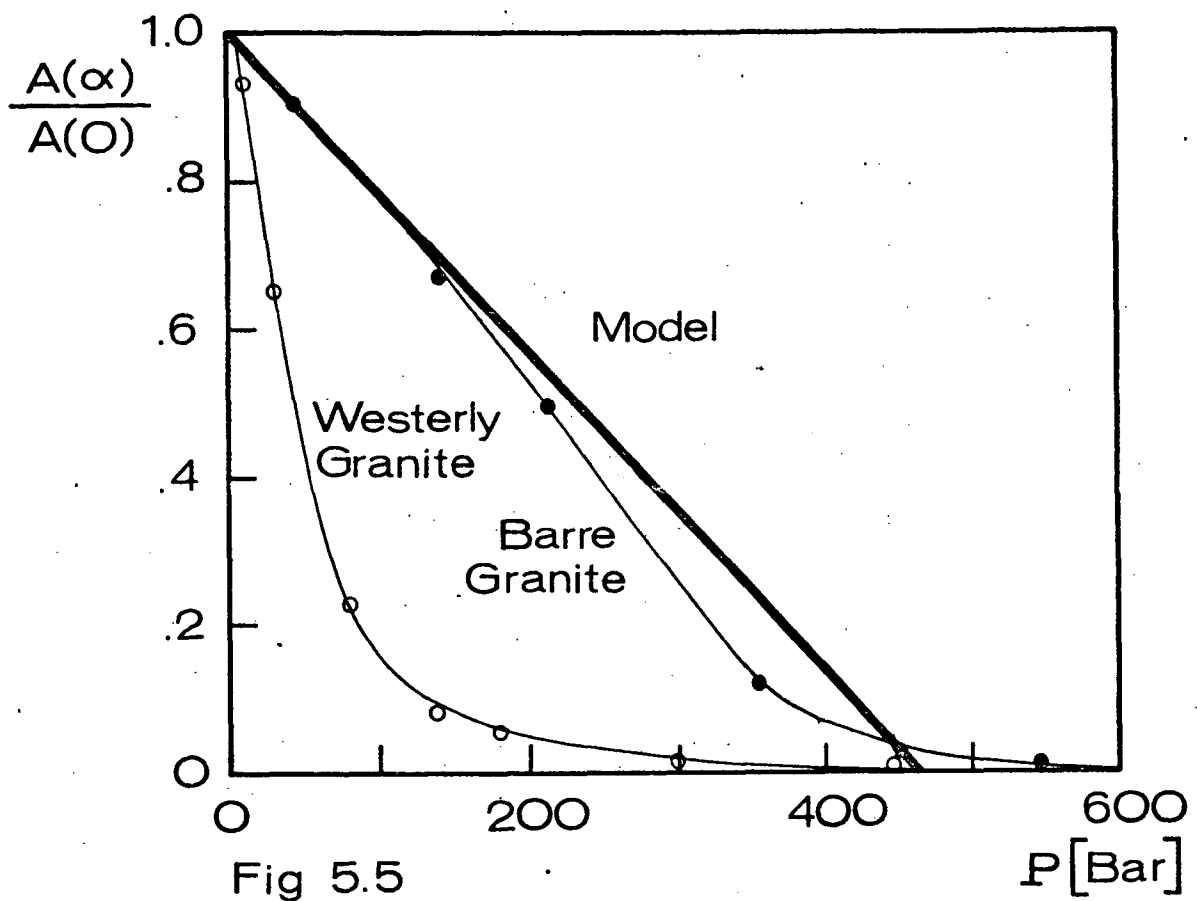
Fig 5.5
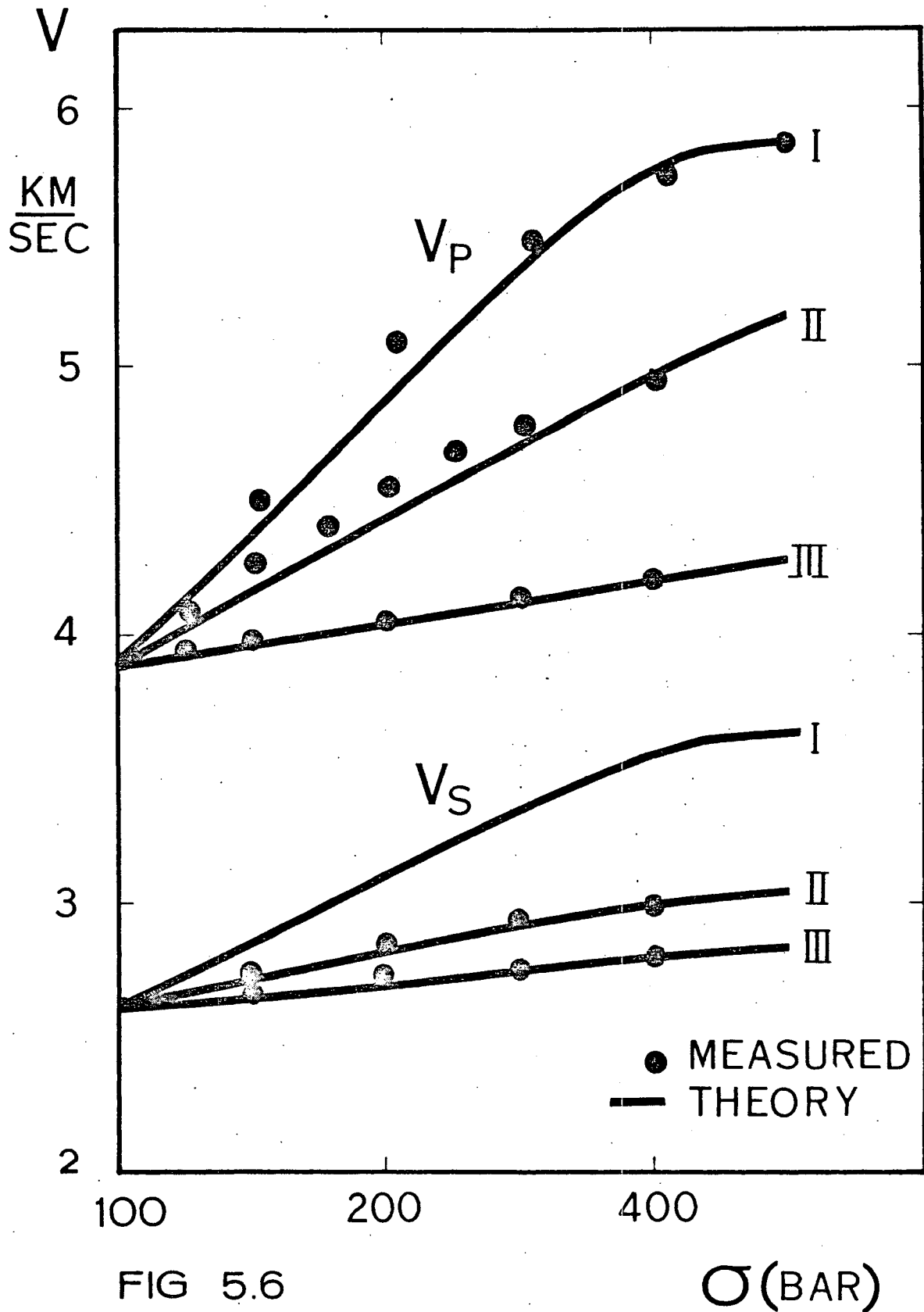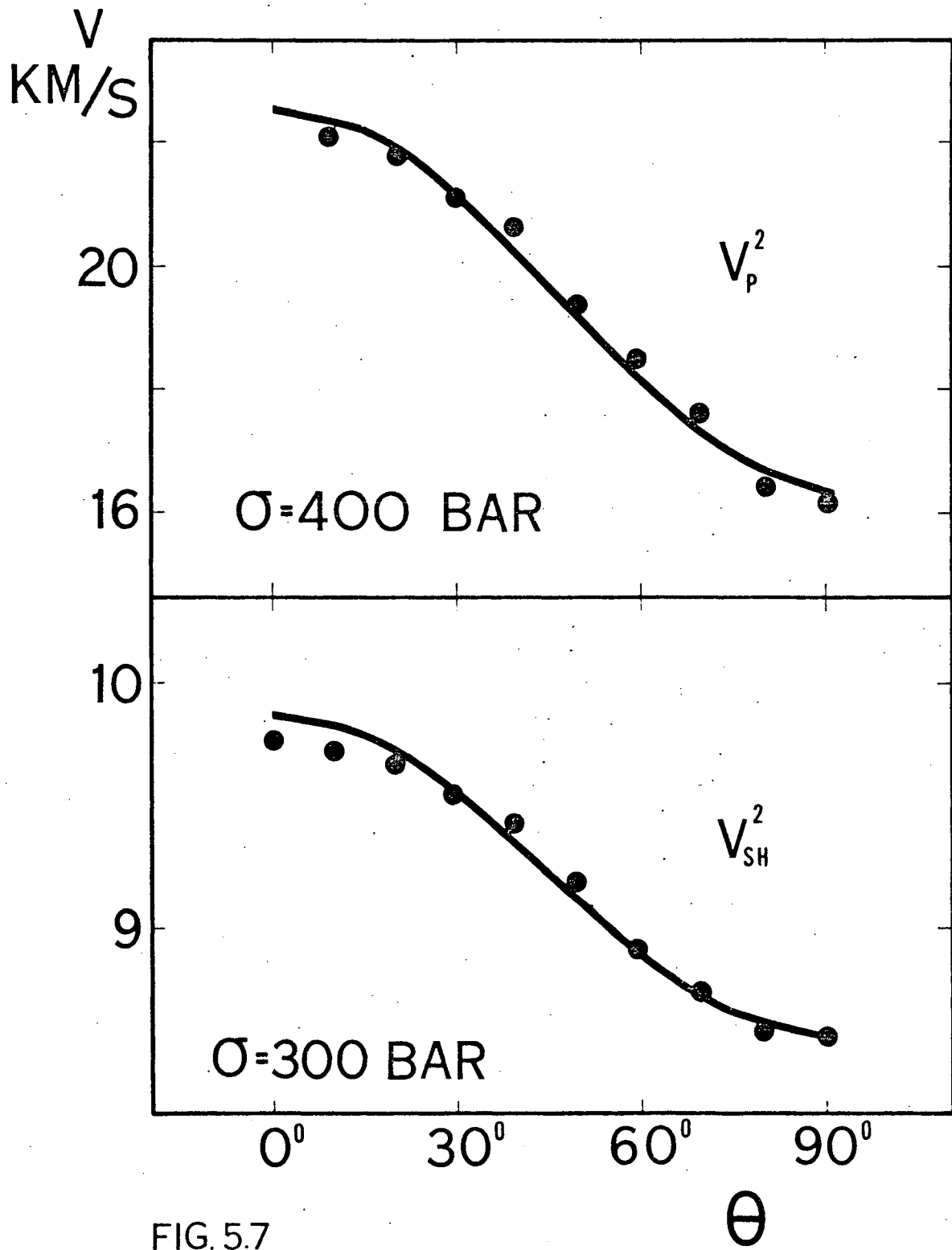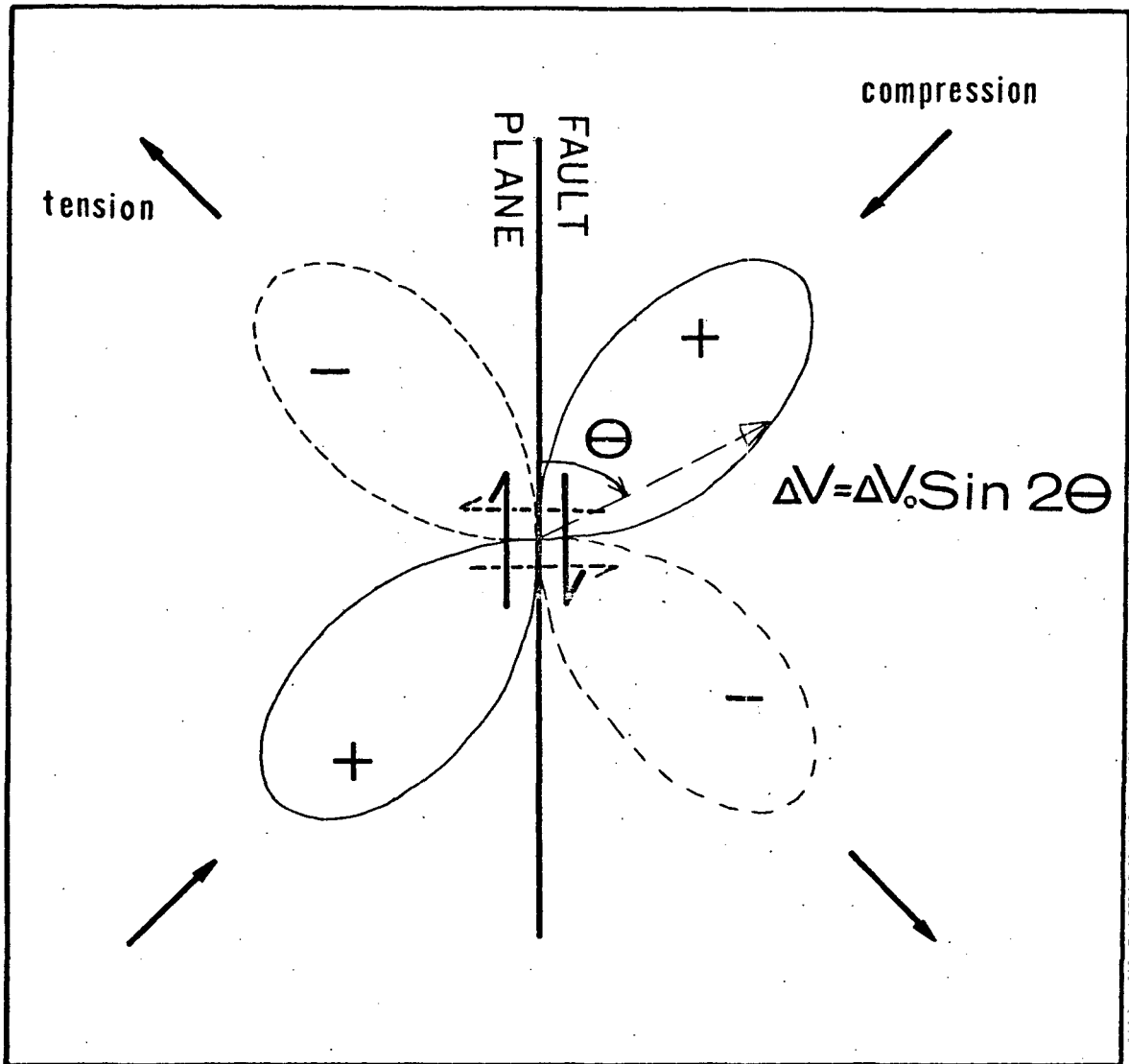
FIG 5.6

FIG. 5.7

FIG 5.8

Chapter 6

The origin of small cracks in igneous rocks

1. Introduction

The properties of many igneous rocks at pressure to
1 or 2 kb, as measured in the laboratory, are dependent on
the behavior of small cracks. If we wish to apply the
laboratory results to the interpretation of rocks in place
then it is necessary to investigate the possible sources of
the cracks. In particular, we wish to determine whether
cracks exist in the rocks--in situ and whether they can be
introduced into a rock sample upon removal from the earth.
The microcracks are probably associated with boundaries
between grains, and as such must be distinguished from
faults and joints, whose length is measured in meters or
kilometers. Microcracks are therefore mostly shorter than
the diameter of the grains in rock.

In this note we look at some available data for brittle
rocks in order to evaluate the relative importance of the
pressure and thermal history and mineralogical composition
on crack density. We also examine the mechanical effects of
drilling cores from rocks under stress.

2. Influence of the thermal and stress history

Igneous rocks are probably in a state of hydrostatic
stress just before solidification from a melt and no
significant non hydrostatic stresses build up as grains grow
from the melt. However, by the time the solid rock is

exposed at the surface of the earth, two major changes have occurred, the temperature is reduced several hundred degrees and the pressure several kilobars. Because rocks consist of mineral phases which have different mechanical properties such changes produce intergranular stresses. Even in rocks made of a single mineral the random orientation of anisotropic grain will also cause intergranular stresses. Cracks will occur when these internal stresses exceed the strength of the material.

A simple model will permit a rough estimation of crack density from the properties of the constitutive minerals. In a solid with a spherical solid inclusion we find (appendix I) that the local stress concentration is approximately proportional to the difference between the bulk moduli of the two solids. If the inclusion is more compressible than the matrix and the initial external stress is sufficiently large, removal of this stress will cause fracture in the matrix. At a grain boundary the maximum shear stress is of the order of

$$\tau_{max.} \approx \frac{1}{2} P \left(1 - k_1/k_0 \right) \qquad 2.1$$

where P is an initial pressure of about 10 kb and k_1 and k_0 are bulk moduli of inclusion and matrix, respectively. The values of k_1/k_0 for common mineral pairs and the associated shear stress for P=10 kb are shown in Table 6.1. The shear stress at grain boundaries, of a few kb, is

comparable to the shear strength of several single crystal silicates and the strength of igneous rocks.

If the inclusion is less compressible than the matrix, a separation of the inclusion boundary from the matrix wall will occur and the volume of the new porosity (for small c) will be

$$V \approx c \cdot \frac{P}{K_0} \left(\frac{K_0}{K_i} - 1 \right)$$

2.2

where c is the concentration of phase 1 and P is the initial pressure. If, for example, c = .1 and $\frac{K_0}{K_i}$ = 2.6 (Quartz-Augite, Table 1), the resulting crack porosity is .0015 which is comparable with the porosity of granites. Removal of the initial pressure can cause significant cracking of grains or induce grains to partially separate from one another along grain boundaries.

Consider now differential thermal contraction. Let denote the difference between the thermal expansions of the matrix and the inclusion. The porosity generated by grain separation when the inclusion contracts more than the matrix is

$$V \approx \Delta T \cdot \Delta \alpha \cdot c$$

2.3

If c = .10, $\Delta \alpha = 2 \cdot 10^{-5}/{}^{\circ}C$ and $\Delta T = 6 \cdot 10^2\ {}^{\circ}C$ we find $V \approx 10^{-3}$, which is also comparable to the porosities of granites. The thermal stress which is set up in an aggregate when the thermal contraction of the inclusion is smaller than that

of the matrix is given by

$$\mathcal{T} \approx \Delta T \cdot \Delta \alpha \cdot E$$

If $E_0 = 10^6$ bar, $T = 6 \cdot 10^2$ °C and $\Delta \alpha = 10^{-5}$ °C (Table 6.2)

then $\mathcal{T} \approx 5$ kb a value comparable to the strength of various

minerals in granites and many other rocks.

Consequently, both the differential thermal expansivity

and the differential compressibility of minerals appear to

be a possible source of cracks in igneous rocks. The

pressure of cracks in igneous rocks is correlated with

the presence of quartz.

The difference between the compressional wave velocities

in dry and saturated samples was shown to be indicative of

the crack porosity of a rock sample (Chapter 2, fig. 2.1).

The difference between V_p at high pressure and at room

pressure is related to crack porosity in a similar fashion

(see fig. 6.1 and Table 6.1). In fig. 6.2 we have plotted

the values of $R = (V_{10} - V_0/V_{10})$ where

$V_{10} = V_p$ at 10 kilobars

$V_0 = V_p$ at 10 bars

for various rocks, as tabulated by Press (1966). It is

quite obvious that the large values of R, and hence the

larger values of crack porosity are found in rocks which

contain quartz. Rocks without quartz, such as dunites and

eclogites, have significantly lower crack porosities.

Compared with other common rock-forming minerals, quartz has

unusual properties. It undergoes a large volume change upon cooling from 600°C, about 4.5%, compared to a value of 1-2% for most other silicate minerals. It is also one of the most compressible silicates. These properties of quartz seem to cause the relatively large crack density observed in quartz bearing rocks.

3. Influence of drilling in stressed rocks

Drilling a hole in a stressed solid is accompanied by transient, high stress concentrations around the bottom of the hole. When the initial stress is large, discing of cores occurs (Pretorius 1958, Hast 1958) and the frequency of discing is proportional to the initial stress (Jaeger and Cook, 1963, Obert and Duvall, 1967).

It is conceivable that small cracks can be produced in the core by drilling at stresses well below that at which discing occurs. In order to test this possibility, compressional wave velocities were measured in eight cubes of Westerly granite after a cycle of vacuum drying and exposure to room conditions. The cubes, 5 cm in size, were stressed uniaxially, each at a different stress level , while a core 2 cm in diameter was drilled. Compressional wave velocity was measured on the cores after vacuum drying and reexposure to room conditions; the results are shown in fig. 6.3. The last core, at a stress of about 800 bars, broke into a number of thick discs and velocity could not be measured. The velocity in all other cores, drilled under

lesser load, is only slightly below the initial velocities in the cubes. A small increase in the difference between the two velocities with increasing stress ($\partial V / \partial \sigma \approx 1\%$ per 100 bars) indicates that a few small cracks are produced before discing occurs but that at stress just below the discing stress, such cracking is not significant. These results are in agreement with other work on microfracturing in rock. Scholz (1968), for example, found that most of the microfracturing in rock subject to increasing non-hydrostatic stress occurs just before the shear strength of the rock is exceeded.

4. Conclusions

Small cracks in igneous rocks appear to be associated with both the history and mechanical behavior of the rocks. Existence of these cracks is due mainly to the differential thermal expansivity and compressibility of minerals and in particular quartz in these rocks.

Unless the stress in situ is very high only a few small cracks will be introduced into the sample while it is being cored. When the in situ stress is high discing occurs.

The mechanical properties of igneous rocks measured in the laboratory on small samples are indeed representative of the in situ properties provided the environmental conditions of pressure, temperature, and saturation are properly modelled.

Appendix

Effects of solid spherical inclusions on the internal
stresses in a composite solid

Suppose a material with bulk modulus K_o and shear modulus μ_o contains a spherical inclusion (fig. 6.4) with bulk modulus K_1. An external hydrostatic pressure $\underline{P}$ is applied at $R = b$. If superscript 0 denotes the material around the inclusion (matrix) and superscript 1 the inclusion itself, the stress and displacement components can be written (Timoshenko and Goodier, p. 358, 1951) as follows

$$\sigma_{RR}^{o} = A - B/R^3 \qquad\qquad \sigma_{RR}^{1} = D \qquad\qquad 1.$$

$$\sigma_{\theta\theta}^{o} = A + B/2R^3 \qquad\qquad \sigma_{\theta\theta}^{1} = D \qquad\qquad 2.$$

$$U_{R}^{o} = \frac{1}{2\mu_o} \cdot \frac{B}{2R^2} + \frac{A}{3K_o} R \qquad\qquad 3.$$

where A, B, & D are constants to be determined.

At $R = a$ the normal stress σ_{RR} and displacement U_R must be continuous, hence

$$A - B/a^3 = D \qquad\qquad 4.$$

$$\frac{A}{3K_o} + \frac{B}{4\mu_o} \cdot \frac{1}{a^3} = \frac{D}{3K_1} \qquad\qquad 5.$$

and at $R = b$, $\sigma_{RR} = P$ or

$$A - B/b^3 = \underline{P} \qquad\qquad 6.$$

solving for A, B & D eqs. 4.5.6 yields

$$A = P \frac{1+n}{1+n-c(1-m)}$$

7.

$$\frac{B}{a^3} = P \frac{1-m}{1+n-c(1-m)}$$

8.

$$D = P \frac{m+n}{1+n-c(1-m)}$$

9.

where $m = K_1/K_0$, $n = 3K_1/4\mu_0$ and $c = (a/b)^3$

which is the concentration of the inclusion material.

The magnitude of the shear stress at the contact between the inclusion and matrix is given by

$$\tau_{max} = \frac{1}{2}\left|\sigma_{RR} - \sigma_{\theta\theta}\right| = \frac{3}{4} P \left(\frac{1-m}{1+n-c(1-m)}\right)$$

10.

or for small c and n $\approx$ 1

$$\tau_{max} \approx \frac{1}{2} P \left(1 - K_1/K_0\right)$$

11.

When $K_1 < K_0$ removing the pressure $\underline{P}$ will cause internal shear stress τ_{max} in the neighborhood of the inclusion. If, however, $K_1 > K_0$ the removal of pressure will simply cause the separation of the inclusion from the matrix. The volume of the porosity can be estimated from the difference in expansion between the inclusion material and an equivalent amount of matrix, or

$$V \approx \Delta V_0 - \Delta V_1$$

12.

and for the whole composite

$$\Delta V_o = C \cdot \frac{P}{K_o} \qquad\qquad \Delta V_1 = C \frac{P}{K_1} \qquad\qquad 13.$$

where C is the concentration of 1 in 0

$$V \approx C \cdot \frac{P}{K_o} \left(1 - \frac{K_o}{K_1} \right) \qquad\qquad 14.$$

Because the matrix now contains primarily holes, there are also stress concentrations induced around these holes. From (10) we find for n = m = 0 and small concentrations

$$\mathcal{T}_{max} \approx \frac{3}{4} P \qquad\qquad 15.$$

Tension could develop around grains for a limited range of elastic constants values. Since the tensile strength of rocks is almost zero, cracks will appear instantaneously.

To evalute the stresses associated with the differential thermal contraction, expressions derived by Uyklestad (1942) for a hot inclusion yield

$$\mathcal{T} = E \alpha T \qquad\qquad 16.$$

where E is Young's modulus, and T is the volumetric strain due to cooling. In the case of uniform cooling α is replaced by $\Delta \alpha$, the difference between the thermal expansion α_o of the matrix and that α_1 of the inclusion, thus

$$\mathcal{T} \approx \Delta \alpha \cdot \Delta T \cdot E \qquad\qquad 17.$$

When $\alpha_i > \alpha_o$, the inclusion will separate from the matrix upon cooling. The volume of the porosity will again be obtained from the difference in volume change between the inclusion and an equal amount of matrix. Thus

$$V \approx c \cdot \Delta\alpha \cdot \Delta T \qquad \text{18.}$$

where ΔT is the temperature difference between melting and room temperature.

References:

Hast, N., The measurement of rock pressure in mines,
    Sveriges Geologiska Undersköning, Ser. C., 52, 3, 1958.

Jaeger, J.C., and N.G.W. Cook, Pinching off and discing of
    rocks, J. Geophy. Res., 68(6), 1759, 1963.

Myklestad, N.O., Two problems of thermal stress in the
    infinite solid, J. Appl. Mech., A-138, 1942.

Obert, L., and W.I. Duvall, Rock mechanics and the design
    of structures in rocks, John Wiley and Sons, N.Y.,
    1967.

Press, Frank, Seismic velocities, p. 197 in Handbook of
    Physical Constants, S.P. Clark, editor, Geol. Soc.
    Amer. Memoir, 1966.

Pretorius, P.G.D., Some observations on rock pressure at
    depth on the ERPM Ltd., Assoc. Mine. Mngres. S. Afr.,
    1958.

Scholz, C.H., Microfracturing and the inelastic deformation
    of rock in compression, J. Geophy. Res., 73(4), 1417,
    1968.

Timoshenko, S., and J.N. Goodier, Theory of elasticity,
    p. 358, McGraw-Hill Book Co., N.Y., 1951.

Table 6.1

Shear stress and porosity due to differential bulk modulus (data from Birch, 1966)

Mineral pair	Ratio of bulk moduli*	Max. shear stress	Estimated total crack porosity at room conditions
Olivine-Augite	.77	1	.0004
Augite-Oligoclase	.75	1	.0003
Oligoclase-Quartz	.38	3	.0012
Augite-Quartz	.54	2	.0015

* K and K are the bulk moduli of inclusion and matrix, respectively.

Table 6.2

Shear stress and porosity due to

differential thermal expansion (data from Skinner, 1966)

Mineral pair	Difference in thermal expansivity	Max. shear stress	Estimated total crack porosity at room condition
Olivine-Augite	1	3	.0003
Augite-Plagioclase	0.7	2	.0002
Plagioclase-Quartz	3	9	.0009
Quartz-Augite	4	12	.0012

Table 6.3

Difference in compressional velocity at 10 kb and room

pressure for air dried samples

Rock	Symbol	($\pm$.0004)	$V/V_o(\pm.03)$	References
Oak hall limestone	OL	0	.045	1
Fredrick diabase	FD	0	.051	1
Troy granite	TG	.001	.148	2
Rutland quartzite	RQ	.001	.132	1
Westerly granite	WG	.002	.333	1
Stone mnt. granite	SG	.0035	.428	1
Casco granite	CG	.0045	.500	2
Webatuck dolomite	WD	.0022	.270	2

1. Velocity data from Simmons and Brace 1965. Crack porosity from Brace 1965.

2. New velocity data from Nur and crack porosity from Brace.

Figure Captions

Figure 6.1   The relative difference of compressional velocity
$(V_{10}-V_o)/V_{10}$ in igneous rocks between 10 kilo-
bars to room pressure. The difference increases
with increasing crack porosity. V_{10} is velocity
at 10 kb and V_o is the velocity at atmospheric
pressure.

Figure 6.2   The relative difference of velocities $R =$
$V_{10}-V_0)/V_{10}$ computed for many igneous rocks
as a function of their density. Large values
of R indicate large crack porosity and small
values correspond to small crack porosity.
Typical values of R for solids without cracks
are .03-.05. Quartz bearing rocks have the
largest crack density. (Data from Press, 1966).

Figure 6.3   Compressional wave velocities in cores drilled
from stressed blocks at various stresses. The
difference of velocity between the core and
the block it came from increases slightly
with increasing stress, indicating the presence
of new cracks. At 800 bars core broke into
thick discs.

Figure 6.4   Geometry of two phase model. A spherical
solid inclusion with bulk modulus K_1 embedded
in a solid with bulk and shear moduli K_0
and μ_0 respectively, subject to a hydrostatic
stress P.

Fig. 6.1   crack porosity
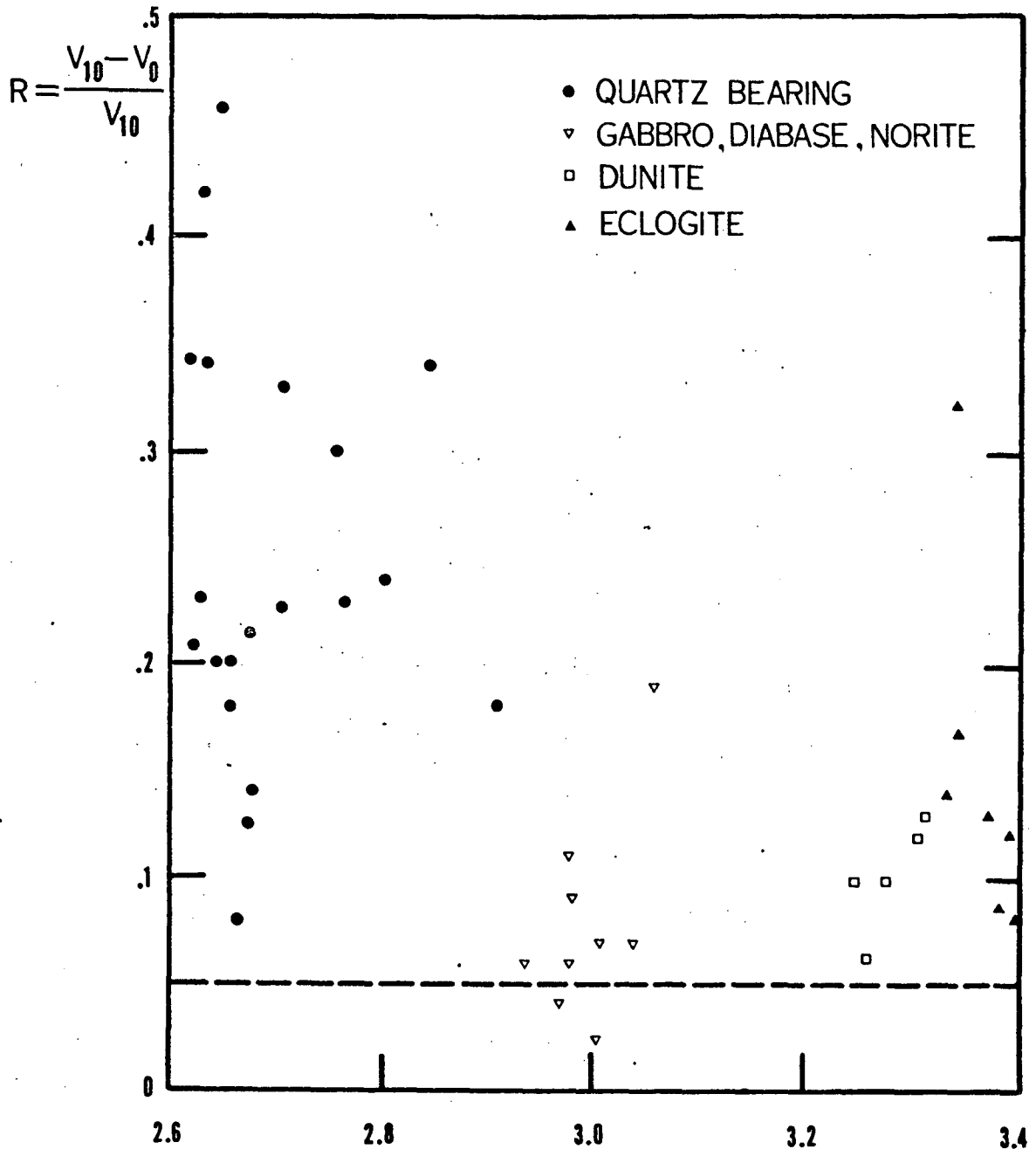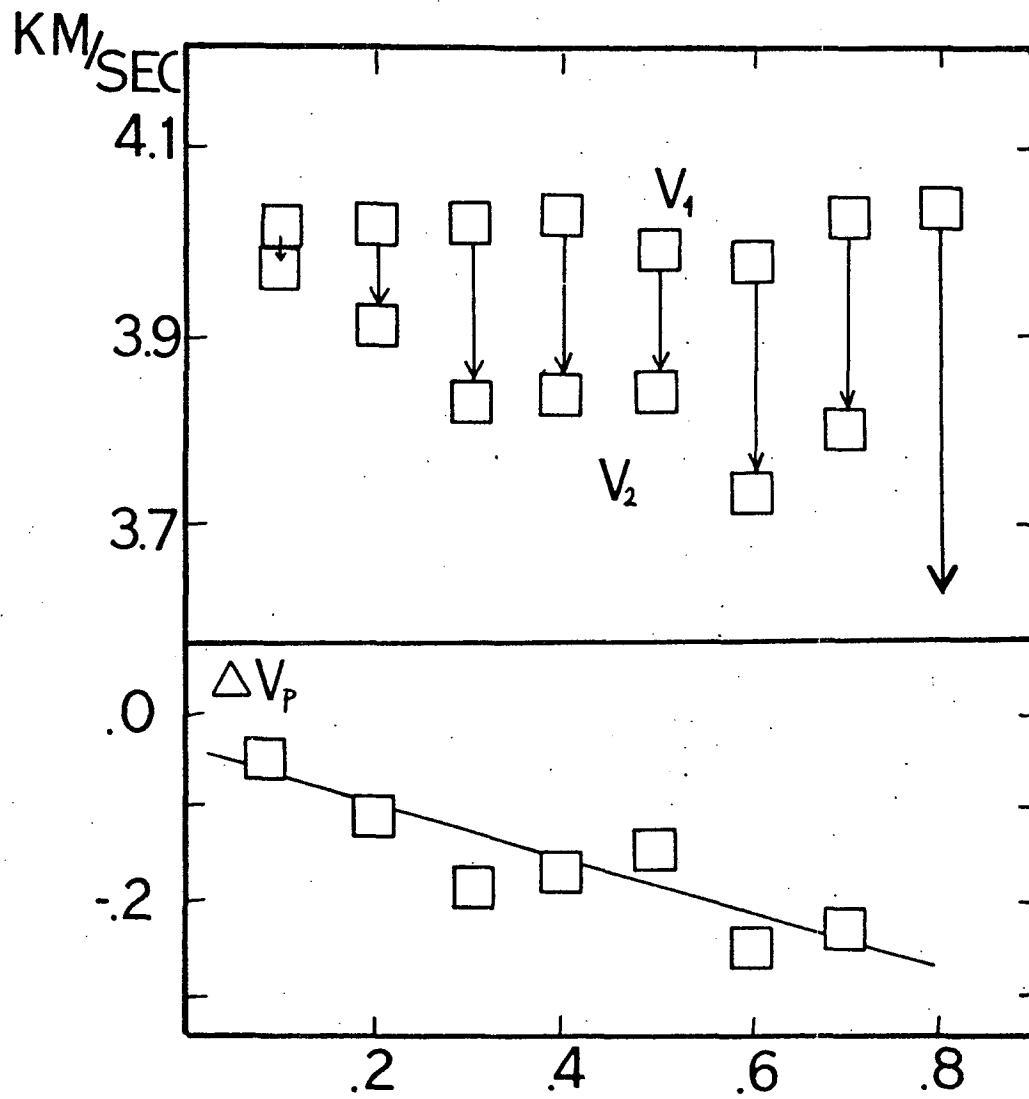
$$R = \frac{V_{10} - V_0}{V_{10}}$$

- • QUARTZ BEARING
- ▽ GABBRO, DIABASE, NORITE
- ▫ DUNITE
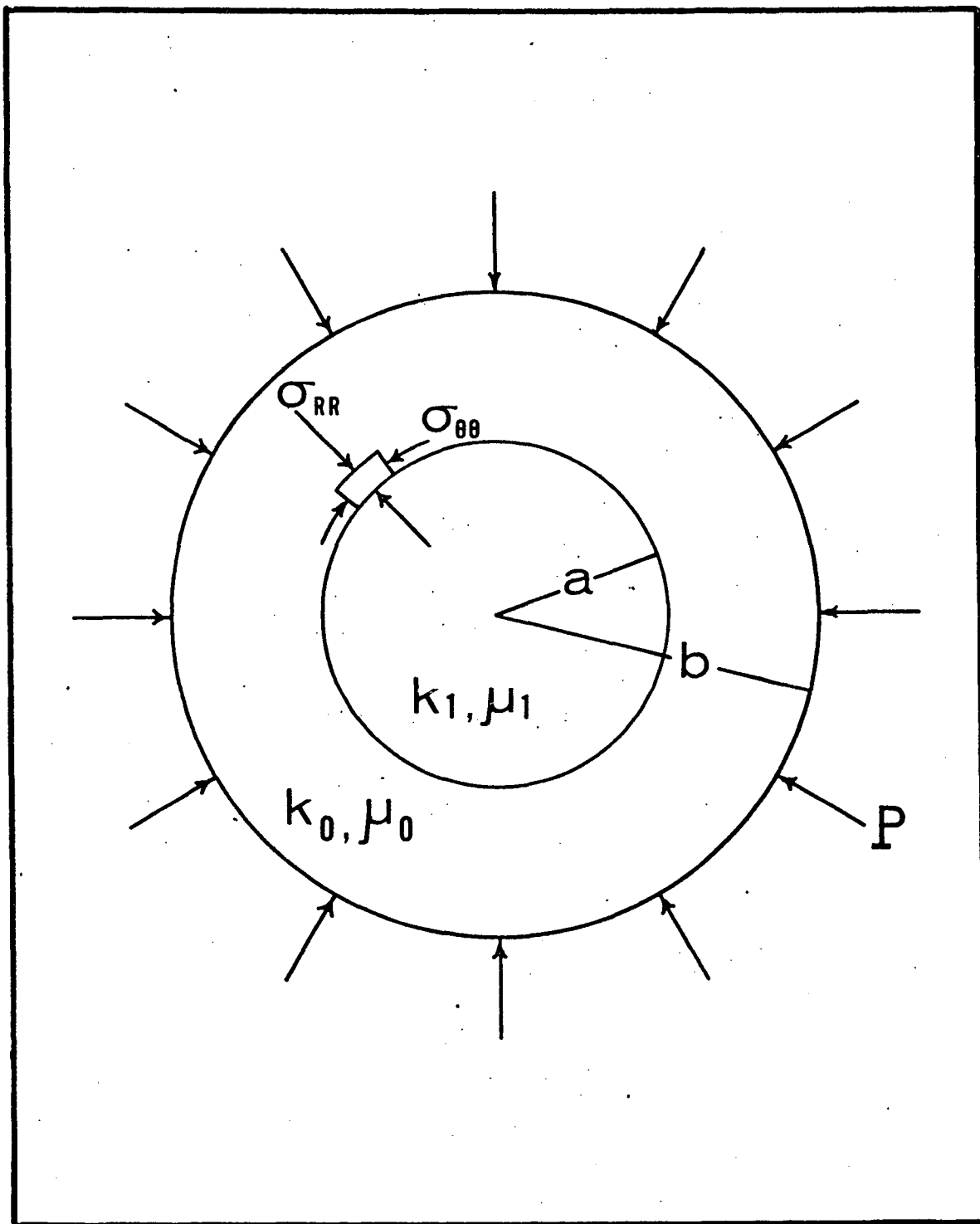- ▲ ECLOGITE
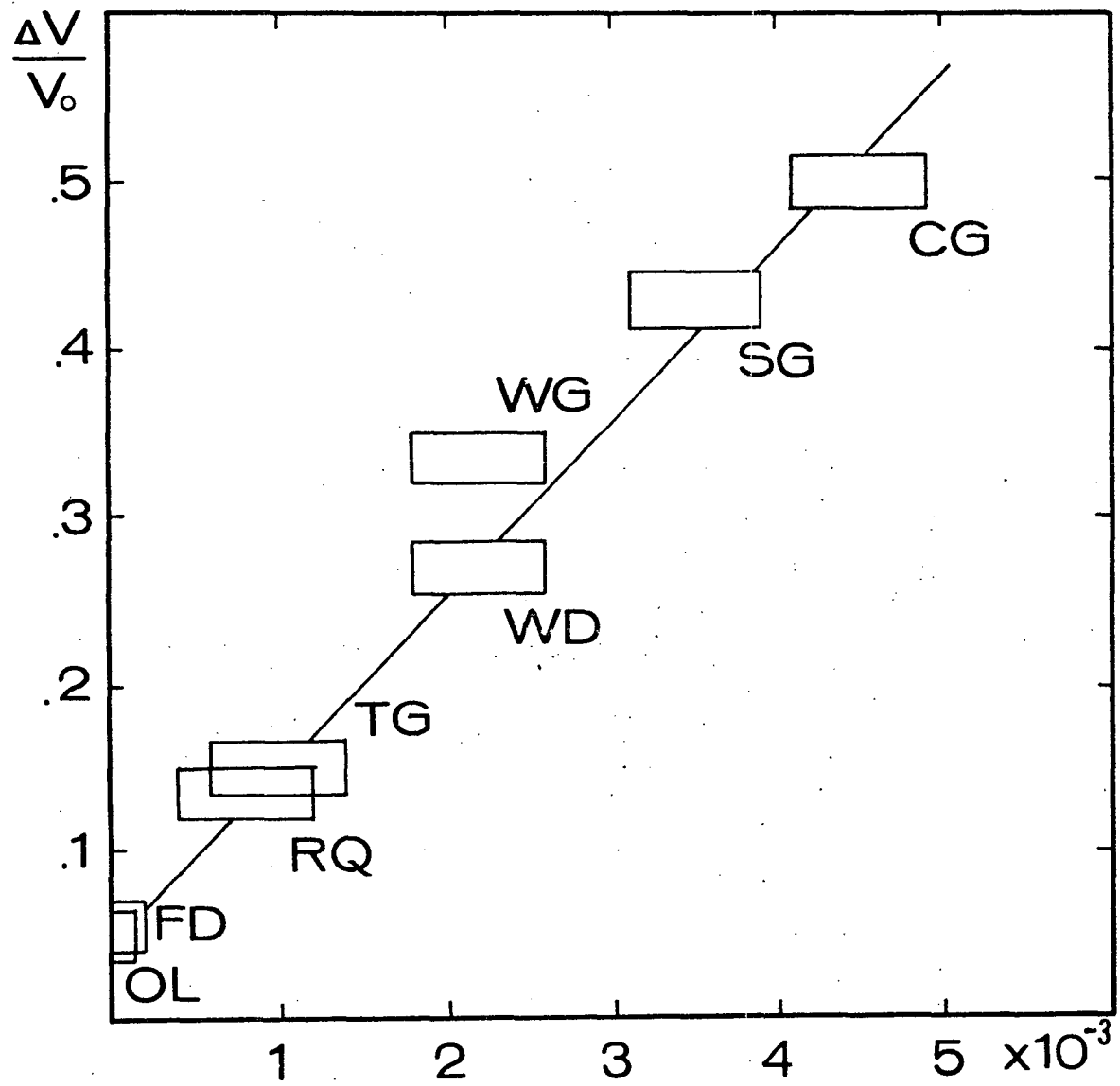
FIG 6.2

FIG 6.3

Fig 6.4

Chapter 7

In situ stress determinations from

velocity measurements

1. Introduction

Many physical properties of rocks are stress dependent.
These include the velocities of elastic waves, electrical
resistivity, magnetic susceptibility, fluid permeability
and thermal conductivity. All of these properties become
dependent on direction in a rock with cracks under non-
hydrostatic stress and may be useful for determination of
stress in situ. Perhaps the most promising approach to in-
direct stress measurements is the simultaneous measurement
in situ of several such properties. In this chapter though we
examine only the use of field measurements of the velocities
of elastic waves to determine in situ stress.

Measurements of velocities under the controlled condi-
tions of the laboratory are the basis for the interpretation
of field data. Perhaps the most important aspect of the
laboratory work is the simulation of environmental condi-
tions of rocks in the earth. Requirements for the simulation
of pressure and temperature have been known at least since
1923 (Adams and Williamson 1923). The need for simulation
of saturation, pore pressure, and viscosity of pore fluids
has been established only recently for such low porosity
rocks as granites.

Such measurements made in the laboratory studies have
been limited to small specimens, high seismic frequencies
and coherent solid rock samples which are possibly unre-
presentative of the average large scale features of rocks
in situ. The influence of a truly triaxial stress (three
distinct principal stresses) on the induced velocity aniso-
tropy or the influence of saturation on shear wave velocity
have not even been investigated yet. Furthermore the pre-
sence of initial elastic anisotropy in most rocks requires a
more extensive analysis than that of Chapter 4.

2. Sources of local stress in the earth

The next step in extending the laboratory results to
field use is the investigation of various aspects of the
velocity-stress relationships in controlled field tests.
There are a number of requirements for meaningful tests. We
need to measure seismic wave velocities in situ, measure
elastic properties of a representative sample and compute
the local stress. It is essential to make these tests
where either stresses or stress changes are already known
from independent estimates. This last requirement is quite
demanding, especially when we consider the scale of an in
situ experiment. Although it is not difficult to stress a
small part of the earth, it is very difficult to obtain high
stress over a large region and we are limited to natural
phenomena.

The difficulty of obtaining stress over a large region

can be seen easily. A 10 ton truck, acting as a stress source, will cause an average compressive stress of only 20 to 30 bars 1 meter away. The use of heavier loads will not improve the situation greatly.

The application of several large flat jacks could produce stress of a few tens of bars over a somewhat larger region. Because flat jacks can tolerate only a limited displacement they can be effectively used over a region of a few meters at most.

Another, somewhat similar, loading method is the use of pressurized boreholes. The main advantages of holes over slots are the relative ease with which the holes can be drilled and the great depth which can be reached. The stresses, induced by pressurizing holes are also quite local. The radial stress decreases as a^2/r^2 from the hole, of radius a, and if a pressure of 200 bars is applied in a 15 cm hole the radial stress reduces to 50 bars 30 cm away from the hole and to 1 bar 2 m away. An increase of the extent of the induced stress perhaps by a factor of two is possible by pressurizing a second borehole, a few feet away from the first hole.

Stresses near the surface of the earth associated with such topographic features as canyons and cliffs may be as large as 200 bars. The vertical stress at a bottom of straight rocky cliff of height h is $\sigma_z \approx \rho gh$ where ρ is the density of the rock. For most rocks $\sigma_z \approx$ 200-300 bar/km

and thus most cliffs are much too small to cause stresses
in excess of 50 or 70 bars (corresponding to 150-250 meters).
Obviously the stresses due to self weight are small in most
natural sites with the exception of a few localities such as
Yosemite Valley with a granite cliff of 1 km and where the
associated stress is roughly 150-200 bars.

There are various known sources which cause <u>changes</u>
of stress over extensive regions. Atmospheric pressure
centers, Earth tides, ocean tides and floods are such long
period natural stress sources. Of these, ocean tides and
periodic floods cause the larger stress changes. Ocean
tide is about 3 meters, which corresponds to a stress change
of approximately .3 bars in regions adjacent to the ocean.
Earth tides and atmospheric pressure centers cause stresses
which do not exceed a hundredth of a bar. None of these
sources appear to be useful for our purposes.

The construction of a new dam could perhaps provide
for a controlled stress test in that the rising water level
causes a slow increase of the stresses around the dam site.
The stress would not exceed 1 or 2 bars but the areal extent
could be several 100 km^2.

3. <u>Stress changes and strain accumulation associated with</u>
   <u>earthquakes</u>

The <u>change</u> of stress with time, possibly easier to measure
than the absolute stress, associated with such phenomena as
earthquakes is of considerable value in the study of the

dynamic phenomena of the earth. We may be able to use the stress change associated with earthquakes to calibrate the velocity-stress relationship in tectonically active areas and then to use the relationship to study stress accumulation prior to other earthquakes. Chinnery (1967) listed several earthquakes and their associated stress drops which were calculated from the known sizes of the faults and the measured dislocations. The largest estimated stress release (Knopoff 1958) is 188 bars and the smallest (Aki 1967) .5 bar. Most values are in the range of 20-100 bars. Measurements of velocity to detect such stress changes appear to be possible. The unpredictability of earthquakes requires however many velocity measurements, repeated several times in a region that is tectonically active. Possibly such measurements should be incorporated eventually in a program of geodetic measurements.

The increase of stress preceding an earthquake is slow. Kasahara et al. (1966) reported a strain increase of 4×10^{-4} per year in the Matsushiro area, a very active region, in 1965-66, with a shear stress increase rate of a few bars per year in this region. Most tectonic regions will exhibit smaller rates. Repeated measurement of velocity by Eisler (1969) near the San Andreas fault indicate a slight decrease of stress over a period of 6 months. On the basis of these rates and the presently available seismic methods velocity tests should be repeated at intervals of two or three years.

The difficulty of using earthquakes for <u>testing</u> our laboratory results, which arises chiefly from their unpredictability, may be circumvented by triggering small or micro earthquakes by explosions as suggested by Aki (personal communication) or by the use of earthquake swarms and aftershocks. The smaller stress changes associated with the smaller events is compensated by the predictability of the occurrence of the event within a shorter time interval. Due to the smallness of aftershocks both in magnitude and aerial extent, the detection of the changes of velocity associated with a single shock may be undetectable. But if the released stress during a long sequence of small shocks has a constant direction a statistical study might reveal a systematic variation with direction of travel time residuals.

4. Velocity measurements in situ

From the values of dV/dp listed for various rocks in Table 7.2, we see that shear velocities are generally less sensitive to stress than compressional velocities in <u>dry</u> rocks but they are almost independent of saturation. Changes in V_p in rocks in situ could always be partly due to changes in saturation and not necessarily indicate a change of stress. Furthermore we believe that in the larger part of the earth's crust, rocks are completely saturated with water and therefore the value of $dV_p/d\rho$ is much less than $dV_s/d\rho$. Shear velocities are therefore more useful as stress indicators provided adequate shear sources are available or can be

built. (Compressional velocities may also indicate stress changes even when the rocks are saturated with fluids. The sensitivity is small but the generation and detection of these waves is easy).

Seismic velocities may be measured on the surface of the earth with seismic profiles, or in vertical profiles in boreholes. In order to measure both magnitudes and direction of the principal stresses many profiles are necessary. Even at very shallow depths, two horizontal principal stress components and one direction are involved and, therefore, at least three profiles are necessary. Several additional profiles may be needed in practice to remove such "noise" as local inhomogeneity of the rock, natural anisotropy of the rock in place, and changes in the degree of saturation along the wave path. The problems of inhomogeneity and anisotropy must be balanced against the need to extend the path length to increase the precision of velocity determination.

An alternative to the use of long paths is the use of high frequency seismic sources either in the form of sharp precisely timed impulses or continuous signals. The impulsive source is well suited for determination of absolute velocities, with limited resolution. It may be a piezo-electric transducer which can be excited at high frequencies and therefore be used only for short wave paths of a few feet. A fast explosive can be used for longer profiles but such

explosives do not generate very high frequencies and the
resolution therefore diminishes. There is no serious
limitation on the length of the spread. Eisler's (1969)
results indicate that the arriving wave forms from similar
explosions are almost identical--perhaps a careful analysis
of a section of the wave form rather than first arrival alone
could improve the resolution. The continuous source is also
applicable to determination of relative velocity or velocity
changes in a given path over a period of time. Repeated
precise measurements of travel times can be achieved easily
and if enough samples are collected a rather detailed pattern
of stress change should be detectable.

Some consideration should be given to the kind of waves
to be used for the determination of stress, or of stress
changes, by seismic profiles. Although in a dry rock the
compressional wave velocity is very sensitive to stress,
saturation decreases the sensitivity greatly. In addition,
because the degree of saturation is commonly unknown, especially
in low porosity rocks, the use of compressional wave velocity
can lead to ambiguous results. On the other hand the genera-
tion and reception of compressional waves is much easier than
shear waves. The velocity of the shear wave which is polarized
in the plane of the applied stress is almost independent of
direction of propagation, while the velocity of the wave
polarized in a perpendicular plane depends significantly
on direction. In the shallow crust then the SV velocity is
dependent on direction. Therefore, for stress determination

from shear velocities we require a source of SV waves.

The second alternative, that of using vertical pro-
files, is best done in boreholes. Such measurements, at
least for compressional waves, have been routine in the oil
industry for a decade or more. Some attempts have been made
to measure both V_p and V_s but the resolution of V_s with pre-
sently used commercial logging tools is not sufficient for
our use. Increased resolution of present instruments is
therefore required.

Waves other than body waves may be used to determine
V_s. Several interface waves have been identified in bore-
holes (White 1965, Chap. 4). Perhaps the most useful one
for us is travels in the fluid column of the borehole with
a velocity

$$V_t = \left[\rho \left(\frac{1}{K_\ell} + \frac{1}{\mu_s} \right) \right]^{-1/2}$$

where ρ is the density of the fluid, K_ℓ is the bulk modulus
of the liquid and μ_s is the shear modulus of the rock.
Because it is easy to determine K_ℓ from compressional wave
velocities in the borehole fluid, μ_s can be obtained. Changes
of μ_s with time can be obtained with even higher accuracy
because changes in K_s are negligible. Since $V_t < V_s < V_p$
the interface wave can travel without excessive loss of
amplitude. Such waves have been observed to travel up and
down boreholes several times (Riggs 1955). Hydrophones,
suspended in the fluid, can be used to determine accurately
phase velocities and core samples from the boreholes can be

References:

Adams, L.H., and E.D. Williamson, The compressibility of minerals and rocks at high pressure, J. Frankl. Inst., 195, 475, 1923.

Aki, K., Scaling law of seismic spectrum, J. Geophy. Res., 72, 1217, 1967.

Chinnery, M.A., Theoretical fault models, delivered at I.U. G.G., Zurich, Switzerland, 1967.

Desai, K.P., Sequential measurements of longitudinal and shear velocities of rock samples under triaxial pressure, Ph.D. Thesis, U. of Tulsa, 1968.

Eisler, J.D., Investigation of a method for determining stress accumulation at depth-II. Bull. Seism. Soc. Amer., 59(1), 43, 1969.

Kasahara, K., A. Okada, M. Shibano, K. Sasaki, and S. Matsumoto, Electro optical measurements of horizontal strains accumulating in the Swarn earthquake area (3), Bull. Earthq. Res. Inst., 45, 225, 1967.

Knopoff, Leon, Energy release in earthquakes, Geophy. J., 1, 44, 1958.

Riggs, E.D., Seismic wave types in a borehole, Geophysics, 20, 53, 1955.

White, J.E., Seismic waves: radiation, transmission and attenuation, ch. 4, McGraw-Hill Co., p. 142, 1965.

Table 7.1

Magnitude and areal extent of various

stress fields

Source or location	Typical areal extent	Stress (bars)
Laboratory	10 cm	10000
Laboratory	1 m	1000
In situ induced stress	5 m	300
Topographic stress	1 km	200
Earthquakes	100 km	100
Ocean tides	500 km	.3

Table 7.2

Observed changes of wave velocities with hydrostatic

pressure in various rocks (in km/s bar)

Rock	(dV_p/dp) satur.	(dV_p/dp) dry	dV_S/dp	Reference
Westerly granite	$1.2 \cdot 10^{-3}$	$4 \cdot 10^{-3}$	$1.2 \cdot 10^{-3}$	Nur(chap.2)
Casco granite	$1.7 \cdot 10^{-3}$	$5 \cdot 10^{-3}$	$3 \cdot 10^{-3}$	"
Webatuck dolomite	$1.0 \cdot 10^{-3}$	$3.5 \cdot 10^{-3}$	$1 \cdot 10^{-3}$	"
Berea sandstone	$1.7 \cdot 10^{-3}$	$13 \cdot 10^{-3}$	$4 \cdot 10^{-3}$	Desai (1968)
Barttesville	$1 \cdot 10^{-3}$	$6 \cdot 10^{-3}$	$3 \cdot 10^{-3}$	"

APPENDIX A

Experimental set-up for travel time measurements

A schematic diagram of the electronic equipment for travel time measurements is shown in fig. A.1. A 404B Fairchild-Dumont pulse generator is used to trigger a 545B Tektronix Oscilloscope with a 1A1 Dual trace plug-in unit. A second, high voltage Velonex model 350 pulse generator is triggered after a constant delay through an Ad-Yu Type 602H2 step variable delay line. A pulse is generated by the Fairchild-Dumont generator, delayed relative to the trigger by the built-in continuously variable delay line. The pulse travels through a continuously variable mercury delay line and is displayed on the oscilloscope's screen. The Velonex generates a strong pulse which travels through the sample and is then also displayed on the screen. The Dumont continuously variable delay is now adjusted to obtain zero reading of the Hg delay line for zero sample length. The early triggering of the scope allows the display of the complete event from pulse triggering to the arriving signal and no calibration is necessary to find the length of mercury which corresponds to zero sample length.

The signals travelling through the sample and the mercury delay line respectively are displayed on the oscilloscope and their first arrivals are made to coincide by adjusting the length of the mercury column. The length of the column, read in mm, together with V_p in mercury

(obtained from calibration with fused silica), 1.46 km/sec, yields the velocity in sample. Accuracy is about 2%, whereas precision is better than .5%.
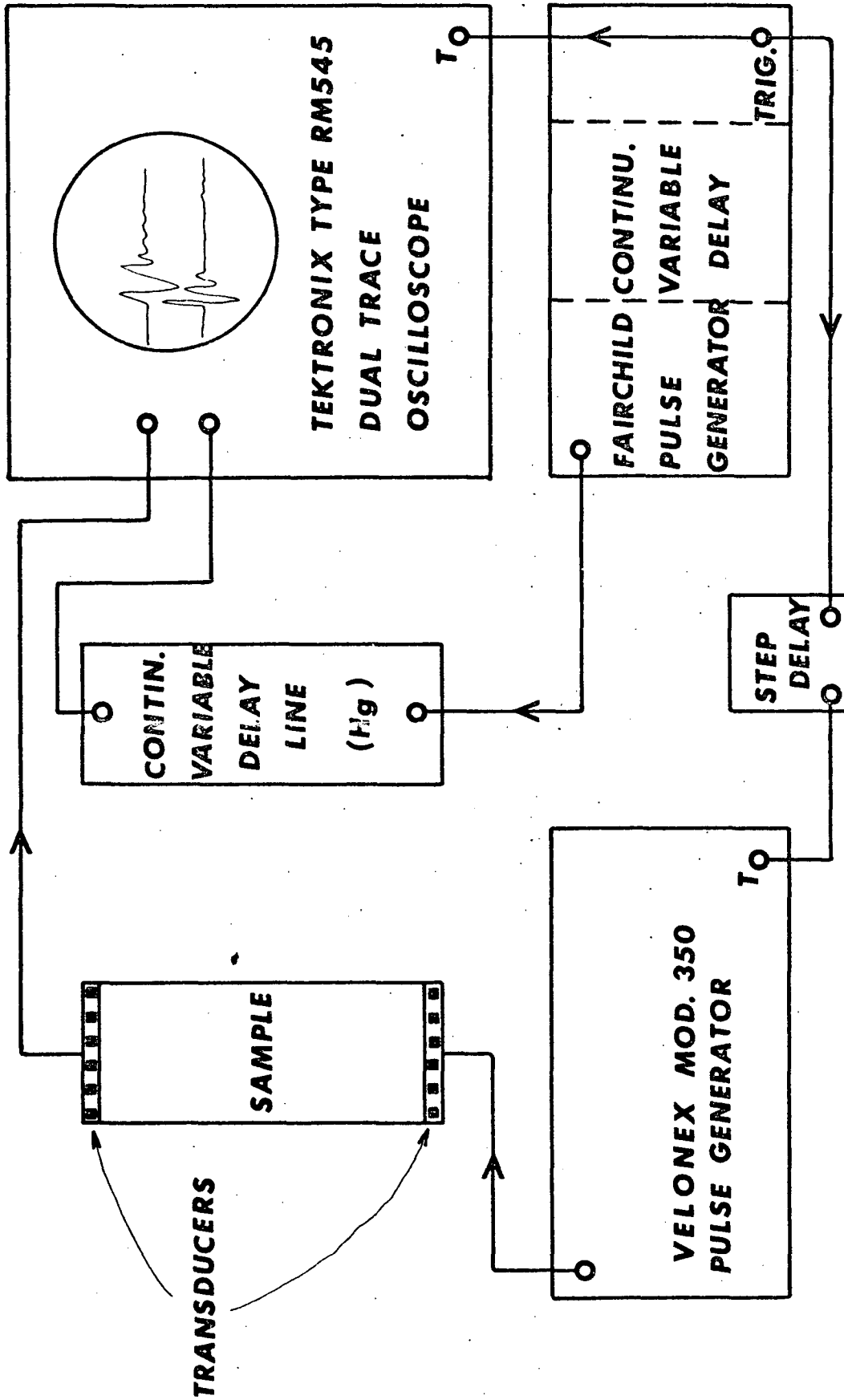
FIG. A1